UNIVERSITY OF OKLAHOMA

GRADUATE COLLEGE

LOCAL FLUID STRESS AND NUTRIENT TRANSPORT EFFECTS VIA SIMULATIONS OF PERFUSION THROUGH BONE TISSUE ENGINEERING SCAFFOLDS

A DISSERTATION

SUBMITTED TO THE GRADUATE FACULTY

in partial fulfillment of the requirements for the

Degree of

DOCTOR OF PHILOSOPHY

By

ROMAN VORONOV
Norman, Oklahoma
2010

LOCAL FLUID STRESS AND NUTRIENT TRANSPORT EFFECTS VIA SIMULATIONS OF PERFUSION THROUGH BONE TISSUE ENGINEERING SCAFFOLDS

A DISSERTATION APPROVED FOR THE
SCHOOL OF CHEMICAL, BIOLOGICAL AND MATERIALS ENGINEERING

BY

_____
Dr. Dimitrios V. Papavassiliou, Chair

_____
Dr. Vassilios I. Sikavitsas, Co-Chair

_____
Dr. Prakash Vedula

_____
Dr. Robert L. Shambaugh

_____
Dr. Matthias U. Nollert

_____
Dr. Henry J. Neeman

DEDICATION

This work is dedicated to my mother. She has supported me throughout my career and I love her very much.

ACKNOWLEDGMENTS

Financial support from NSF is gratefully acknowledged (CBET-070081). Dimitrios Papavassiliou also acknowledges support from the DoE-funded Carbon Nanotubes Technology Center – (Award Register #: ER64239 0012293) and from NSF under CBET–0651180. Computations were carried out at the OU Supercomputing Center for Education & Research (OSCER) utilizing a Dell Pentium4 Xeon E5405 Linux Cluster (sooner.oscer.ou.edu) and at the Texas Advanced Computing Center (TACC) under TeraGrid allocations TG-CTS070037T, TG-CTS-070050, TG-CTS090017, TG-CTS090025 and TG-CTS-090017. TACC utilized a Dell Xeon Intel Duo-Core 64-bit Linux Cluster (lonestar.tacc.utexas.edu). I am thankful to Dr. Henry Neeman and Joshua Alexander, for their lessons and supercomputing support; to Dr. Rheal Towner, Sabrina Doblas, Rebecca Cranford and Joanna DeMoe for their help with MicroCT imaging; to Billy Crook and Advanced Clustering Technologies® for a wonderful computer and tremendous technical support; to Prof. Georgia Kosmopoulou for her input on statistics and to Анна “yami” Назарова for keeping me sane... This work would not have been possible without the help of these people.

TABLE OF CONTENTS

TABLE OF TABLES

TABLE OF FIGURES

ABSTRACT

Lattice Boltzmann Method and Lagrangian Scalar Tracking simulations were performed in order to characterize the mechanical and chemical microenvironments within two different types of bone tissue engineering polymer scaffolds: salt leached foam and non-woven fiber mesh. Surface fluid stresses were calculated for triplicates of foam scaffolds prepared with twelve different combinations of porosities and pore sizes. Equations (31) and (32) were developed based on foam scaffolds simulation results that allow for the estimation of average bulk and surface stresses, but require knowledge of the pressure drop across the scaffold. Alternatively, the Wang-Tarbel Equation [see Equation (40)] does not require a pressure drop measurement, but it requires knowledge of Darcy's permeability (which is presented in Table 6 for foam scaffolds with different porosities and average pore sizes).

Non-dimensionalized fluid stress results from the foam scaffolds were analyzed using statistical fits to 65 different distributions and the generalized three point gamma distribution [see Equation (36)] was found to give the best agreement with the simulation results. Furthermore, it was found that the reduced probability density function for the surface stresses does not depend significantly on the scaffold geometry. Using this finding, a generalized three point gamma distribution was derived that can be used to provide an estimate of dimensional surface fluid stresses for highly porous scaffolds within statistically acceptable limits. The estimation procedure requires knowledge of average surface stress and of fitted parameters given in Equation (44), (a simple procedure for obtaining an estimate of average fluid stress based on well established theory is illustrated as a part of this work). Fluid shear results published by other

laboratories (obtained for different types of scaffolds using experiment or simulation) fit without statistically significant error to the suggested three point gamma distribution. This provides for a quick and rather simple method for obtaining the surface fluid stress distribution for flows through highly porous media, thereby eliminating the need of detailed simulations or experiments. Furthermore, based on properties of the gamma probability density function, the mode value of surface fluid stress (i.e., the most frequent value) is also available from Equation (45).

In order to characterize nutrient transfer within scaffolds, a novel reactive algorithm was developed as a part of this work for modeling solute transport with first order heterogeneous surface reactions using the Lagrangian scalar tracking methodology. Advantages of this approach are that various Schmidt number solutes and different solute release modes can be simulated with a single solvent flow field and a whole spectrum of solute reactivities can be modeled using just a single set of particles. Preliminary results from this method seem to indicate that the nutrients travel longer distances but survive less time at higher flow rates. At high surface area per total volume ratio of the scaffolds the nutrients are more likely to experience a collision with the scaffold wall, and therefore travel shorter distances and survive for less time.

I. INTRODUCTION

In 2004, musculoskeletal disorders cost the US nearly $850 billion – 7.7% of the GDP, with 1 in 4 Americans requiring medical attention.(AAOS, 2008) Current approaches to repair lost or damaged bone include the use of autografts and allografts. However, the lack of autograft availability, donor site morbidity, disease transmission, and limited inductive ability, are major limitations for these approaches.(Laurencin et al., 2006; Toolan, 2006; AAOS, 2008). A very promising alternative approach in regenerating bone is bone tissue engineering (BTE) using biodegradable scaffolds (Caplan and Goldberg, 2004) seeded with bone forming pre-osteoblastic mesenchymal stem cells (MSCs). The MSCs can be obtained from the patient (thereby bypassing any immune rejection problems) and disseminated onto the scaffold, which is then cultured *ex vivo*.(Jaiswal et al., 1997) After the culturing is complete the finished tissue engineering construct is implanted into the patient. The supplement itself does not substitute for the original tissue, but instead induces in-growth from the surrounding bone tissue (osteoinductivity) by providing an attractive environment with appropriate cues. This section provides a brief introduction to bone tissue engineering, the challenges that lay therein and this study's proposed approach at addressing them.

I.1 BONE TISSUE ENGINEERING – AN OVERVIEW

I.1-a 3D Support (Scaffolds)

A scaffold is an artificial structure capable of supporting three-dimensional tissue formation. In the case of engineering bone tissue a three-dimensional support is required for adherent cells to attach, proliferate, maintain their differentiated function, and

eventually form extracellular matrix (ECM) proteins. It also helps to define the shape of the growing tissue. Typically, scaffolds in tissue engineering serve at least one of the following purposes: allow cell attachment and migration, deliver and retain biochemical factors, enable diffusion of vital cell nutrients, and/or exert desired mechanical and/or biological influences on cell behavior.

Preferably, a bone tissue engineering scaffold should be *porous* (with high *interconnectivity* to allow for in-growth of capillaries, perivascular tissues, for mineralization and for efficient mass transport), biocompatible, and bioresorbable. Its surface chemistry should encourage cell attachment, proliferation, and differentiation. Finally, the mechanical properties of the scaffold should be appropriate for the loads it will experience at the bone repair site (without showing symptoms of fatigue or failure, at least until the newly grown tissue takes over).

When implanted, it is desired to have an interlocked transition between natural and artificial tissues so as to prevent any kind of instability along the boundaries between them. In order to achieve osteoinductivity, the cultured scaffold that is implanted into the patient should have an internal environment similar to that of bone: bone's structure and morphology (inorganic hydroxyapatite ($Ca_{10}(PO_4)_6(OH)_2$) and organic matrix made of mostly of collagen type I). The osteoinductive environment is created during the tissue culture process when the cells lay down ECM.

Currently, various scaffold geometries can be manufactured using a multitude of methods from a variety of materials (see Section II.1-c), but no optimal design has been converged upon. Nor is it obvious how exactly the scaffold manufacturing parameters affect the tissue culture process. For a more in-depth discussion of materials, fabrication

methods, and strategies used to enhance bone regeneration in engineered bone tissues see reviews by Stevens et al.(Stevens et al., 2008) and by J.D. Kretlow and A.G. Mikos (Kretlow and Mikos, 2008)

I.1-b Mesenchymal Stem Cells (MSCs)

Progenitor cells used for bone tissue engineering are typically multi-potential mesenchymal stem cells (MSCs), which are derived from adult tissues, such as the bone marrow stroma and a number of connective tissues. Some examples of human MSC lineage differentiation potential are bone, cartilage, adipose tissue, muscle, tendon, and stroma. Differentiation towards a certain lineage can be encouraged via chemical or mechanical stimulation of the cells (see Section I.2). For a more in-depth overview of MSCs, see a review by Tuan et al. (Tuan et al., 2003)

I.1-c Cell Seeding Methods

The process of establishing a 3D cell culture within a scaffold begins either by placing cells on the exterior of the scaffold or by disseminating them throughout the scaffold's interior. This is called cell "seeding" and it may be accomplished in one of the following ways: *statically* (i.e., micropipetting), or *dynamically* (i.e, spinner flask, or perfusion*)*. High density and uniform initial cell distribution on the scaffold's surface have been related to a uniform subsequent tissue distribution, higher matrix production (Vunjak-Novakovic et al., 1998; Moretti et al., 2005) and increased bone mineralization(Holy et al., 2000). Therefore, efficient seeding is desired for enhanced tissue formation. *Static* seeding of cells (i.e., pipetting cell suspensions over the surface of a scaffold), although the most commonly used seeding method on 3D scaffolds, has typically shown to produce poor tissue growth due to low seeding efficiencies and

nonuniform cell distributions within scaffolds (typically high cell densities are achieved only along the periphery at which the cells were deposited). *Dynamic* cell seeding is an alternative that aims to enhance the cell seeding process via flow perfusion. For example, using a *spinner flask* (i.e. a flask with a magnetic stirrer inside it) to seed the cells results in better seeding efficiency. However, it is thought to be appropriate only for high porosity, highly interconnected small samples, because for clinically relevant scaffold sizes, the flow rates achieved using a *spinner flask* are not high enough to perfuse the cells into the inner depths of the scaffold. The most efficient seeding method up to date is *directly perfusing* a cell suspension through a 3D scaffold, because it results in a uniform convection of the cells into the interior region of scaffolds. Perfusion can be done either using an oscillatory flow or unidirectional flow. Oscillatory flow seeding is the most efficient in terms of achieving uniform cell coverage while minimizing the waste of cells since the same cell suspension is oscillated back and forth through the scaffold. (Alvarez-Barreto et al., 2007) For more detail about cell seeding using bioreactors see a review by Wendt et al. (Wendt et al., 2005)

I.1-d Tissue Culturing (Bioreactors)

Culturing methods are similar to seeding methods in that they are also achieved under either *static* or *dynamic* conditions (spinner flask, rotary wall vessel or direct perfusion*)*. Tissue cultured under static conditions is typically inhomogeneous in structure and composition (with tissue-less regions in the center and tissue growth on the outside of the scaffold, if the scaffold is not very thin). This is attributed to the decline of nutrients and accumulation of cellular waste products towards the center of the construct due to poor mass transport properties under static conditions. Therefore, dynamic culture

approaches, such as the *spinner flask*, *rotating wall vessel* (a microgravity environment created by the spin of the outer of two concentric cylinders whose annular space contains the cell culture) and *direct perfusion* bioreactors have emerged as a response to the need of improved mass transport within scaffolds (with the latter demonstrating the most improvement in cell functions and tissue growth).(Alvarez-Barreto and Sikavitsas, 2006)

The four different culturing schemes have been previously compared in their ability to promote growth and osteoblastic function of cells statically seeded on top of porous Poly(DL-lactic-co-glycolic acid) (PLGA) foam discs.(Goldstein et al., 2001) All techniques resulted in similar cell densities, but the rotating wall vessel and flow perfusion system produced the most uniform distribution of cells. While foams cultured in the rotating wall vessel had the lowest levels of alkaline phosphatase activity (a marker of active bone deposition) and those cultured in the perfusion system or in a spinner flask demonstrated enhanced activity with respect to those cultured statically. Therefore, it can be concluded that all of the dynamic culturing schemes outperformed the static controls by any parameters. Also, the flow *perfusion bioreactor* produces uniformly distributed tissue with enhanced activity for bone tissue engineering.

I.2 IMPROVING TISSUE FORMATION VIA STIMULATION

Bone tissue formation within scaffolds can be stimulated in two major ways: *mechanically* and *chemically*. In order to improve the *ex vivo* tissue formation in porous scaffolds, various mechanical signals have been explored that mimic mechanical stresses inside the living bone tissue.(Fritton and Weinbaum, 2009) Among the various *mechanical* stimuli, such as hydrostatic pressure, and substrate deformation (low-

amplitude, high-frequency micro strains, such as muscle contraction during resting state postural activity), shear stress due to fluid flow is thought to be one of the dominant mechanical stimuli for physiological bone cell behavior. *Chemical* stimulation involves the bulk or surface modification of a base scaffold biomaterial with growth and differentiation factors that can improve cell attachment, proliferation, ECM production, and migration. Also, efficient nutrient and waste transport present major challenges in tissue culturing.

Recently, it has been shown that *mechanical* stimulation is able to enhance bone tissue growth irrespective of chemotransport in a study by Sikavitsas et al (Sikavitsas et al., 2003). The effects of mechanical stimulation, in the form of fluid shear stress, were investigated while keeping the chemotransport conditions for nutrient delivery and waste removal constant by perfusing culture media of different viscosities at a constant fluid flow rate. An increase in viscosity, which translates into greater shear forces, was found to enhance the deposition of mineral matrix and the ECM distribution throughout the construct, demonstrating the importance of fluid flow induced shear forces on the creation of bone tissue-engineered grafts. Thus, this study shows that mechanical and chemical stimulations can be treated separately, and this is the strategy that is adopted in this study.

I.2-a Fluid Shear Stress

It has been hypothesized that external forces on bone tissue inside the human body create a pressure gradient that induces fluid flow in the lacuno-canalicular porosity of bone. (Tate et al., 1998; Burger and Klein-Nulend, 1999; Cowin, 1999) The oscillatory fluid flow within the canaliculi (when the force is removed the fluid flows

back as the spongy bone tissue regains its shape) is thought to stimulate a faster and more efficient formation of bone matrix via mechanostimulation of bone cells within the bone's natural physiological environment. For a more in-depth discussion of the current understanding of bone mechanobiology and its implications for clinical medicine and tissue engineering research, see a review by Allori et al.(Allori et al., 2008)

The idea of stimulation via fluid shear has been extended to bone tissue engineering using 3D porous scaffolds.(Sikavitsas et al., 2001; Sikavitsas, Bancroft et al., 2003; Holtorf et al., 2005) The local shear forces have been previously shown to promote osteoblastic differentiation, matrix deposition, and extracellular matrix mineralization. This can be measured by production of alkaline phosphatase, nitric oxide (NO) and prostaglandin PGE_2, expression of genes for osteopontin, cyclooxygenase-2,c-Fos and other intracellular messengers and transcription factors.

Media flow rate through the scaffolds, dynamic viscosity of the fluid, bioreactor configuration, and porous scaffold micro-architecture all play a role in determining the local shear stresses. It has been suggested based on micro finite elements methods calculations that certain regions of scaffolds experience velocities that are up to 1000 times higher than the inlet velocity,(Sandino et al., 2008) thus further supporting the idea that internal morphology of scaffold structures significantly affects interstitial flow (therefore the mechanical loading on cells and the extra-cellular matrix). This suggests that maliciously high shear stress values may be present within the scaffold, which could potentially cause cell lysis and/or detachment. This raises the question of what is the optimal stress that the cells in bone tissue engineering constructs should be exposed to during the culturing process.

The physiologic fluid shear stress through the lacunar-canalicular system has been suggested to be 8-30 dynes/cm^2 (Weinbaum et al., 1994) and *in vitro* studies have confirmed stem cell response to fluid shear forces in the 0.1-25 dynes/cm^2 range.(Maes et al., 2009; Stolberg and McCloskey, 2009) Conversely, an excess of fluid shear ranging from 26-54 dynes/cm^2 can be malicious to the tissue growth via cell death and/or detachment.(Stathopoulos and Hellums, 1985; Cartmell et al., 2003; Alvarez-Barreto, Linehan et al., 2007) The ability to predict shear stress distribution for different scaffold architectures *a priori*, combined with knowledge of how these stresses affect cell growth and/or cell detachment from scaffolds, could lead to scaffold design procedures that would control cell and tissue growth.

I.2-b Cell Signaling, Oxygen/Nutrient & Waste Transport

Since cells consume nutrients and oxygen irreversibly, and produce waste during the culturing process, solute transport in the presence of an irreversible chemical reaction within porous scaffolds typically used in flow perfusion is of interest. The cell culture medium used for culturing is typically Dulbecco's modified Eagle medium (D-MEM, 10% fetal bovine serum), which is a mixture of various proteins, sugars, hormones, growth factors, etc. It also delivers oxygen to the cells. Thus, different components contained in the medium may have a different reaction probability of being consumed upon contact with a cell attached to the wall of a scaffold. Additionally, various biochemical signaling molecules (such as hormones, cytokines, and growth factors) are constantly released by the cells, contained as supplements in the cell culture medium and/or can be incorporated into the scaffold material in order to be released via a timed profile release mechanism.(Allori et al., 2008)

Traditional 2D and thin 3D cell cultures are in constant contact with the cell culture medium and therefore do not suffer from chemo-transportation limitations, whereas scaffolds with a bulk 3D structure of thicknesses relevant to practical applications conditions suffer from poor cellular proliferation, differentiation, and function under static culturing conditions(Alvarez-Barreto and Sikavitsas, 2006) This is attributed to the decline of oxygen/nutrients and accumulation of cellular waste products towards the center of the construct. Several flow perfusion bioreactors have been developed in order to improve the chemo-transportation through 3D porous scaffolds, such as the spinner flask, the rotational bioreactor and the perfusion bioreactor. The constant replenishment of nutrients and removal of waste products via flow perfusion dramatically increase osteoblast differentiation, proliferation, upregulation of osteogenic factors, and mineralized matrix production.(Bancroft et al., 2002; Sikavitsas, Bancroft et al., 2003)

Because transport of cell signals, nutrients, and waste is essential to bone cell culturing, investigation of mass transport within scaffolds is of great interest to bone tissue engineering.

I.3 GOAL OF THIS WORK

The goal of this work is to investigate two dominating controlling factors of bone tissue growth stimulation (fluid shear stress and mass transport) as a function of the scaffold architecture. There are several ways that the effects of fluid shear and mass transport can be controlled in laboratory conditions. For example, for tissue cultured under flow perfusion, the flow rate of the perfused media, its viscosity and composition

all play an important role and have been studied experimentally. However, the internal structure of the scaffold too plays a key part in determining the culturing conditions, as it fixes the flow field of the perfused media and the shape of the growing tissue. Unfortunately, the micro-porous structure of bone tissue engineering scaffolds is too unavailable for experimental observation. Moreover, the degrees of freedom in the manufacturing of scaffolds are vast making it even more challenging to achieve fundamental understanding of how the scaffold architecture affects the tissue culturing process. Therefore, the approach of this study is to use computer simulation in conjunction with non-destructive 3D scanning methods in order to accurately obtain the scaffold architecture and model the localized tissue culturing process conditions that cells would experience if they were seeded onto the scaffold. By parametrically varying the scaffold architecture, the fluid flow rate and the mass transport properties of the fluid, it is desired to obtain insight into how to better design the scaffold architecture for optimal tissue growth (while taking into account the non-idealities of realistic geometries of the scaffolds).

The tissue growth process is dynamic: adhesion strengths change with time as cell coverage grows from an initial monolayer coverage of cells and ECM on the scaffold to multiple layers of cell and tissue growth. Also, the number of cells within the pores of the scaffold changes so therefore does the internal geometrical characteristics of the scaffold. Bancroft et al. investigated long term effects of fluid flow under perfusion on primary differentiating osteoblasts. Initial shear forces experienced by the cells did not exceed 1 dyne/cm^2, whereas long term shear forces escalated to >2 dynes/cm^2 due to tissue growth resulting in tighter pore constrictions.(Bancroft, Sikavitsas et al., 2002)

Furthermore, once the tissue has grown in vivo, the bone remains at a constant state of remodeling: osteoblasts produce and mineralize new matrix, while osteocytes maintain the matrix and the ostoclasts resorb it. Thus the biological environment inside the scaffold can be visualized as a continuously changing 3D matrix of tissue that dynamically responds to mechanical and chemical stimuli. Therefore, it is important to gain understanding into how the presence of newly formed tissue affects the culturing conditions within the scaffolds. Ultimately, the acquired knowledge could be used in order to predict the location and degree of tissue growth based simply the scaffold architecture and the laboratory settings of the culturing process.

I.4 WORK PREVIOUSLY DONE BY OTHERS

I.4-a Fluid Shear Stress

Until recently estimates of fluid shear stress were made using simplifying assumptions about the pore structure and the velocity profile of the fluid within the pores.(Goldstein, Juarez et al., 2001) However, such analytical methods are not based on the actual complex, non-ideal scaffold micro-structure and are, therefore, inherently inaccurate - they offer only an estimation of flow conditions without providing a shear stress distribution. Since, scaffolds with different architectures experience different amounts of internal shear stresses even if the flow rate is the same, the effect of porosity and pore size on the internal shear stress has been previously explored using idealized geometries via computational fluid dynamics.(Boschetti et al., 2006) However, in order to overcome drawbacks of oversimplifications and idealizations, (Porter et al., 2005) calculated local shear stresses inside 3D natural scaffolds using Lattice Boltzmann Method (LBM) simulations for cell culture media flow through trabecular bone, which

was reconstructed using micro-computed tomography (μCT). Since then, μCT has been used in conjunction with fluid dynamics simulations to characterize shear stress distributions within different types of scaffolds (see Table 1).

Table 1 Literature overview of micro-computed tomography based computational fluid dynamics studies of the microfluidics environment within bone tissue engineering scaffolds.

Reference	Scaffold Type	Manufact. Method	Comp. Fluid Dynamics Methodology	Flow Rates Modeled (mL/min)	Number of Samples Modeled	Simulation Domain Size	Shear Surface Stress Values [dyne/cm^2] Average (Maximum)
(Cioffi et al., 2006; Raimondi et al., 2006)	Polyurethane foam: Degrapol®, Swiss Federal Institute of Technology (100 μm average pore size, 71% porosity)	Freeze-Immersion-Precipitation	Fluent	0.5, 3, 6, 9	1 (3 sub-volumes)	0.064 mm^3 cubes (of which only 0.001mm^3 are relevant)	0.0394 (0.27), 0.241, 0.4748 (3.24), 0.7135
(Sandino, Planell et al., 2008)	Calcium Phosphate - based bone cement (300-400 μm average pore size, 71% porosity)	Foaming Albumen	Finite Element (Marc-Mentat, MSC, Software)	1.7x10^{-5} to 1.7x10^{-3}	1	1 mm diameter x 2 mm height cylinders	0 to 0.4
	Glass Ceramic	Foaming Egg White			1		
(Cioffi et al., 2008)	Poly(ethylene Glycol Terephthalate)/ Poly(butylene Terephthalate)	Comp. Molding	Fluent	0.03 and 0.3	1	1.95 mm^3 cube	0.00256 (0.013) and 0.0256 (0.13)

	300/55/45 composition (180 μm average pore size, 80% porosity)						
(Maes, Ransbeeck et al., 2009)	Titanium (280 μm average pore size, 77% porosity)	Gelcasting	Fluent 6.3 (ANSYS, Inc.)	0.04	1 (5 Regions of Interest)	1 to 3.375 mm^3 cubes	0.014 to 0.0195
	Hydroxyapatite (270 μm average pore size, 73% porosity)				1 (5 Regions of Interest)		0.011 to 0.0146 (average)
(Jungreuthmayer et al., 2009)	Collagen-Glycosamino-glycan (96 μm average pore size, 90.5-99% porosity)	Lyophilization	Finite Volume (OpenFOAM icoFoam)	1	1 (3 sub-volumes)	0.64 mm x 0.64 mm x 0.48 mm (of which only 0.32 mm^3 are relevant)	0.2 (0.9)
	Skelite™: 67% silicon stabilized tricalcium phosphate + 33% hydroxyapatite (350 μm average pore size, 58.5-60% porosity)	-		40	3	5 mm diameter x 3.9 mm height cylinders	7.5(31)

Most recently, the first success at a direct experimental measurement of the fluid shear stress within porous chitosan scaffolds using Doppler optical coherence tomography (DOCT) has been reported by Jia et al.(Jia et al., 2009; Jia et al., 2009) At a constant input flow rate of 0.5 mL/min, the measured local fluid flow and shear stress varied from 30 - 100 μm to 100 - 200 μm chitosan scaffolds examined, with a mean shear stress of 0.49 ± 0.3 dyn/cm^2 and 0.38 ± 0.2 dyn/cm^2, respectively. Furthermore, the authors were able to present experimentally measured WSS distributions in representative two dimensional slices of the scaffolds.

I.4-b Oxygen, Nutrient and Waste Transport

Uniform tissue development requires satisfactory delivery of oxygen and nutrients, as well as removal of metabolic waste. Molecular oxygen is essential to cell survival, but can be readily depleted in high-density tissue cultures. Moreover, cell differentiation can be influenced by applying different ranges of oxygen concentration during culture.(Malda et al., 2004; Krinner et al., 2009) Therefore, a thorough understanding of oxygen transport within bone tissue engineering scaffolds can be used in order to increase the quality of cultured tissue and possibly to direct the fate of cell differentiation. Among nutrients, glucose is the most important one since it serves as a source of energy for the cells. Lactate (an ionic form of lactic acid) is an acidic product of cell metabolism that could be harmful if not removed properly from the tissue culture. Most recently it has been shown that both culture conditions (static or dynamic) and cell density (high or low) affect the cell metabolic rates.(Zhao et al., 2005) Moreover, for biodegradable scaffolds, such as PLLA, the material of the scaffold will degrade into acidic byproducts as time

goes on. Although flow perfusion has been shown to decrease the degradation rate (by hindering autocatalysis of the degradable polymer), after two weeks of culture even at these conditions the degradation of the scaffold material will become significant and after 6 weeks the scaffold's mass can decrease by as much as 50%.(Agrawal et al., 2000) Table 2 is a summary of kinetic rates for the major cell metabolic processes that are available in literature.

Table 2 Literature overview of published MSC and bone cell metabolic rates.

Source	Process	Rate [g / (cell sec)]	Cell Type	Culturing Conditions
(Komarova et al., 2000)	O_2 Consumption	1.92×10^{-15}	Mature / Differentiating Rat Calvarial Osteoblasts	Static
(Guarino et al., 2004)	O_2 Consumption	4.8×10^{-15}	Immortalized Rat Calvarial Osteoblasts	Static
(Zhao, Pathi et al., 2005)	O_2 Consumption	0.15 to 1.07×10^{-16}	Human MSC	Perfusion for 4 weeks
(Zhao, Pathi et al., 2005)	Glucose Consumption	0.2 to 1.39×10^{-16}	Human MSC	Perfusion for 4 weeks
	Lactate Production	2.39×10^{-12}		
	Lactate Production	3.35×10^{-14}		

Previously, the impact of oxygen environment on MSC expansion and chondrogenic differentiation was modeled by simulating a stationary pellet culture.(Krinner, Zscharnack et al., 2009) That model predicted a significant impact of short-term low oxygen treatment on MSC differentiation and optimal chondrogenic differentiation at 10-11% P_{O2}. Considerably much less work has been done in the area of investigation of mass transport within 3D scaffolds. Cioffi et al. performed a combined macro-scale/micro-scale computational study to quantify oxygen transport and flow-

mediated shear stress to human chondrocytes cultured in three-dimensional poly(ethylene glycol terephthalate)/poly(butylene terephthalate) (PEGT/PBT) foam scaffolds in a perfusion bioreactor system.(Cioffi, Kuffer et al., 2008) A volumetric consumption rate based on Michaelis-Menten kinetics for oxygen consumption by avian cartilage cells was applied in this study (with the microscopic part of the model accounting for porosity of the volume). The Cioffi et al. model predicted small local oxygen variations within the scaffold micro-architecture. At the two flow rates examined the higher flow rate of 0.3 mL/min was found to maintain the oxygen supply throughout the scaffold above anoxic levels (>1%) within 99.5% of the scaffold, while at the lower flow rate of 0.03 mL/min 6% of the scaffold (mostly in the vicinity of its periphery) would be supplied with 0.5%-1% O_2.

II. SCAFFOLD MANUFACTURING

II.1 LITERATURE REVIEW

II.1-a Scaffold Materials

A wide variety of materials may be appropriate for an ideal bone graft substitute. Metals (stainless steel, titanium and/or its alloys), ceramics (hydroxyapatite), glass, natural polymers (hyaluronic acid, starch-based polymer matrices), and synthetic polymers (polyurethane foams, poly(lactic acid) (PLA), poly(glycolic) acid (PGA), and their copolymer poly(lactic acid-glycolic acid) (PLAGA)) are just some of the materials used for bone tissue engineering scaffolds. Among these materials, some synthetic polymers are biodegradable and biocompatible, and can be produced industrially in large quantities. Additionally, synthetic polymers are very versatile in the ways that they can be customized in order to introduce structural, biological and biomechanical signals that are necessary for sufficient and durable tissue growth. Moreover, some of the lactic acid isomers and copolymers are approved for human clinical use by the Food and Drug Administration (FDA) and do not have the potential to elicit an immunological or clinically detectable foreign body reaction. Therefore they have become the front runner materials for engineered scaffolds for bone tissue.

For a more in-depth discussion see reviews of polymeric scaffolds in bone tissue engineering by D.W. Hutmacher(Hutmacher, 2000) and by X. Liu and P.X. Ma,(Liu and Ma, 2004); a review of biodegradable synthetic polymers by Gunatillake and Adhikari(Gunatillake and Adhikari, 2003); chapters on polymeric scaffolds for tissue engineering applications by D.M. Yoon and J.P. Fisher (Yoon and Fisher, 2006) and a

review of synthetic degradable polymers utilized for osteogenic drug delivery by Holland and Mikos(Holland and Mikos, 2006).

II.1-b Physiological Need for Porosity

Porosity (percentage of void space in a solid) and pore size are two important geometric characteristics that can be controlled during the process of the scaffold manufacturing. An interconnected porous geometry of the scaffold is necessary for cell migration, proliferation, vascularization and nutrient/waste transport. Additionally, it improves mechanical interlocking between the implant and the surrounding natural bone upon implantation. The internal geometry of the scaffold also determines the mechanical properties of the engineered tissue and is thought to affect the rate of degradation under perfusion.(Agrawal, McKinney et al., 2000)

In vitro, lower porosity stimulates osteogenesis by suppressing cell proliferation and forcing cell aggregation, while in vivo, higher porosity and pore size result in greater bone in-growth (but in diminished mechanical properties). Relatively larger pores favor direct osteogenesis, since they allow vascularization and high oxygenation, while smaller pores result in osteochondral ossification. The minimum pore size required to regenerate mineralized bone is generally considered to be ~100 μm, whereas large pores (100–300 μm) show substantial bone in-growth and smaller pores (75–100 μm) result in in-growth of unmineralized osteoid tissue. Only fibrous tissue penetrates smaller pores (10–75 μm) However, for non-load-bearing conditions the 100μm does not seem to be the critical pore size, since all pore sizes show similar bone in-growth. For comparison, in human tibial condyles, the porosity for cancellous bone has been measured to range between 61% and 90% (with a linear increase with age).(Ding et al., 2002) Since the rat is a

standard small animal model for modeling osteoporosis, it is also of value for comparison.(Laib et al., 2000) Wistar rat cancellous bone porosity was measured to be about 78-83% for control and 91% after 23 days of tail suspension.(Laib, Barou et al., 2000)

For a more in-depth discussion of porosity of 3D biomaterial scaffolds and osteogenesis see a review by Karageorgiou and Kaplan.(Karageorgiou and Kaplan, 2005)

II.1-c Scaffold Manufacturing Methods

The ultimate scaffold-engineering goal is to produce scaffolds that meet specific mechanical, mass-transport, and external-shape requirements. Therefore, a design must be determined and the manufactured scaffold must replicate the design.

According to a review by S.J. Hollister, (Hollister, 2009) there are two basic categories of scaffold manufacturing methods: designed controlled and nondesigned controlled. Non-designed controlled methods include emulsion, solvent diffusion, non-woven fiber mesh (melt blowing, electrospinning), gas foaming (CO_2) and porogen leaching. These methods are very proficient at creating highly porous scaffolds with fine structural features of variable size scales (with the smallest being on the order of 1μm). Features of such scales are beneficial for seeding cells into scaffolds, and can be used for controlled release of growth factors via degradation. Limited control over the 3D scaffold architecture can be attained by changing porogen size and shape, freezing conditions, organic solvents, polymer melt concentration, or electrospinning fiber collection. However, the ultimate effects of these parameters can only be determined after the scaffold has been made. Thus, significant deviations in reproducibility and anisotropies of effective mechanical and mass-transport properties can occur. Finally, it is

generally not possible to utilize these techniques to produce complex 3D anatomically shaped scaffolds.

Designed Controlled (Rapid Prototyping) methods include: stereo lithography, nozzle deposition, laser polymerization, laser sintering and printing techniques. These technologies process material layer-by-layer using a variety of physical processing methods. They are driven by a contour created by slicing a surface representation of the design. Complicated external anatomic shapes and complex internal porous architectures can be created using these techniques; however, they are more expensive and require hardware that is not easily accessible. The lower feature limit of design controlled techniques is typically 200 to 500μm.

Blending design- and nondesign-controlled techniques may be done sequentially, by first creating scaffolds by design controlled and then applying nondesigned-controlled methods, or simultaneously, by performing both manufacturing techniques together. Although this type of compromise between the two categories of the manufacturing methods holds the most potential for the future of scaffold manufacturing, at this time, it is not trivial to do.

II.2 EXPERIMENTAL SETUP

II.2-a Foam Scaffold Manufacturing

Porous foam scaffolds were prepared in the Sikavitsas laboratory using solvent casting/particulate leaching method (Mikos et al., 1994; Lu et al., 2000; Liu and Ma, 2004; Alvarez-Barreto and Sikavitsas, 2007). Briefly, poly(L-lactic acid) (PLLA, 114,500 MW, 1.87 PDI, Birmingham Polymers) was dissolved into chloroform 5% w/v. The solution was then poured over a bed of sodium chloride crystals. Solvent was allowed to

evaporate for 24h. The resulting salt-polymer composite was inserted into an 8 mm diameter cylindrical mold and compressed at 500 psi. During compression, the composite was heated to 130 °C and held at constant temperature and pressure for 30 min. The resulting composite rod was cut into 2.3 mm thick discs using a diamond wheel saw (Model 650, South Bay Technology, Inc.). The discs were placed into de-ionized water (DIH_2O) under agitation for 2 days to leach out NaCl. Entire DIH_2O volumes were replaced twice per day. Leached discs were then removed from DIH_2O and placed under vacuum to remove moisture from the scaffolds. The resulting product was 8 mm diameter, 2.3 mm thick discs (see Figure 1).

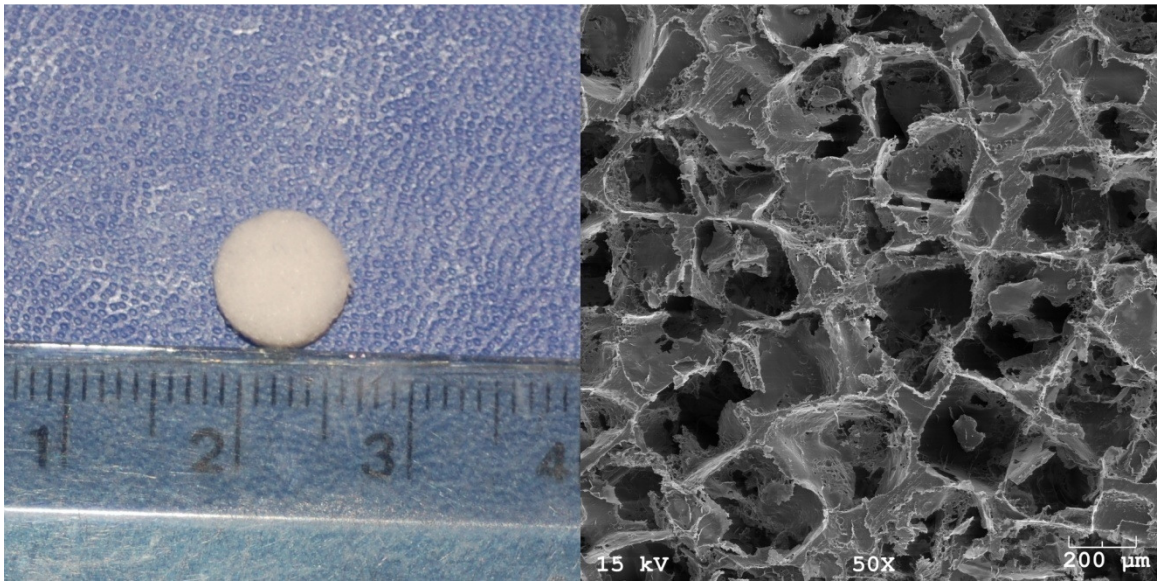

Figure 1 LEFT PANEL: a representative PLLA scaffold (ruler is in cm). RIGHT PANEL: SEM image of a PLLA scaffold showing its complicated internal structure (50X magnification, scale bar is 200 µm). Image from (Voronov et al., 2010).

Porosity of scaffolds was determined by measuring the solid volume (mass of the scaffold divided by the density of PLLA) and comparing to the total scaffold volume (assuming a cylindrical scaffold shape). Combinations of typical ranges of pore size (180-250µm, 250-355 µm, and 355-450 µm) and porosity values (80%, 85%, 90%, and

95%) were created for this study by sifting out salt grain sizes and by controlling the amount of salt added to the polymer solution, respectively.

II.2-b Nonwoven Fiber Mesh Scaffold Manufacturing

Nonwoven fiber mesh scaffolds were constructed using PLLA micro-fibers produced with the technique known as spunbonding in the Shambaugh laboratory (Majumdar and Shambaugh, 1990; Malkan, 1995; Zhang et al., 1997; de Rovere and Shambaugh, 2001; Tandler et al., 2001). A schematic of the spunbonding apparatus is shown in Figure 2.

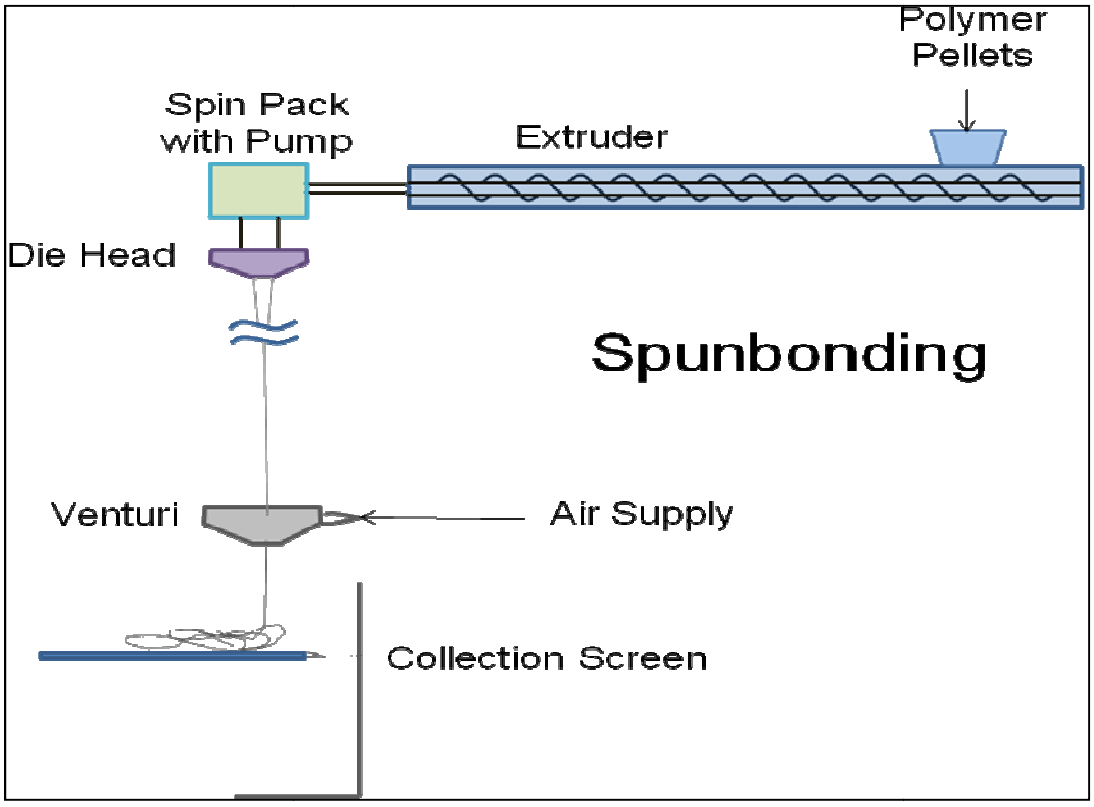

Figure 2 Schematic of the spunbonding apparatus used to produce PLLA nonwoven fiber meshes for scaffolds. Image from (VanGordon et al., 2010)

In spunbonding, a hot polymer melt is extruded from a heated die and then fed through a high speed air venturi to attenuate the polymer strand to a fine diameter fiber. The polymer used in the production of fibers was PLLA (grade 6251D, 1.4% D

enantiomer 108,500 MW, 1.87 PDI, NatureWorks LLC.) A custom Brabender extruder of 19.1 mm (0.75 in.) diameter and 381 mm length was used to melt and pressurize the polymer. The barrel of the extruder had a 20:1 L/D ratio and a 3:1 compression ratio. The polymer exiting from the extruder was then fed to a modified Zenith pump which pumped controlled quantities of molten polymer through a heated die which has a single polymer capillary of 0.420 mm inside diameter. The die assembly was heated using two 250 W cartridge heaters. Polymer flow rates were varied from 0.13 to 0.81 g/min. The polymer strand exits the die and feeds through an air venturi 100 cm below the die nozzle. Room temperature air flow to the venturi was measured and controlled using a rotameter. During spunbonding, a collection screen was placed 175 cm below the die face. The collection screen was manually circulated in order to obtain even layering of the fibers. This procedure resulted in a random lay down of fibers known as nonwoven. Layers of fibers were stacked and measured until the stack reached a mass of 9.0 ± 0.1 g within an area of 162.8 cm^2. From the collected nonwoven fiber stack, a center cut sheet having a 7cm diameter was collected. This procedure was the same as that used by de Rovere and Shambaugh (de Rovere and Shambaugh, 2001) Finally using an 8 mm diameter die, discs were punched from the layered 7 cm diameter fiber sheets. The resultant scaffolds were ~85% porous with an 8 mm diameter and ~2.3 mm thickness. Collected fiber diameters were measured optically using a Nikon HFX-II microscope. Eleven fiber diameters were taken and averaged for each sample. For the nonwoven fiber scaffolds produced for this study, the average diameter of the fibers was 34.8 ± 1.85 μm. Porosity was determined by the same method as porous foams.

III. NON-DESTRUCTIVE X-RAY SCAFFOLD IMAGING

This section describes the methodology involved in acquiring micro CT images of the scaffolds: image processing, filtering, segmentation and 3D reconstruction.

III.1 MICROCOMPUTED TOMOGRAPHY (μCT)

Micro-Computed Tomography (μCT) is a nondestructive method of creating a virtual image of a 3D object by capturing images of its cross-sections via X-Ray beams, which allows for preservation of the imaged constructs for subsequent histological analysis. The term micro denotes that the resolution, or the distance between pixels, of the cross-sectional projections is on the order of microns. Therefore, μCT is predominately used for small samples, such as in-vivo studies on small animals. It has been shown that weekly sequential μCT imaging revealed a consistent increase in total matrix mineralization volume over time in culture, demonstrating that multiple scans did not eliminate the cells' ability to produce mineralized matrix. Furthermore repeated scanning of bone tissue engineering scaffolds did not significantly reduce mineralized matrix formation by the seeded cells.(Cartmell et al., 2004) Therefore, μCT presents not only a method for preserving the sample after the experiment, but also an opportunity to image the culturing process itself without significantly affecting the outcome of the experiment. For a comparison of μCT with other techniques used in the characterizations of scaffolds see a review by S.T. Ho and D.W. Hutmacher.(Ho and Hutmacher, 2006)

Figure 3 ScanCo VivaCT40 (ScanCo Medical, Bassersdorf, Switzerland; http://www.scanco.ch) used in this study is shown on the left side.

ScanCo VivaCT40 (ScanCo Medical, Bassersdorf, Switzerland; http://www.scanco.ch), shown in Figure 3, was used to obtain 10µm and 42 µm resolution 2D intensity image slices using settings of an intensity of 88 µA, and an energy of 45 kV. Each slice was stored in a form of a 16 bit grey scale Tagged Image File Format (TIFF) image, in which each pixel contained information about its intensity. All scans were done at 300 ms integration time, 2-fold frame averaging. These settings were found to give the best quality images for the PLLA scaffolds (by trial and error).

III.2 IMAGE FILTERING, SEGMENTATION & 3D RECONSTRUCTION

Images produced by the μCT scanner are "grey scale" intensity images represented by a pixel map where every element has a value corresponding to how bright/dark the pixel at the position in question should be displayed. MATLAB® is used for image processing of acquired μCT slices. The scans were thresholded using a global thresholding technique (a single threshold is picked for the entire reconstructed volume), which resulted in the porosity of the scaffolds being within 1% of the experimentally measured values. Porosity was determined experimentally by measuring the solid volume (mass of the scaffolds divided by the density of PLLA) and the total volume (assuming a cylindrical scaffold).

Although μCT is a relatively accurate imaging method, it is liable to produce noise and ring artifacts. In order to reduce artifacts in the acquired μCT images, the "nearest neighbor filter" is applied by setting pixels to a value of zero if they are touching only one pixel, or not touching any other pixels, that have a non-zero value. After filtering has been applied, the 2D μCT images are stacked in 3D using an in-house Matlab® code in order to produce a 3D reconstruction of the scaffold geometry via Tecplot 360® visualization software, such as the ones depicted in Figure 4.

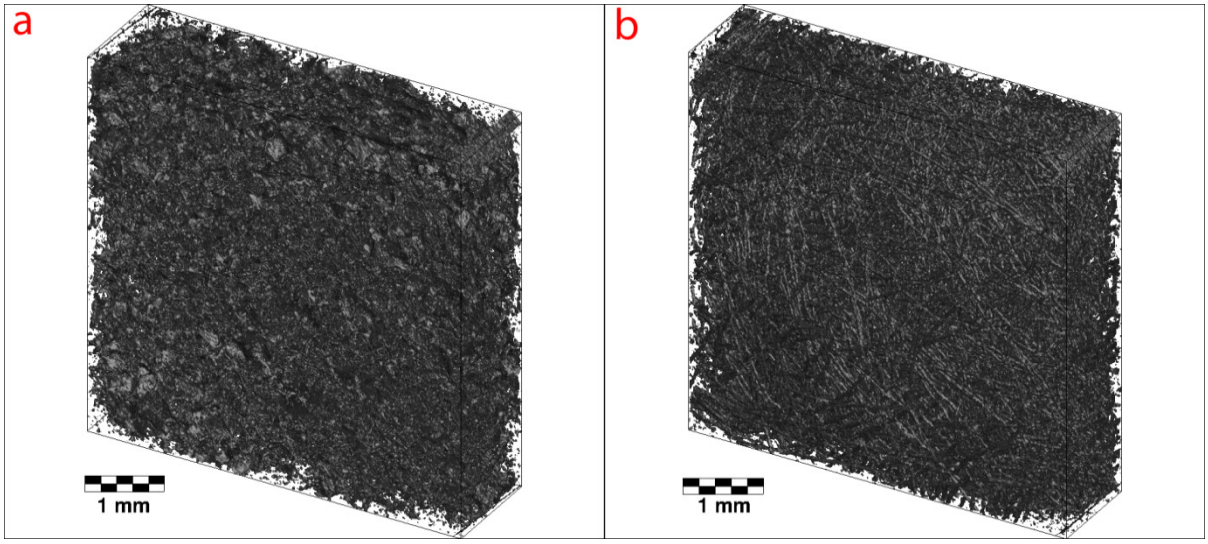

Figure 4 Matlab® 3D reconstructions of μCT imaging of a)porous foam scaffold created by solvent casting/particulate leaching and b)nonwoven fiber mesh scaffold created by spunbonding. Image from (VanGordon, Voronov et al., 2010).

For every scaffold, a single cuboid portion was cut out from the center of the digital reconstruction, in order to avoid end effects in the flow simulations. The exact size of the reconstruction "cut-out" was different for each scaffold. A typical reconstruction can be seen in the left side of Figure 4, with a representative size of 5.502 mm x 5.544 mm x 1.974 mm.

III.3 SURFACE AREA CALCULATION ALGORITHM

The images obtained from μCT consist of pixels, and when the slices are reconstructed in 3D the reconstruction consists of voxels (which are analogous to pixels in 2D). Since the inter-pixel distance and the inter-slice distance is the same, the 3D reconstruction is effectively a cubic lattice with solid and empty space nodes (after global thresholding). Therefore shapes that may not be cubic in nature are represented cubically on this lattice and the surface area calculation is not exact. In order to illustrate the

problem, the surface area calculation in 2D for a simple example of a circle is illustrated below:

Consider the 2D analogy of a micro computed tomography image after thresholding shown in Figure 5, which is essentially a binary image with red representing solid and white representing empty space. Assuming that the red object in the image is actually the blue circle whose perimeter it is desired to measure (since perimeter is the 2D analogy of surface area), but its shape is not known a priori, it would is possible to take one of several approaches. Namely, one could approximate the perimeter of the blue circle by summing the "surface" perimeter of all solid (red) nodes that are marked with diagonal black stripes (i.e., any solid node that has a perpendicularly neighboring empty space node).

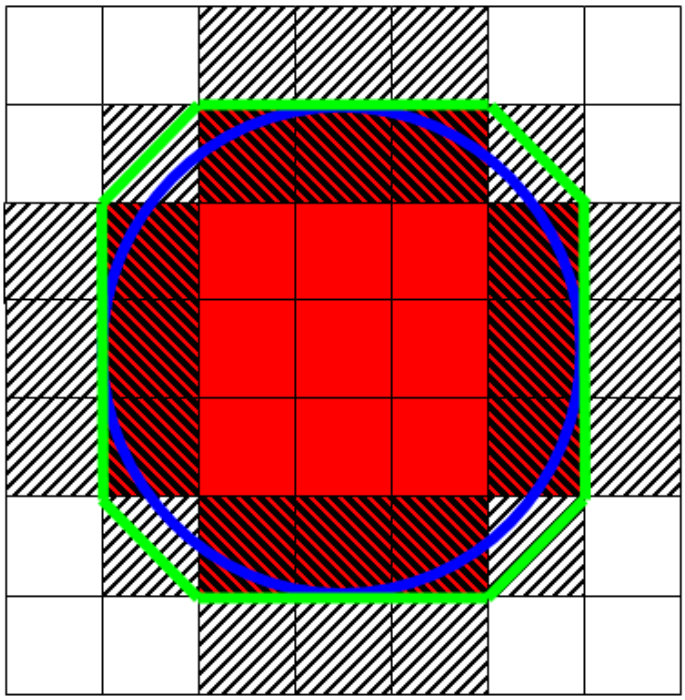

Figure 5 Estimation of a circle's perimeter from a 2D square lattice representation (analogy of surface area estimation in three dimensions). Marked in red are the solid nodes representing the actual object, white nodes are empty space, diagonal stripes indicate "surface" nodes. Blue is the actual object in question and green is a "diagonal" estimation of its perimeter. Image from (Voronov, VanGordon et al., 2010).

Assuming that each pixel is a square with a unit side in arbitrary units, the true perimeter of the circle would be $5\pi \approx 15.7$. The *"surface" perimeter* method gives 20, which is an overestimate of the actual answer (and serves as the upper limit, because it treats the circle as if it is composed of blocks).

Another way of estimating the perimeter is to assign a unit length to each of the "surface" nodes and then sum up the lengths. For the *sum of all solid "surface" nodes* (red with diagonal black stripes) is 12 and the *sum of all empty space "surface" nodes* (white with diagonal black stripes) is 16. Even though the latter is very close to the actual answer, with higher lattice resolution both the solid and the empty space "surface" node sums converge on the same answer (which happens to be an underestimate of the true perimeter, because this method arbitrarily reduces the perimeter of each "surface" node to unity). Finally, a more accurate method of estimating the perimeter is to sum up the green lines, where a *diagonal approximation* is used for the perimeter of the diagonally touching solid nodes. This method gives an answer of $12 + 4 * \sqrt{2} \approx 17.66$, which is close to the actual answer and remains to be the best estimate even with increasing lattice resolution (in 3D a more involved analogy of this method is used, but the idea is the same).

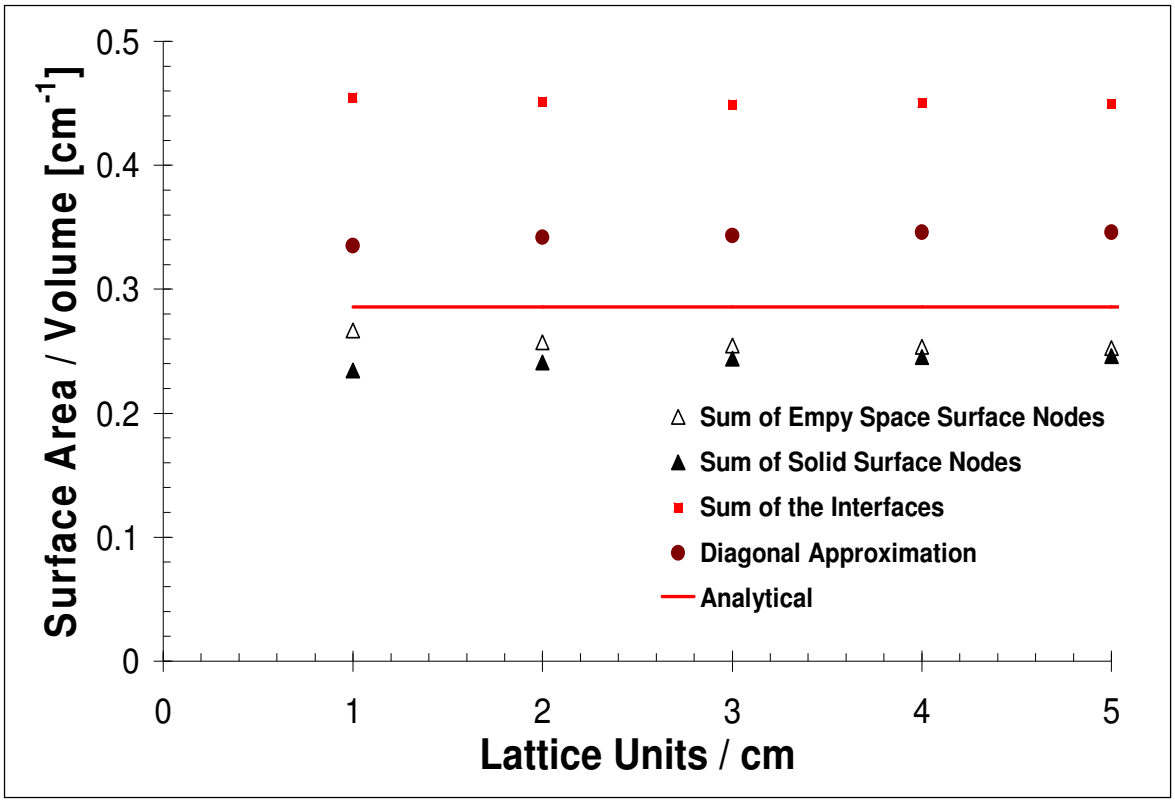

Figure 6 Estimation of surface area per volume ratio of a 20 cm diameter sphere using various methods. Image from (Voronov, VanGordon et al., 2010).

Figure 6 shows how these methods compare for the case of a sphere in three dimensions. Note that volume is computed simply by summing up the solid nodes. The analytical solution for the surface to volume ratio for a sphere can be simply found from theory to be 3/R, where R is the radius of the sphere.

It can be seen that as the sphere representation in lattice units becomes more and more refined (the lattice units per cm ratio goes up), these methods converge upon their respective answers. The 3D analogy of summing *"surface" perimeter* method (herein dubbed as the *"sum of the interfaces"*) provides the upper limit for the surface-to-volume ratio. Both the *sum of all solid "surface" nodes* and the *sum of all empty space "surface" nodes* converge on a single value with increased resolution, which is an underestimate of the analytical solution for a sphere. The 3D analogy of the *diagonal approximation*

method is closer to the analytical solution than *sum of the interfaces*, but is still an overestimate. Therefore, the average of the *diagonal approximation* and of the *sum of the surface nodes (average of fluid and solid)* methods is used as the best estimate of the surface area.

In order to calculate the surface area-to-*solid* volume ratio (a.k.a. specific surface area), S, the surface area is surface area is divided by the sum of the solid voxels in the 3D reconstruction.

$$S = \frac{Surface\,Area}{Solid\,Volume} = \frac{SurfaceArea}{\sum Solid\,Voxels} \tag{1}$$

In order to calculate the surface area-to-*total* volume ratio, the specific surface area is multiplied by one minus scaffold porosity.

$$\frac{Surface\,Area}{Total\,Volume} = \frac{SurfaceArea}{Solid\,Volume}\left(1 - \frac{Empty\,Volume}{Total\,Volume}\right) = S(1-\varepsilon) \tag{2}$$

III.4 GEOMETRIC CHARACTERISTICS OF THE SCAFFOLDS FROM μCT

Although the μCT imaging of the scaffolds is required in order to provide simulation geometry for the fluid shear stress and mass transport simulations, μCT is also a useful tool for obtaining geometric characteristics of the scaffolds.

III.4-a Foam Scaffolds

The surface area-to-volume ratio allows the calculation of the amount of surface area available for cell attachment and tissue deposition (assuming that the cells have been seeded uniformly throughout the scaffold and have arranged themselves into a monolayer). It has been previously related to increased proliferation of human OPC1

osteoblasts seeded on alumina and β-tricalcium phosphate ceramic scaffolds.(Bose et al., 2003) Therefore surface area-to-volume ratio is an important geometric property of the tissue engineering scaffolds. Table 3 summarizes the average surface area per volume ratio as a function of porosity and NaCl grain size of the foam PLLA scaffolds obtained from μCT.

Table 3 Surface area / solid volume ratio as a function of porosity and NaCl grain size, expressed in cm^{-1}.

NaCl Grain Size (μm)	porosity = 80%	porosity = 85%	porosity = 90%	porosity = 95%
180 - 250	286	316	363	430
250 - 355	296	340	380	420
355 - 450	220	240	300	346

From the data appearing in Table 3 it is apparent that the surface area-to-volume ratio for foam scaffolds becomes larger with increased porosity. To an extent this is also true for the decreasing NaCl grain size. For comparison, in human tibial condyles the surface area-to-volume ratio for cancellous bone was measured to range between 83 and 356 cm^{-1} (with a linear increase with age, which also corresponded to an increasing porosity).(Ding, Odgaard et al., 2002) Wistar rat cancellous bone surface area-to-volume ratio was measured to be about 228-248 cm^{-1} for control, and the tail suspension did not seem to affect the ratio with the values remaining fairly constant at 270-277 cm^{-1} throughout 23 days of the experiment.(Laib, Barou et al., 2000)

III.4-b Non-Woven Fiber Scaffolds

The fiber diameter of non-woven fiber mesh scaffolds can serve as a verification of the μCT imaging technique (since it can be measured via other methods) and it is also an important geometric characteristic of the scaffolds. The average fiber diameter for the nonwoven fiber mesh scaffold was obtained by three different methods for comparison:

1) based on the surface area-to-solid volume ratio using Equation (3); 2) by fitting circles to fiber cross-sections on the μCT images using a Matlab® boundary tracing technique (see Appendix - III); 3) optically by using a microscope.

The first method for measuring the fiber diameter is based on the surface area-to-solid volume ratio. The surface area-to-solid volume ratio (or the "specific surface area") of a cylinder (ignoring end effects) is given as

$$S = \frac{4}{D} \tag{3}$$

where D is the fiber diameter. This means that by measuring the surface area-to-solid volume ratio of fibers in the non-woven fiber mesh scaffold via μCT one can back-calculate the fiber diameter of the scaffolds using Equation (3).

Secondly, it is possible to examine the 2D slices of the nonwoven fiber mesh scaffolds obtained through different planes of the scaffolds via μCT. The idea is that if a fiber is oriented perpendicular to the plane of the μCT slice then its cross-section will appear as a circle in the image and it can be used to estimate the fiber diameter via a circle fit. The circle fitting approach is illustrated in Figure 7, where the perpendicular fiber cross-sections are marked in green color.

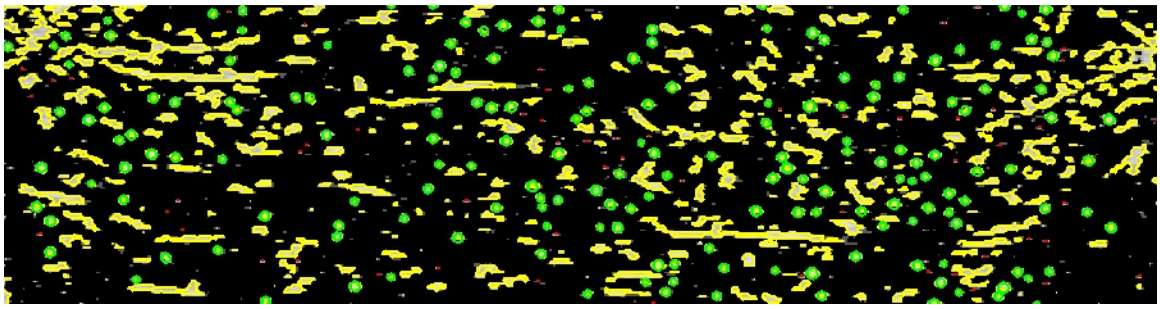

Figure 7 Illustration of the circle fitting method of estimating the fiber diameter. The algorithm examines the fiber cross-sections that appear in the 2D μCT slice. The noncircular objects are marked in yellow or red and are rejected. The fiber cross-sections that are circular in shape are marked in green. The green circles are used in order to obtain the mean fiber diameter show in Table 4.

The circle fitting algorithm examines the fiber cross-sections that appear in the 2D μCT slice. The noncircular objects are marked in yellow and are rejected. The fiber cross-sections that are circular in shape are marked in green. The green circles are used in order to obtain the statistics regarding the fiber diameter. For example, a histogram of fiber diameters for a single nonwoven fiber mesh scaffold is shown in Figure 8.

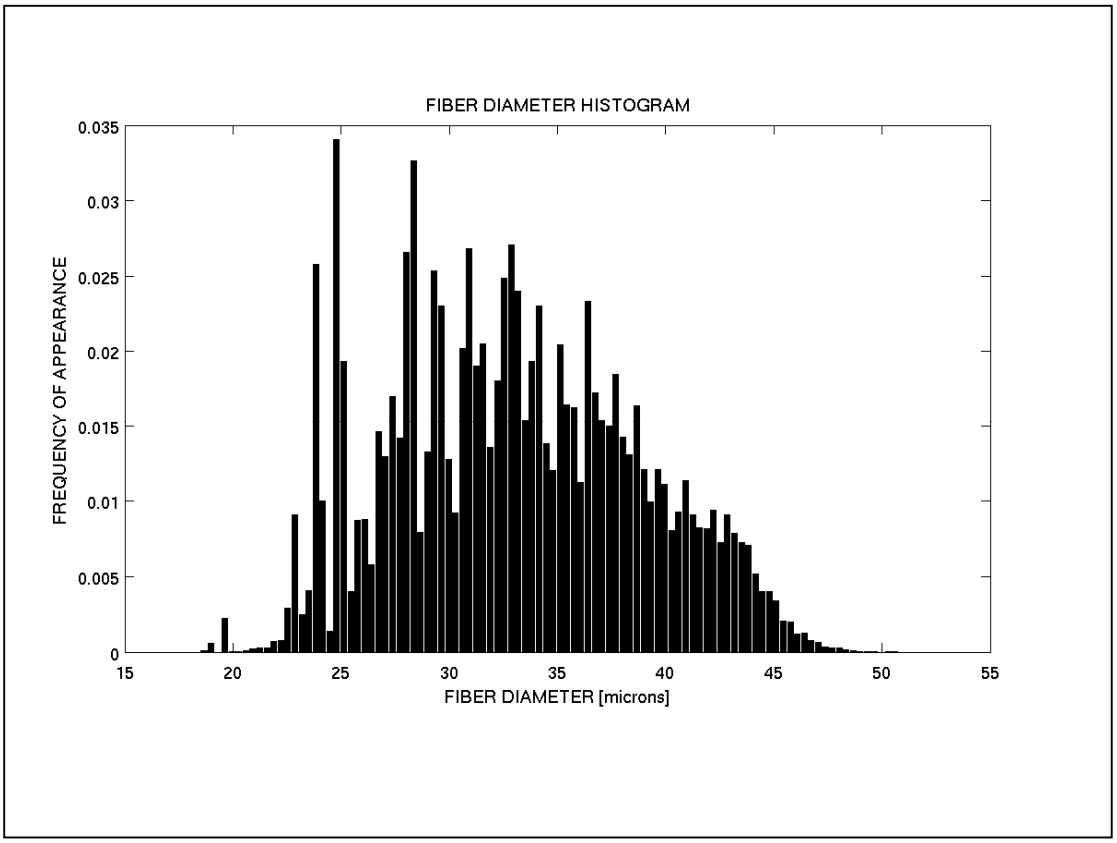

Figure 8 A sample histogram of fiber diameters for a nonwoven fiber mesh scaffold obtained using the circle fitting method.

Finally, the diameters of the collected fibers were measured optically using a Nikon HFX-II microscope. Eleven fiber diameters were taken and averaged for each sample. Table 4 is a comparison and a summary of the fiber diameter results for all of the methods.

Table 4 Scaffold comparison based on geometric characteristics.

	Nonwoven Fiber Mesh
Void Fraction	0.85
Surface Area / Solid Volume [cm^{-1}]	1046.47
Surface Area / Total Volume [cm^{-1}]	157.33
Mean Diameter From Specific Area [microns]	38.22
Mean Diameter From Edge Detection [microns]	33.01 ± 5.73
Mean Diameter From Microscope [microns]	34.8 ± 1.85

The mean diameter of the PLLA fibers obtained from the surface area measurement in Table 4 corresponds well to the mean diameter values measured by the other methods. This further validates the accuracy of the global threshold chosen for μCT image segmentation, as well as the correctness of the surface area algorithm.

IV. SIMULATION METHODOLOGY

IV.1 FLUID SHEAR STRESS - LATTICE BOLTZMANN METHOD

IV.1-a Background

The Lattice Boltzmann Method (LBM) is a numerical technique for simulating fluid flow that consists of solving the discrete Boltzmann equation.(Chen and Doolen, 1998; Succi, 2001; Sukop et al., 2006) In addition to computational advantages [e.g., LBM is inherently parallelizable on high-end parallel computers,(Kandhai et al., 1998; Wang et al., 2005), LBM techniques have been used in a wide spectrum of applications [turbulence, (Cosgrove et al., 2003) non-Newtonian flow (Gabbanelli et al., 2005; Boyd et al., 2006; Yoshino et al., 2007), and multiphase flow (Swift et al., 1996)]. More importantly, for the present application, LBM is especially appropriate for modeling pore-scale flow through porous media (such as bone tissue) due to the simplicity with which it handles complicated boundaries.

IV.1-b Algorithm

During the past decade, LBM has been accepted as a 2nd order accurate numerical method for modeling hydrodynamics.(Chen and Doolen, 1998). The Boltzmann equation is an evolution equation for a particle distribution function that is calculated as a function of space and time (McNamara and Zanetti, 1988) as follows:

$$f_i(\vec{x}+\vec{e}_i\Delta t, t+\Delta t) = f_i(\vec{x},t) + \Omega_i(\vec{x},t) \pm ff_i \quad (4)$$

where f is the particle distribution function, $\vec{x}$ is position, t is time, Δt is the time step, $\vec{e}$ is the microscopic velocity, Ω is the collision operator, ff is the forcing factor and the subscript 'i' is a lattice direction index. The terms on the right hand side of Equation (4)

constitute the three steps of the LBM algorithm, namely the streaming, collision and forcing steps. During the streaming step, the particle distribution function f at position x and time t moves in the direction of the velocity to a new position on the lattice at time $t+\Delta t$. The collision step subsequently computes the effect of the collisions that have occurred during the movement in the streaming step and is considered a relaxation towards equilibrium. Several collision models are available, and we use the simplest and most common, i.e., the single-relaxation time approximation of the collision term given by Bhatnagar, Gross and Krook. (Bhatnagar et al., 1954) The collision operator is approximated as

$$\Omega_i(\vec{x},t) = -\frac{1}{\tau}(f_i - f_i^{eq}) \tag{5}$$

The particle equilibrium distribution function, f^{eq}, is given by

$$f_i^{eq}(\vec{x}) = w_i \rho(\vec{x}) \left[1 + 3\frac{\vec{e}_i \cdot \vec{U}}{c^2} + 9\frac{(\vec{e}_i \cdot \vec{U})^2}{c^4} - \frac{3}{2}\frac{\vec{U}^2}{c^2} \right] \tag{6}$$

where $c=\Delta x/\Delta t$ is the lattice speed, Δx is the lattice constant, w is a lattice specific weighing factor (w_0 = 2/9, $w_{1\text{-}6}$ = 1/9, $w_{7\text{-}14}$ = 1/72), ρ is local density and U is the macroscopic velocity. The time τ appearing in Equation (2) is the time scale with which the local particle distribution function relaxes to equilibrium. It is related to the kinematic viscosity of the fluid as

$$\nu = \frac{1}{3}\left(\tau - \frac{1}{2}\right) \tag{7}$$

During the forcing step of the algorithm, a pressure drop is specified by adding a forcing factor, *ff*, to the fluid particle distribution function components moving in the positive stream-wise direction and by subtracting it from those moving in the negative x direction.

The final step in the LBM algorithm is to calculate the macroscopic properties of the fluid such as density, ρ, and velocity, U, at any instant from the conservation equations of mass and momentum given by

$$\rho = \sum_{i=0}^{n} f_i \tag{8}$$

$$\rho \vec{U} = \sum_{i=0}^{n} f_i \vec{e}_i \tag{9}$$

where n is the number of allowable directions that the fluid particles are allowed to move (i.e., 14 in the D3Q15 lattice used here), in addition to the zero position, which is the rest position that a fluid particle can stay when it does not move. A custom-written, in-house code was developed for this work. The 3D, 15-velocity lattice (D3Q15) for LBM, (Qian et al., 1992) was used to perform the simulations.

The simulation lattice consists of N_x, N_Y and N_Z nodes in the x, y and z directions, respectively (for a representative volume of interest shown in Figure 4 a high resolution μCT scan results in a 188 x 524 x 528 lattice). LBM is especially appropriate for modeling pore-scale flow through porous media (such as bone tissue) due to the simplicity with which it handles complicated boundaries. Among the lattice nodes, *fluid* nodes are those within the flow field (i.e., within the empty pore space) and *wall* nodes are those that make up the rigid wall. The fluid particle distribution is simply zero for all wall nodes, obviating the need to use elaborate meshing techniques near the boundaries. The no-slip boundary condition is applied at the wall faces using the bounce-back technique.(Sukop, Thorne et al., 2006)

IV.1-c Shear Stress Calculation

The calculation of the shear stress was done following the scheme suggested by Porter et al.(Porter, Zauel et al., 2005) The cell culture media was assumed to be a Newtonian fluid and the shear stresses within the scaffold were estimated as

$$\underline{\underline{\tau}} \approx \mu\left(\frac{1}{2}\right)\left(\nabla\vec{U} + \nabla\vec{U}^{T}\right) \tag{10}$$

where $\underline{\underline{\tau}}$ is the shear stress tensor, and $\vec{U}$ is the velocity vector. The fluid dynamic viscosity was assumed to be 0.01 g / cm s, which is close to minimum essential media, supplemented with 10% Fetal Bovine Serum (FBS) typically used in cell culturing experiments.(Lakhotia and Papoutsakis, 1992) The first derivatives of the velocity field are calculated using the 2nd order accurate centered difference approximation at each fluid voxel, as long as the backward and forward neighbors of that voxel are also fluid voxels.

$$U'(x_i) = \frac{U(x_{i+1}) + U(x_{i-1})}{2h} + O(h^2) \quad \text{where h = 1 lattice unit} \tag{11}$$

In case that one of the neighbors is a solid voxel, the fluid-solid boundary is located half way between the solid and the fluid node due to the bounce-back boundary condition in LBM. In order to handle the non-equispaced data a second-order Lagrange interpolating can be differentiated in order to estimate the derivative of velocity.

$$U'(x) = \frac{2x - x_i - x_{i+1}}{(x_{i-1} - x_i)(x_{i-1} - x_{i+1})}U(x_{i-1}) + \frac{2x - x_{i-1} - x_{i+1}}{(x_i - x_{i-1})(x_i - x_{i+1})}U(x_i) + \frac{2x - x_{i-1} - x_i}{(x_{i+1} - x_{i-1})(x_{i+1} - x_i)}U(x_{i+1}) \tag{12}$$

If it is the forward neighbor that is a solid, Equation (12) reduces to

$$U'(x) = -\frac{U(x_{i-1})}{3} - U(x_i) \tag{13}$$

And for the case of the backward solid neighbor, Equation (12) reduces to

$$U'(x) = U(x_i) + \frac{U(x_{i+1})}{3} \tag{14}$$

For the case where both the forward and the behind neighbor are solid voxels, the derivative of velocity is set to zero.

A symmetric strain matrix is formed from the obtained partial derivatives for each fluid voxel, and the eigenvalues of the rate of strain matrix were found using the Jacobi method.(Fletcher and Srinivas, 1991) The largest absolute-value of the three eigenvalues obtained at each fluid voxel is selected, corresponding to the largest stress value for that voxel. The bulk stresses are averaged over all non-solid nodes in the simulation, whereas the surface stresses are averaged over all non-solid nodes that have a solid nearest neighbor node. The results of the shear stress calculation using the approach described above are shown in Figure 9 for the case of pressure driven flow in a channel.

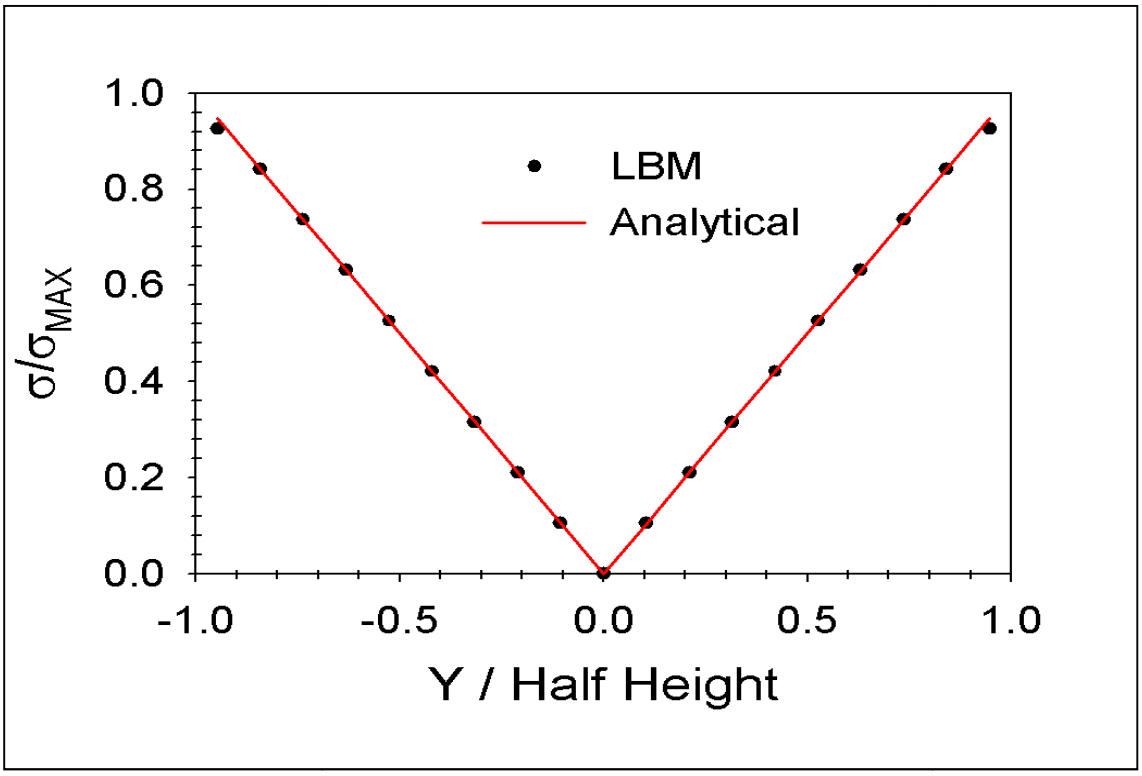

Figure 9 Validation of the shear stress calculation procedure: Stress fields for flow through a 19 cm channel at $\Delta P/L = 1\times10^{-9}$ g / cm^2 s^2 calculated from LBM. Image from (Voronov, VanGordon et al., 2010).

IV.1-d Parallelization

Computationally, LBM is very attractive due to its effective and inherently parallelizable numerical algorithm. The code used for this work is an in-house Fortran 90 code that has been parallelized with Message Passing Interface (MPI). Each MPI process works on a chunk of the problem (data parallelism), while keeping a "ghost" copy of its nearest neighbor's boundaries for implementation of the boundary conditions. Traditionally, in parallel implementations of the LBM method, the MPI computational domain is decomposed using one of two ways: "slice, box, and cube" partitioning scheme or "recursive bisection" techniques, although other approaches such as the "cell based" methods have been proposed.(Wang, Zhang et al., 2005) We have implemented an algorithm that allows for the program to choose between the slice (1D), the box (2D) and the cube (3D) partitioning scheme depending on the problem dimensions, such that the load balance is optimized by this choice. Since the scaffolds have an isotropic porosity in all three dimensions throughout the whole computational domain, this method is expected to achieve sufficient load balance. Figure 10 illustrates the "box" partitioning scheme as an example of MPI parallelization.

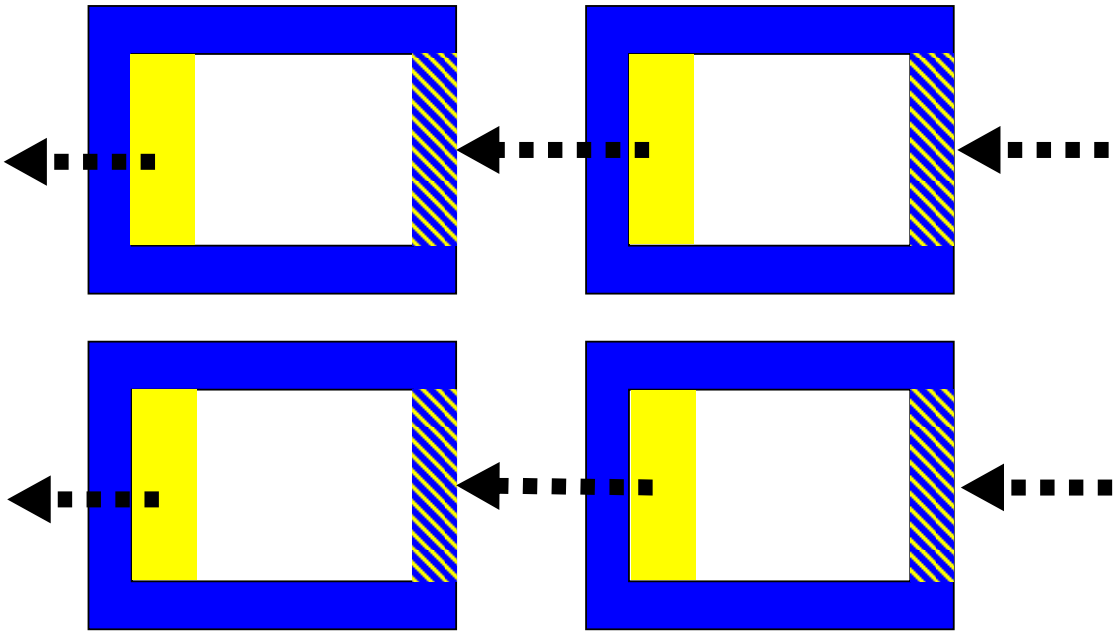

Figure 10 Example of MPI parallelization in 2D. Initially the problem is divided in the X and Y dimensions between four MPI processes. White - nodes that have been updated by the LBM calculation; Blue - boundary "ghost" nodes, which cannot be updated without MPI communication because implementation of boundary conditions requires the presence of nearest neighbors. Yellow and shaded blue colors show MPI communication taking place in the X dimension: shaded "ghost" cells are updated from right to left. Likewise, the "ghost" nodes will be updated from left to right, such that all the blue "ghost" nodes become shades (i.e. updated with the most current values from the neighboring MPI process). After all the "ghost" nodes have been updated in the X directions, the procedure is repeated in the Y directions (up-down and down-up).

The "speedup" is a common measure of performance in supercomputing. It refers to how much a parallel algorithm is faster than a corresponding nonparallel algorithm, and is defined by Equation (15).

$$Speedup_P = \frac{Non\ Parallel\ Execution\ Time_1}{Parallel\ Execution\ Time_P} \quad \text{where p is number of processes} \qquad (15)$$

Linear speedup occurs when the speedup increases linearly with the number of MPI processes $\left(Speedup_P = p\right)$ and is considered to be very good scalability. The speedup for the LBM code is plotted in Figure 11.

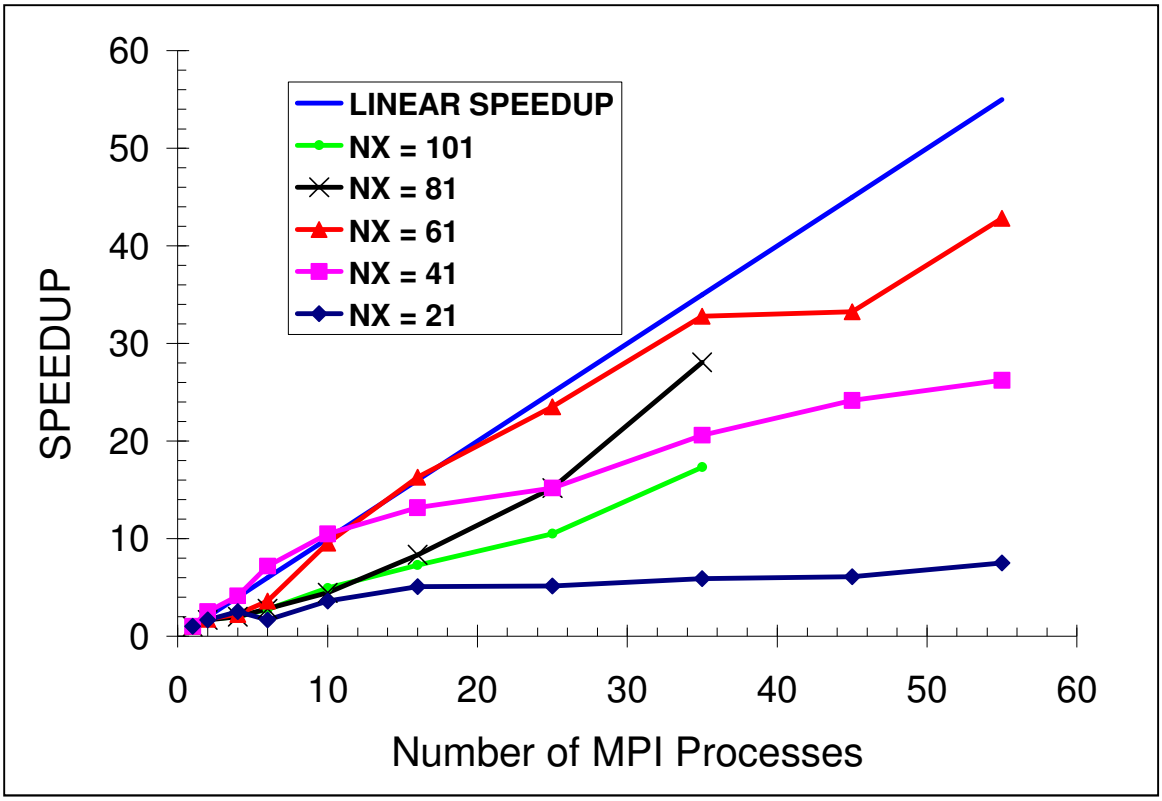

Figure 11 Speedup performance for LBM code as a function of number of MPI Processes for different simulation box sizes (NX is number of nodes along one side of the cubic simulation domain), as measured on Lonestar supercomputer. (Code is compiled with the Intel 9.1 compiler and -O3 -xT compiler optimization options. Nodes are interconnected with InfiniBand technology in a fat-tree topology with a 1GB/sec point-to-point bandwidth. NX is simulation box side size)

From Figure 11 it can be concluded that the LBM code displays very good scalability at large problem sizes. This makes sense because the LBM code is a memory dominated problem. Therefore, as the problem is broken up into smaller pieces along processes, the scalability improves. Of course as the number of processes becomes very large, it is expected that the communication time will dominate. However, for the number of processes tested in Figure 11, this threshold was not reached. What this means the cost of parallelization is justified by the benefits that come from it, especially for large problem sizes.

IV.1-e Validation

The LBM code results have been validated for three different geometries for which analytical solutions are available: forced flow in a channel, in a pipe, and flow through an infinite array of spheres. Some of the validations are discussed below.

For forced flow in an infinite channel the LBM code was found to reproduce the analytical profile that is expected from theory accurately (see Equation (16) and Figure 12).

$$U_x(y) = \frac{\Delta P}{L}\frac{b^2}{2\mu}\left[1-\left(\frac{y}{b}\right)^2\right] \qquad \text{where b is the channel half-height} \tag{16}$$

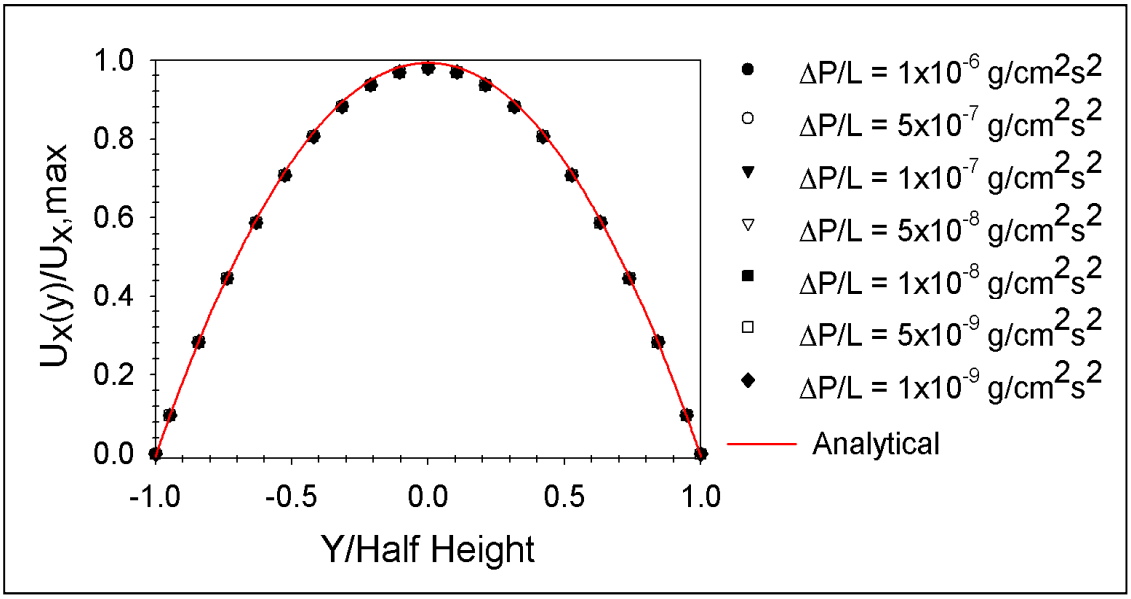

Figure 12 Poiseuille flow in infinite channel with a width of 19 cm as a function of pressure drop and comparison to theory. $U_{X,MAX}$ occurs when y=0 in Equation (16). Image from (Voronov, VanGordon et al., 2010).

Similarly, results for forced flow in a pipe for various pipe sizes and pressure drops compared well with the analytical solution [see Equation (17) and Figure 13].

$$U_x(r) = \frac{\Delta P}{L}\frac{R^2}{4\mu}\left[1-\left(\frac{r}{R}\right)^2\right]$$ where R is radius of the pipe (17)

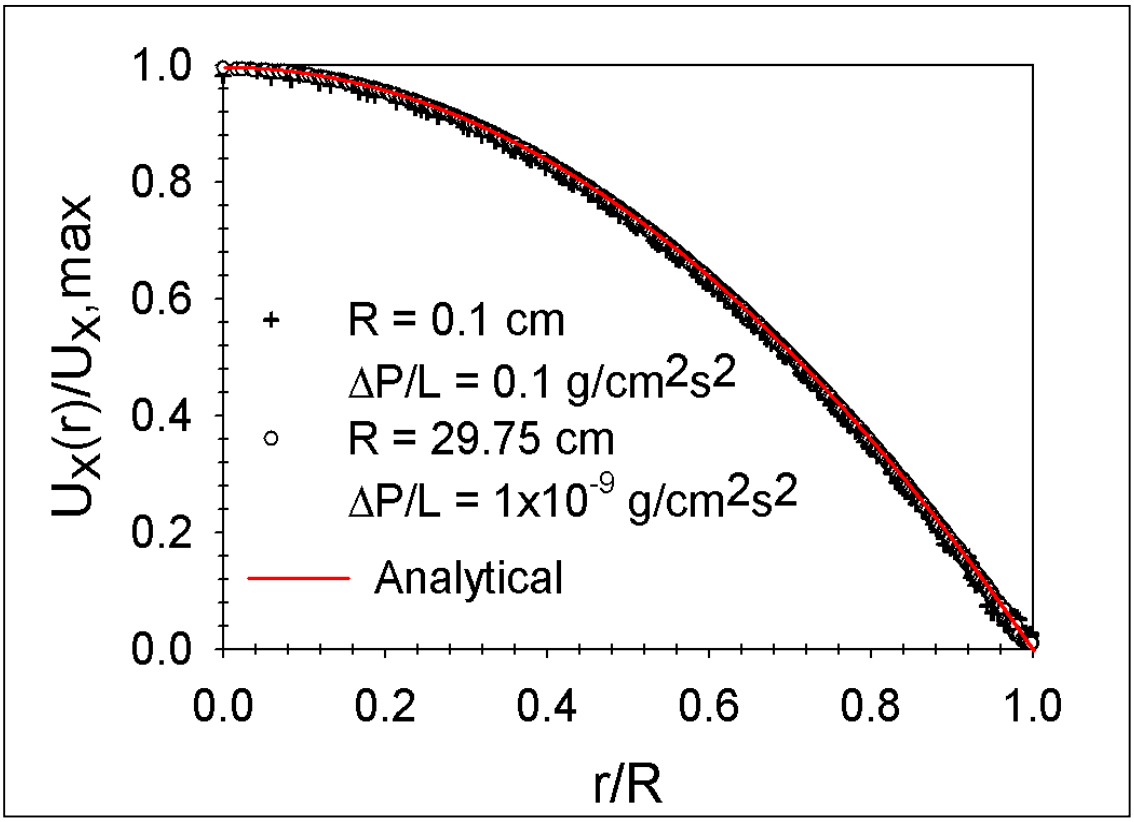

Figure 13 Poiseuille flow in a pipe as a function of pressure drop and pipe radius (comparison to theory). $U_{X,MAX}$ occurs when r = 0 in Equation (17) . Image from (Voronov, VanGordon et al., 2010).

Finally, since the application of interest is flow through porous media, the LBM code was validated for the case of flow through an infinite array of spheres. The Blake-Kozeny (BK) equation is applicable to this type of flow and one can use it to validate the simulation results.(Bird et al., 2002) The BK equation is a special case of Darcy's Law that linearly correlates the pressure drop across a porous medium to the superficial velocity of the fluid (i.e., the velocity that the fluid would have if the porous medium was totally open to flow), and is represented as

$$U_S = \frac{\Delta P}{L}\frac{D_{SPHERE}^2}{150\mu}\frac{\varepsilon^3}{(1-\varepsilon)^2}$$ (18)

where D_{SPHERE} is the sphere diameter, μ is the fluid dynamic viscosity, and ε is the porosity. The value 150 of the coefficient that appears in the BK equation has been obtained through experiments. It is seen in Figure 14 that the simulations recover the value of the coefficient as the cubic lattice resolution is increased.

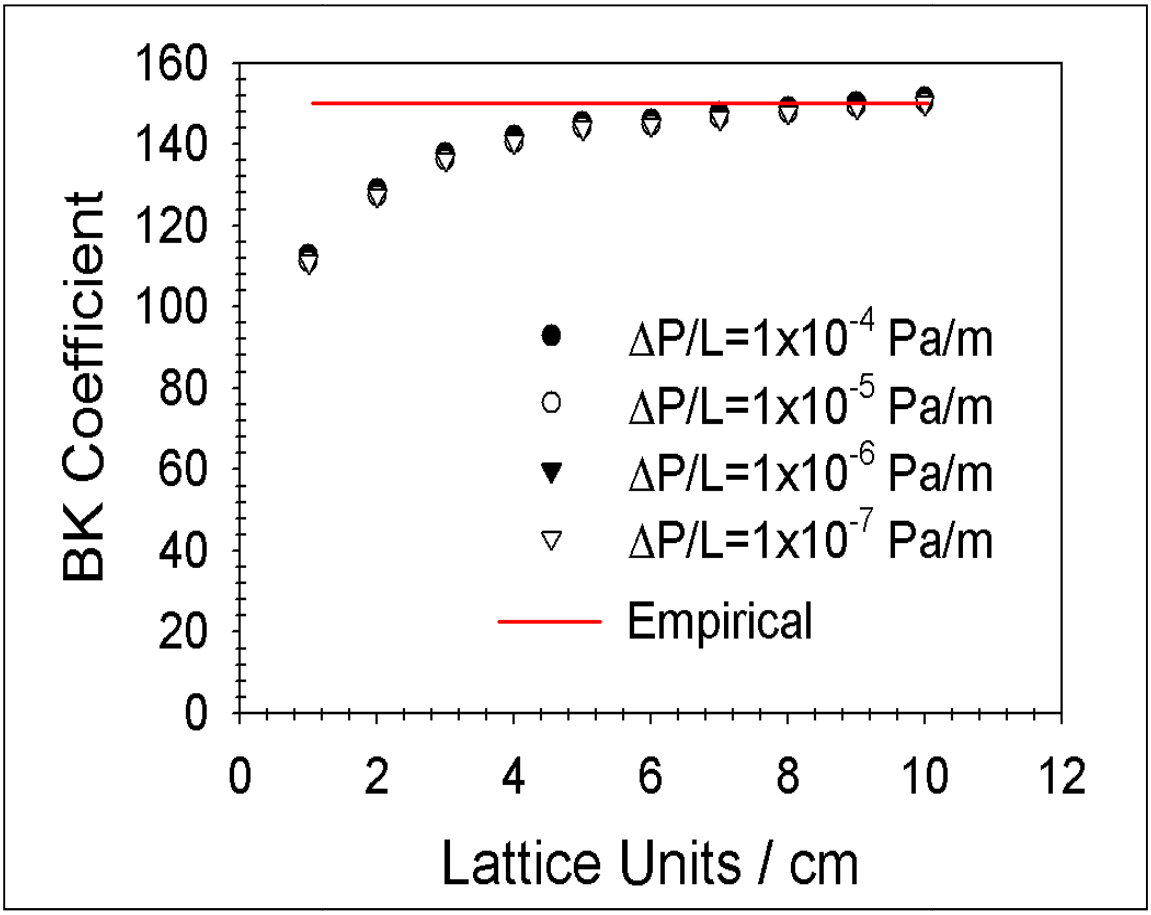

Figure 14 Blake Kozeny coefficient for flow in an infinite array of spheres with D_P = 20cm as a function of pressure drop and lattice resolution. Image from (Voronov, VanGordon et al., 2010).

Figure 15 is a visualization of simulation results for pressure driven flow through an infinite array of spheres obtained from LBM.

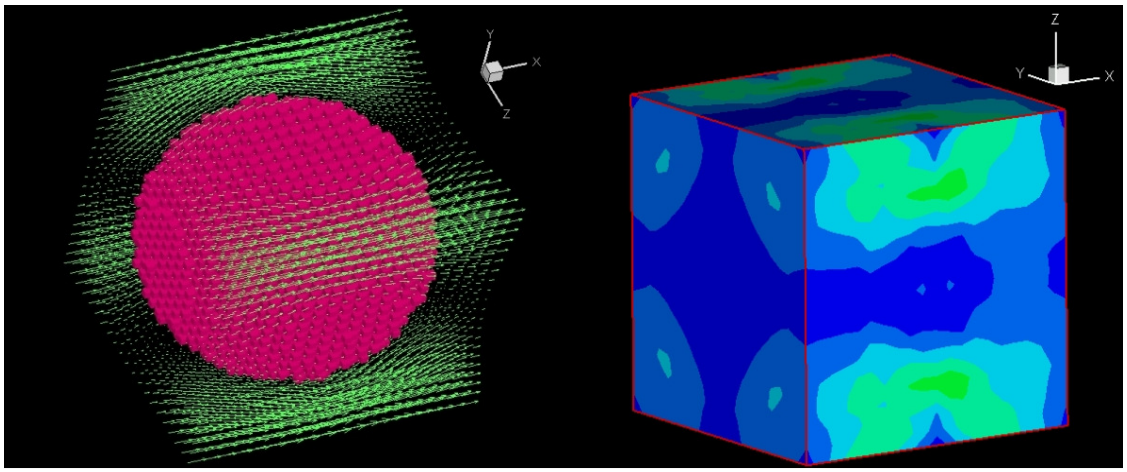

Figure 15 Visualization of simulation results for pressure driven flow through an infinite array of spheres (Left - velocity field; Right - stress field).

IV.1-f Accuracy

In order to test the accuracy of the three different LBM lattices (D3Q15, D3Q19, and D3Q27), Poiseuille flows in a channel and in a pipe were performed for each lattice type and the obtained velocity and stress profiles were compared to analytical solutions by calculating the absolute error (expressed as a percentage of maximum velocity or maximum stress, respectively) using Equation (19). Percent error was not used for quantifying accuracy because it diverges at true values of zero.

$$\mathrm{Re}\,duced\,Absolute\,Error = 100\% \frac{\left|Experimental\,Value - True\,Value\right|}{True\,Value_{MAX}} \tag{19}$$

A small channel is chosen because the lattice resolution of the velocity field inside it would be more representative of a scaffold pore, which would also not have a very large resolution. Figure 16 is a plot of the average absolute error in the streamwise velocity as a function of vertical distance from the center of the channel.

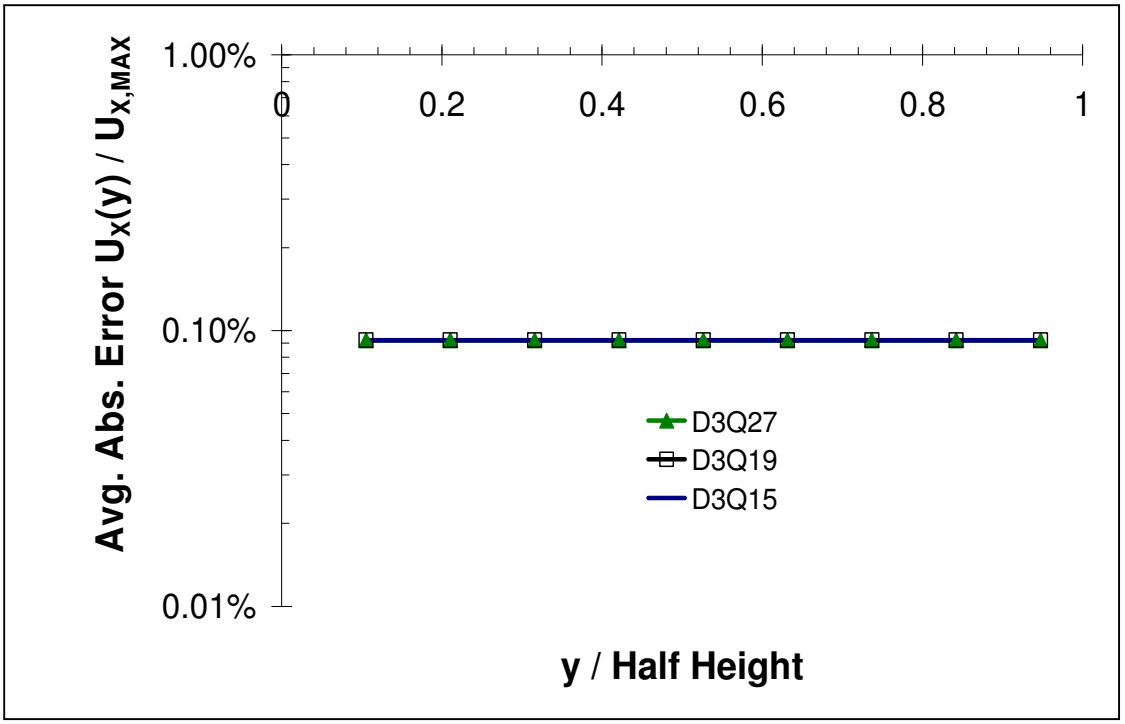

Figure 16 Average absolute error in streamwise velocity relative to analytical solution (expressed as a percentage of $U_{X,MAX}$) as a function of the dimensionless vertical position for Poiseuille flow in a channel for different LBM lattices. Channel height = 19cm and $\Delta P/L = 1x10^{-6} g/cm^2s^2$. The simulation domain consisted of 21x21x21 nodes. The theoretical maximum streamwise velocity at the center of the channel is 0.0045 cm/s.

From Figure 16 it is apparent that the absolute error in the streamwise velocity relative to the analytical solution does not seem to depend on the LBM lattice type for this particular geometry. The fact that the absolute error remains constant while the value of velocity decreases closer to the wall means that there is more error there (at the wall the error is about 1% of the maximum velocity in the channel). This error stems from the bounce back boundary condition in LBM. Since stresses are of ultimate interest to the study, the absolute error in fluid stress as a function of the vertical distance away from the channel's center is plotted in Figure 17.

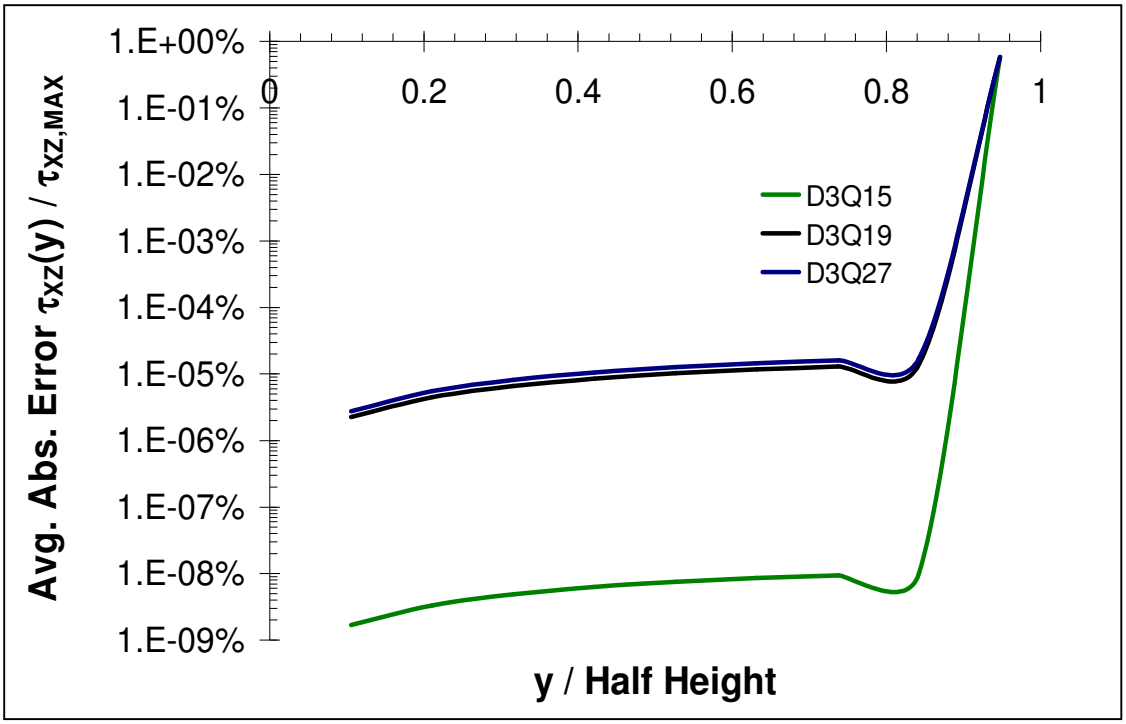

Figure 17 Average absolute error in fluid stress relative to analytical solution (expressed as a percentage of $\tau_{XY,MAX}$) as a function of the dimensionless vertical position for Poiseuille flow in a channel for different LBM lattices. Channel height = 19cm and $\Delta P/L = 1x10^{-6} g/cm^2s^2$. The simulation domain consisted of 21x21x21 nodes. The theoretical maximum fluid stress at the channel wall is $9.5x10^{-6}$ g/cm^2s^2.

From Figure 17 it is apparent that error in fluid stress also worsens near the wall, yet remains low (error near the wall is two magnitudes less than the theoretical value). This is again due to the bounce back boundary condition in LBM, since the error in velocity propagates itself into the stress results. Surprisingly, the D3Q15 lattice gives the more accurate results for this particular geometry. Next, the accuracy of the three LBM lattices is compared inside of a pipe with a fine lattice resolution. This presents the opportunity to examine the accuracy of LBM in a more curved geometry with a finer lattice representation. The percent error results at each lattice node were binned as a function of distance away from center of the pipe and averaged in each bin. They are shown in Figure 18.

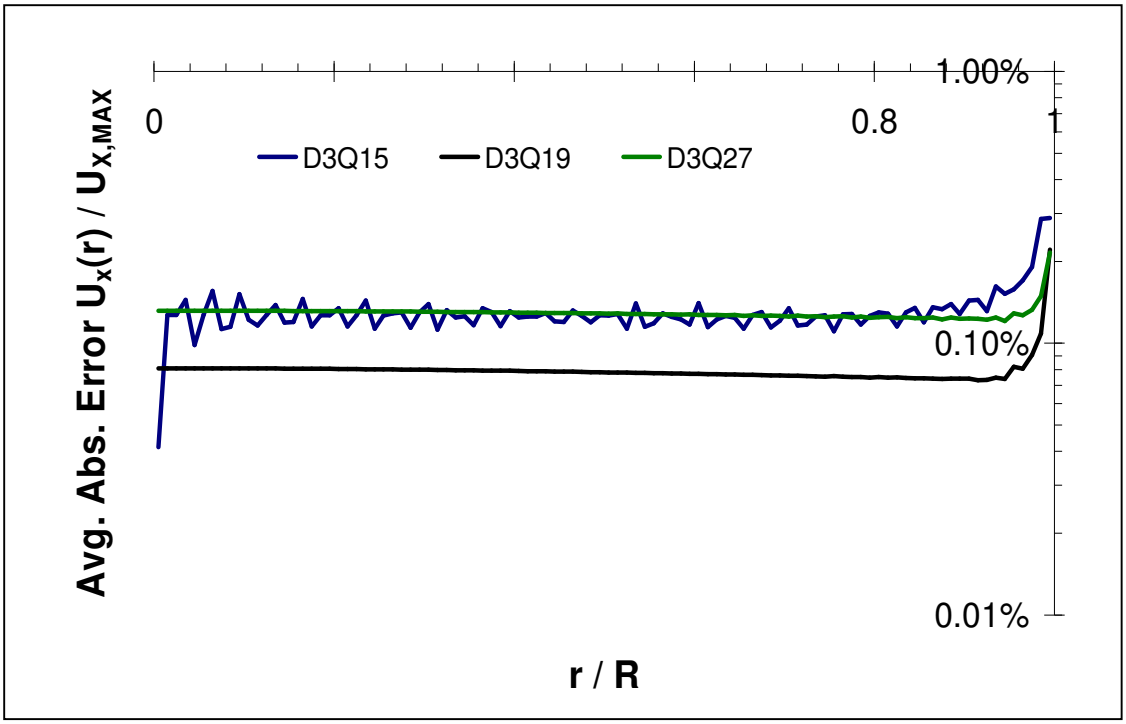

Figure 18 Percent error in streamwise velocity relative to analytical solution as a function of the dimensionless radius for Poiseuille flow in a pipe for different LBM lattices. Pipe radius = 9.5cm and $\Delta P/L = 1x10^{-6} g/cm^2s^2$, corresponding to an average Re = 2.15. The simulation domain consisted of 5x201x201 nodes and was performed on 16 MPI processes on the Lonestar supercomputer. The % error was binned and averaged in each bin as a function of distance from the center, where the bin size was 0.01. The theoretical maximum streamwise velocity at the center of the pipe is 0.0023 cm/s.

From Figure 18 it is apparent that there is not a significant difference in streamwise velocity accuracy between the three LBM lattice types (with D3Q19 having a slight advantage). Also, it is apparent that the accuracy worsens near the wall. This is expected because the curved geometry of the pipe is represented by the cubic LBM lattice, and is expected to improve with increased lattice resolution of the modeled geometry. In a sense, the pipe with its 2D curvature (or the sphere its 3D curvature) correspond to the worst case scenarios, since their true geometries are ideally curved. Thus, the pipe is somewhat of a conservative test for accuracy. Since, the ultimate desired result from the LBM simulation is the surface stress that would be experienced by

the cells attached to the scaffold, Figure 19 is a plot of average % error versus the distance away from the center of the pipe.

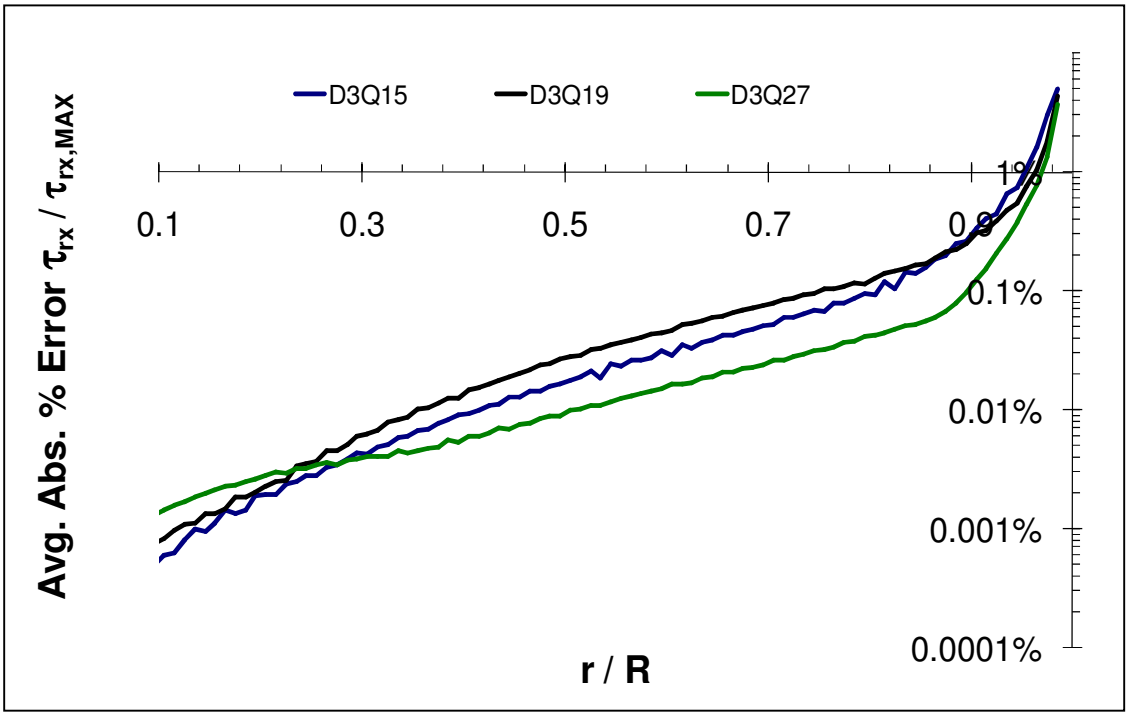

Figure 19 Average absolute error in fluid stress (expressed as percentage of maximum stress) relative to analytical solution as a function of the dimensionless radius for Poiseuille flow in a pipe for different LBM lattices. Pipe radius = 9.5cm and $\Delta P/L = 1x10^{-6} g/cm^2s^2$, corresponding to an average Re = 2.15. The simulation domain consisted of 5x201x201 nodes and was performed on 16 MPI processes on the Lonestar supercomputer. The % error was binned and averaged in each bin as a function of distance from the center, where the bin size was 0.01. The theoretical maximum fluid stress at the pipe wall is $4.75x10^{-6}$ g/cm^2s^2.

From Figure 19 it is apparent that there is not a significant difference in fluid stress accuracy between the three LBM lattice types. Also, it is apparent that the accuracy worsens near the wall. The % error in fluid stress contains the compound error from both the error in the velocity field from LBM due to cubic lattice representation of the curved pipe geometry and from the bounce back boundary conditions, as well as the error that arises from numerically differentiating the velocity field in order to obtain the fluid stress. Since the percent error equation diverges when the theoretical value is zero, the results near the center of the pipe are omitted.

Table 5 summarizes the LBM accuracy and performance profiling results. From it, it is apparent that there is not a significant difference in accuracy between the three lattices, yet the lattice with a smaller memory footprint (i.e. the D3Q15 lattice with the least directions) is the one that is more computationally efficient. Therefore, the D3Q15 lattice is the lattice of choice for all LBM simulations in this study.

Table 5 RMS of % error and average time for one LBM step on for the conditions given in Figure 18 as a function of LBM lattice type.

LBM Lattice	RMS of Abs. Error in $U_x(r) / U_{X,MAX}$	RMS of Abs. Error in $\tau_{rx}(r)/ \tau_{MAX}$	Average Time for LBM Step (sec)
D3Q15	0.13%	1.83%	0.0438
D3Q19	0.08%	1.71%	0.0553
D3Q27	0.13%	1.49%	0.0785

IV.1-g Simulation Details

The typical scaffold obtained from the 3D reconstruction of the μCT scan resulted in a simulation domain of 188 x 524 x 528 nodes. The fluid dynamic viscosity was 0.01 g / (cm s), which is close to the value for culture media that is typically used in cell culturing experiments.(Lakhotia and Papoutsakis, 1992) The forcing factor was such that flow rates of 0.5 or 1mL/min through the scaffolds were achieved, which are typical for a perfusion bioreactor (Sikavitsas, Bancroft et al., 2003; Sikavitsas et al., 2005). The LBM simulation was performed at a Courant Number of 0.0005. Convergence was determined by monitoring the change in the average and maximum streamwise velocities every 1,000 LBM steps. The convergence tolerance was set to 0.001%. It took the LBM simulations roughly 70,000 LBM steps in order to satisfy the convergence tolerance. The calculation of the shear stress was conducted following the scheme suggested by Porter et al.(Porter, Zauel et al., 2005), in which the largest eigenvalue of the shear stress tensor at any location is calculated.

The presence of the cells was assumed to not affect the flow field significantly (this is a good assumption for the at least the first week of culturing). Moreover, the fluid-induced shear stresses acting on the internal area of the scaffold pores were assumed to be an estimate of the shear stresses acting on the membranes of the cells (this further implies that cells are seeded uniformly throughout the scaffold). Finally, the scaffold structure was assumed to be rigid and not affected by the fluid flow.

IV.2 Nutrient Transport - Lagrangian Scalar Tracking

Constant replenishment of nutrients and oxygen within the scaffolds also dramatically benefits the bone cell growth.(Allori, Sailon et al., 2008) Due to the complicated architecture of the pore space of the scaffolds, theoretical prediction of tissue growth is impractical, making simulation the method of choice for the calculations. The Lattice Boltzmann method (LBM) has proven to be a useful and computationally efficient tool for modeling flows through complicated geometries such as porous media. However, it is inherently an Eulerian framework method. Solute transport (an inherently Lagrangian process) with the addition of a chemical reaction is a problem of practical interest for a multitude of disciplines. Lagrangian Scalar Tracking (LST) is an efficient Lagrangian method methodology for performing reactive solute transport simulations (Papavassiliou and Hanratty, 1995; Papavassiliou, 2002) based on a velocity field obtained from the LBM. It uses a novel technique for tracking passive mass markers that can react with the solid boundary which allows the exploration of the whole spectrum of first order heterogeneous reaction rates with just a single simulation. Therefore, consumption of oxygen and/or nutrients within porous scaffolds typically used in perfusion bioreactors is modeled using LST.

IV.2-a Background

Fluid flow in porous media is a problem of practical interest with numerous applications, such as flow through rocks, soils, biological tissue (e.g., bones), and man-made materials like cements and ceramics. Mathematical description of flow within the pore space in porous media is difficult because of the geometrical complexity of the medium. Traditional models rely on space-averaged properties that lose meaning at the pore scale. Recently, LBM (Succi, 2001; Sukop, Thorne et al., 2006) - a numerical technique with intrinsic parallelism, and straightforward resolution of complex solid boundaries and multiple fluid phases - has gained popularity for its ability to provide results that can be equivalent to the solution of the Navier-Stokes equations for single-fluid and multi-fluid flow through porous media.(Chen and Doolen, 1998)

Besides having a complex geometry, numerous flows through porous media applications, such as contaminant transport in soil, geologic sequestration of carbon dioxide, and bioremediation, require the modeling of local mass transfer and chemical reaction. Thus, the problem becomes a multi-scale one, as well as a multi-process one (advection, diffusion, and chemical reaction). Several methods exist for modeling solute transport in porous media: for example in multi component LBM the second component can mimic a solute, when its non-local interaction with the bulk fluid is grossly reduced, while for reactive systems, the LBM boundary condition can be modified to account for the mass consumed by a heterogeneous reaction.(Sukop, Thorne et al., 2006; Kang et al., 2007) Alternatively, hybrid models exist for reaction-diffusion systems, which spatially couple LBM to a finite difference discretization of partial differential equations.(Van Leemput et al., 2007)

These methods are based on the Eulerian framework. Useful statistical quantities, such as the solute survival distance, effective diffusion coefficient, collision frequency, etc. cannot be extracted directly from such simulations. Moreover, just as in the case of classical LBM, the range of solute diffusivity that can be modeled is limited by the instability of the numerical algorithm as the relaxation time for the solute or 'j' component, τ_j, approaches $1/2$: the diffusion coefficient $D_j = 1/3\left(\tau_j - 1/2\right)$ is directly analogous to the definition of kinematic viscosity for single phase fluids [see Equation (7)].(Kang, Lichtner et al., 2007)

An alternative approach for simulating solute transport in porous media is to use the velocity field results produced by LBM simulation in conjunction with LST. Similar techniques have been applied in our laboratory for heat transfer in microfluidics (Thummala, 2004; Papavassiliou, 2006) and by others for the simulation of the motion of nanoparticles in low Reynolds number flows(Bhattacharya et al., 2009). The fundamental hypothesis is that solute transport behavior of passive markers is the combination of convection (obtained using the velocity field from the LBM simulations) and diffusion (obtained from a mesoscopic Monte-Carlo approach that simulates Brownian motion). The LST simulation technique has been developed based on this concept that involves the tracking of trajectories of passive scalar markers in a flow field, and then applying simple statistical methods to extract information about the macroscopic concentration field. The presence of these markers does not affect the flow field, and they do not interact with each other.

This method is resourceful in terms of computational efficiency and simplicity. Its advantages include the ability to simulate various Schmidt number solutes (the

Schmidt number is defined as $Sc = \frac{\nu}{D}$, where ν is kinematic viscosity and D is mass diffusivity) and different solute release modes with a single solvent flow field obtained from an LBM simulation. In addition, LST allows the simulation of a whole spectrum of solute reaction rates, also using just a single flow field obtained from LBM.

IV.2-b Algorithm

The concept of LST is a familiar one, if one is acquainted with a classical Molecular Dynamics (MD) simulation. In classical Molecular Dynamics, an *N*-body system interacts with some specified forces, which more or less affect all the bodies in the system (ignoring bodies beyond a certain distance is a simplifications usually done for computational efficiency). Thus, when a body feels a certain force inflicted on it by the rest of the bodies in the simulation, with knowledge of its mass, the body's acceleration can be computed as well as the velocity. Once the velocity is known, the body moves to a new position, and the forces (which are a function of the body's positions) are recomputed for the next body and so on.

Similarly to MD, the Lagrangian scalar tracking method follows bodies that change positions. However, the bodies are passive (i.e., they do not affect the flow field and are therefore referred to as markers), so they move through a previously solved velocity field, when the flow is steady and laminar. The trajectories of these markers are determined by a convective part (obtained using the velocity field from the LBM simulations) and a diffusion part (i.e., Brownian motion obtained from a mesoscopic Monte-Carlo approach).

The new position of a marker at time $t+1$ is calculated from the previous position $\vec{X}$ at time t based on its convection and diffusion, as given by the equation

$$\vec{X}_{t+1} = \vec{X}_t + \Delta t * \vec{U}_t + \Delta \vec{X} \tag{20}$$

where $\vec{U}_t$ is the fluid velocity at the marker location at time *t*. The velocity of the marker is calculated from the velocity of the fluid obtained from the LBM simulation by an interpolation scheme (either trilinear or tricubic interpolation from the 8 nearest nodes of the cubic lattice produced by LBM, where the velocity at the wall nodes is assumed to be zero).(Lekien and Marsden, 2005) As mentioned above, although the markers are convected by the fluid they do not affect the flow field, and the numerical experiments presented here simulate the transfer of a passive scalar.

The rate of molecular dispersion in one direction, say the *x* direction, is proportional to its diffusivity, as described by Einstein's theory for Brownian motion (Einstein, 1905)

$$\lim_{t\to\infty} \frac{d\left\langle \Delta X_i(t)^2 \right\rangle}{dt} = 2dD \tag{21}$$

The random diffusion of markers follows a normal distribution with a zero mean and standard deviation σ, as denoted by $\mathrm{N}(0,\sigma)$. The molecular dispersion in each one direction has a standard deviation that is given by $\sigma = \sqrt{2D_o\Delta t} = \sqrt{2\nu\Delta t/Sc}$, where D_o is the *nominal* molecular diffusivity (i.e., diffusivity that the markers would have if their motion was purely Brownian). The properties of the fluid, i.e., the Schmidt number of the fluid, are thus taken into account. Equation (20) can now be written as follows:

$$\vec{X}_{t+1} = \vec{X}_t + \vec{U}_t^{(LBM)}\Delta t + \Delta \vec{X}_t^{(random)} \tag{22}$$

The fact that the LST simulates the transfer of a passive scalar allows for multiple Schmidt number simulations using a single LBM velocity field.

As the markers propagate through space, a check is made that they do not penetrate a solid wall at every time step, before the movement is accepted. The way that this is done is as follows: the marker's position is obtained within a unit cube that consists of the nearest-neighbor cubic lattice nodes; the unit cube is divided into 8 sub-cubes and if the marker attempts to enter a sub-cube that belongs to a solid node, the movement is rejected and the marker is returned to its original position (this is done in order to stay with the bounce-back boundary condition in LBM, i.e. the no-slip boundary condition). The procedure is illustrated in Figure 20.

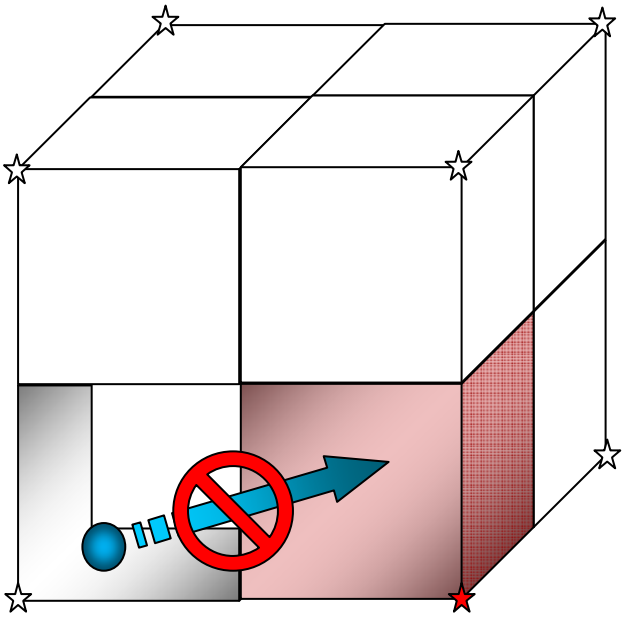

Figure 20 LST wall penetration check: marker's position (represented by a blue sphere) is obtained within a unit cube that consists of the 8 nearest-neighbor cubic lattice nodes (represented by stars); the unit cube is divided into 8 sub-cubes and if the marker attempts to enter a sub-cube that belongs to a solid node (in this case the red sub-cube that belongs to a red star), the movement (represented by a blue arrow) is rejected and the marker is returned to its original position (this is done in order to stay with the bounce-back boundary condition in LBM, i.e. the no-slip boundary condition).

Markers can be released in different ways, depending on the preference of the user. One type of release is the instantaneous *point* release, where all of the markers are released instantaneously out from the same point in space. Another type of release is the instantaneous *plane* release, where all of the markers are released from the same 2D

plane (for example from the plane of the flow domain entrance). A third type of release is *uniform* release. In this type of release the markers are seeded uniformly throughout the simulation domain. Finally, there is a *surface* release, where all of the markers are released from fluid nodes that have at least one nearest neighboring solid node. This release type can also be combined with the *plane* release, resulting in a *surface* release in user specified *plane*. For all of the release types a requirement is made that the initial coordinate of the marker must be in the space occupied by the fluid, not the solid. Figure 21 illustrates some of the available release modes.

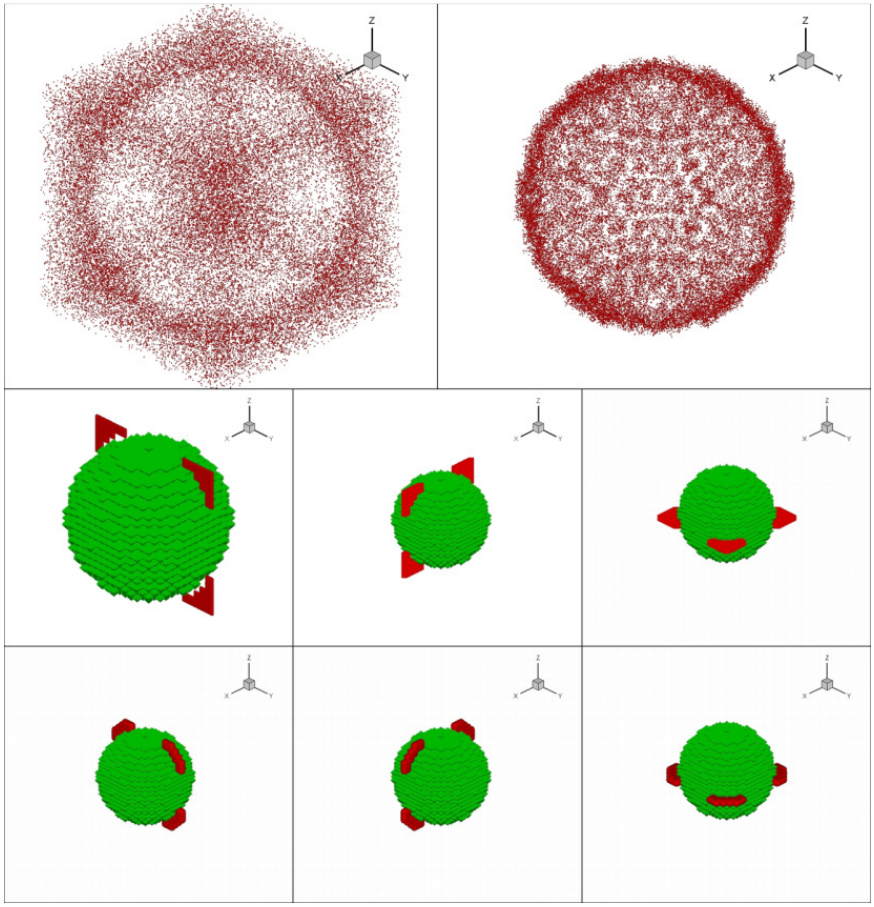

Figure 21 Selected release modes in LST: Top Left – uniform release around a sphere (sphere not shown for clarity); Top Right – uniform surface release around a sphere (sphere not shown for clarity); Second Row – uniform X,Y, and Z plane release around a sphere from left to right, respectively (sphere is shown in green); Third Row - uniform X,Y, and Z surface/plane release around a sphere from left to right, respectively (sphere is shown in green).

IV.2-c Velocity Interpolation

Since the velocity of the LST markers is obtained from the velocity field produced by the LBM simulation, several schemes are available for its interpolation. The most basic scheme is to use trilinear interpolation to interpolate the velocity values from the 8 nearest cubic lattice neighbors. The trilinear interpolation method is 1^{st} order accurate and is illustrated for a unit cube in Appendix - V .

Alternatively, a tricubic interpolation scheme can be implemented in order to achieve greater accuracy. The tricubic interpolation can be achieved by a sequence of one-dimensional cubic interpolations. However, because of the MPI sectioning of the computational domain, this is not convenient. Instead, a scheme by Lekien and Marsden is used (their C++ version was translated to Fortran as a part of this work) that relies on a specific 64×64 matrix that gives the relationship between the derivatives at the corners of the unit cube elements and the coefficients of the tricubic interpolant for this element.(Lekien and Marsden, 2005) Since the LBM velocity field remains static throughout the LST simulation, the required derivatives at the cubic lattice nodes obtained from LBM can be computed before the beginning of the LST simulation (setting the derivative values to zero at the walls). Storing the derivative values increases the memory footprint of the simulation, but simplifies the code and allows to avoid unnecessary MPI communication that would otherwise be required if the interpolation problem was broken up into a sequence of one-dimensional cubic interpolants.

Note, that care must be taken near the wall, since the tricubic interpolation scheme used in this work poses a requirement that the derivatives of the velocity must be continues. This assumption breaks down at the wall, since there they are artificially set to

zero. Thus it is expected that performance of this interpolation method will degrade as the distance to the wall is decreased. Moreover, since both the tricubic and trilinear methods use values at the 8 nearest corners of the cubic lattice to perform the interpolation, they cannot account for the fact that the solid-fluid boundary effectively lays halfway between the nodes due to the bounce-back boundary condition in LBM.

In order to account for the off-lattice solid-fluid boundary, each unit cube is broken up into 8 sub-cubes (each belonging to a corner of the unit cube). This is illustrated in Figure 22. Non-wall corners of the sub-cube to which the LST marker belongs are obtained using regular trilinear interpolation within the unit cube. The wall corners of the sub-cube are set to zero, since they represent the fluid-solid boundary and the no-slip boundary condition applies. Once all 8 corners of the sub-cube are known, the trilinear interpolation is performed on the sub-cube that contains the marker in order to obtain the interpolated velocity of the LST marker. This whole procedure is dubbed as "subtrilinear" from here on.

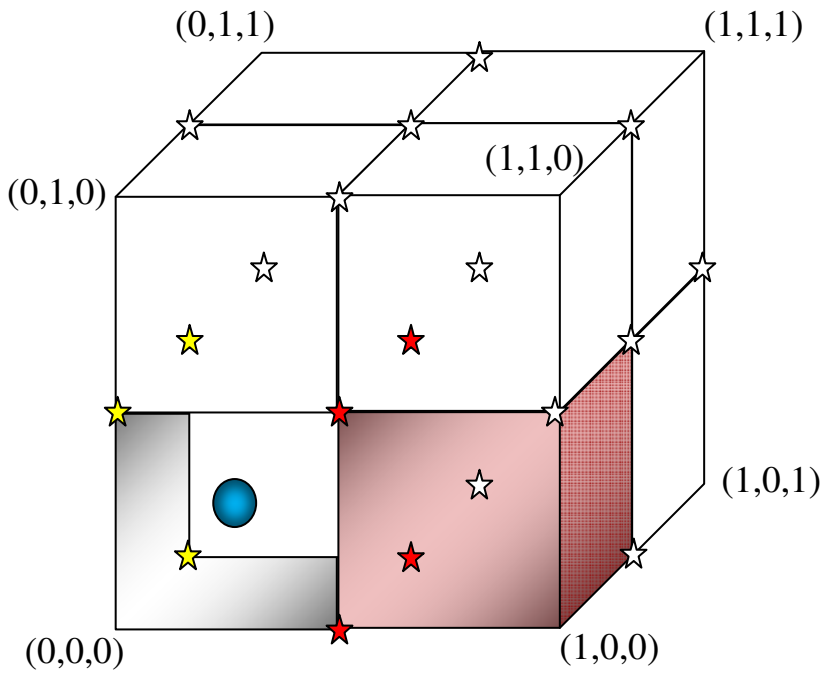

Figure 22 Illustration of the subtrilinear interpolation method near a solid wall. A unit cube is broken up into 8 sub-cubes. Red shows the volume occupied by solid due to the bounce-back boundary condition in LBM, if the (1,0,0) is a solid node and the rest are fluid. If an LST marker (shown by the blue sphere) happens to be inside a sub-cube shaded in gray that belongs to fluid node (0,0,0), its velocity is interpolated as follows. Half-way points labeled with yellow stars are obtained using regular trilinear interpolation within the unit cube. The half-way points labeled with red stars are set to zero, since they represent the fluid-solid boundary and the no-slip boundary condition applies. Once all 8 corners of the sub-cube are known, the trilinear interpolation is performed on the gray sub-cube in order to obtain the interpolated velocity of the LST marker.

Thus, there are four possible options for velocity interpolation in the LST simulation: trilinear everywhere, tricubic everywhere, trilinear in the bulk and subtrilinear at the wall, or tricubic in the bulk and subtrilinear at the wall. Figure 23 serves as a comparison between the four velocity interpolation schemes. It is a plot of average absolute error in interpolated velocity relative to the analytical solution for Poiseuille flow in a small channel. A small simulation domain was chosen, because it is more representative of what happens in a tight pore.

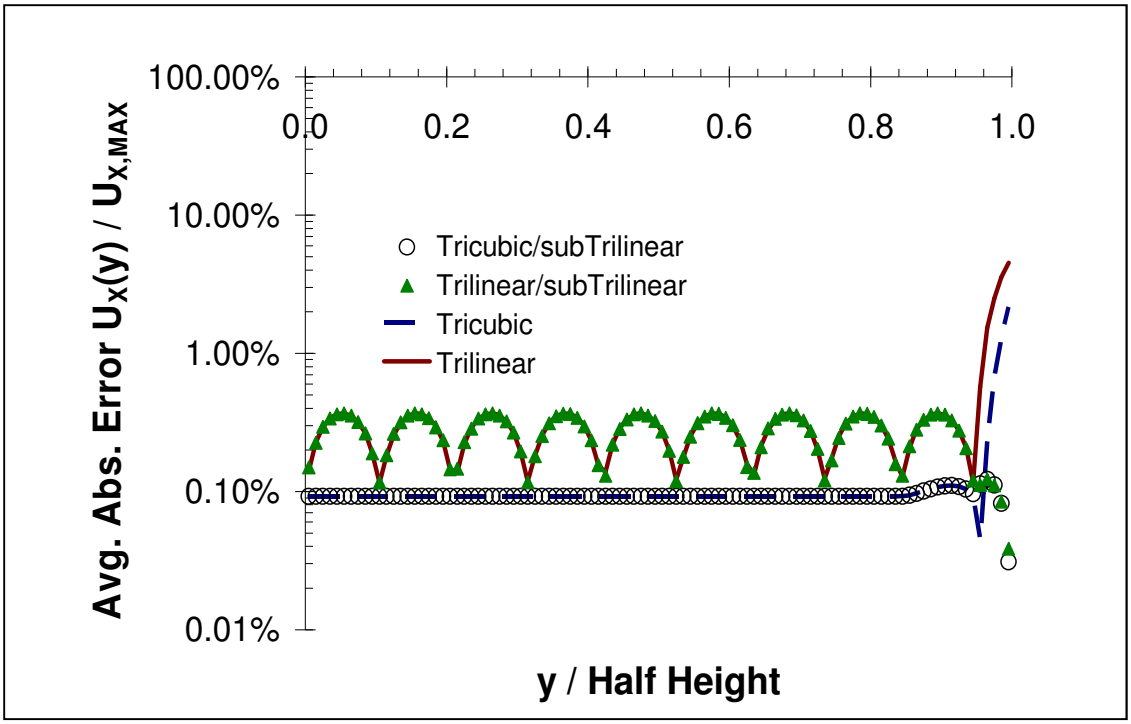

Figure 23 Average absolute error (expressed as a percentage of $U_{X,MAX}$) versus reduced distance from center in the vertical direction for uniform release of 5000 LST markers in Poiseuille flow in a 19cm channel as a function various interpolation schemes. Simulation domain size is 21x21x21; $\Delta P/L = 1x10^{-6}$ g/cm^2s^2. . The theoretical maximum streamwise velocity at the center of the channel is 0.0045 cm/s.

As is expected, near the center all four schemes perform fairly well (with tricubic schemes outperforming the trilinear schemes). Near, the wall both schemes begin to worsen due to the bounce-back boundary condition in LBM and also due to the fact that the trilinear interpolation is undermined by discontinuity in derivatives of velocity at the wall. Also, as is expected, the subtrilinear interpolation method offers considerable improvement (almost three order of magnitude difference) in accuracy near the wall.

In order to investigate further how the interpolation methods compare in geometries with more curvature and higher lattice resolution, a similar comparison of performance of velocity interpolation schemes for Poiseuille flow in pipe is presented in Figure 24.

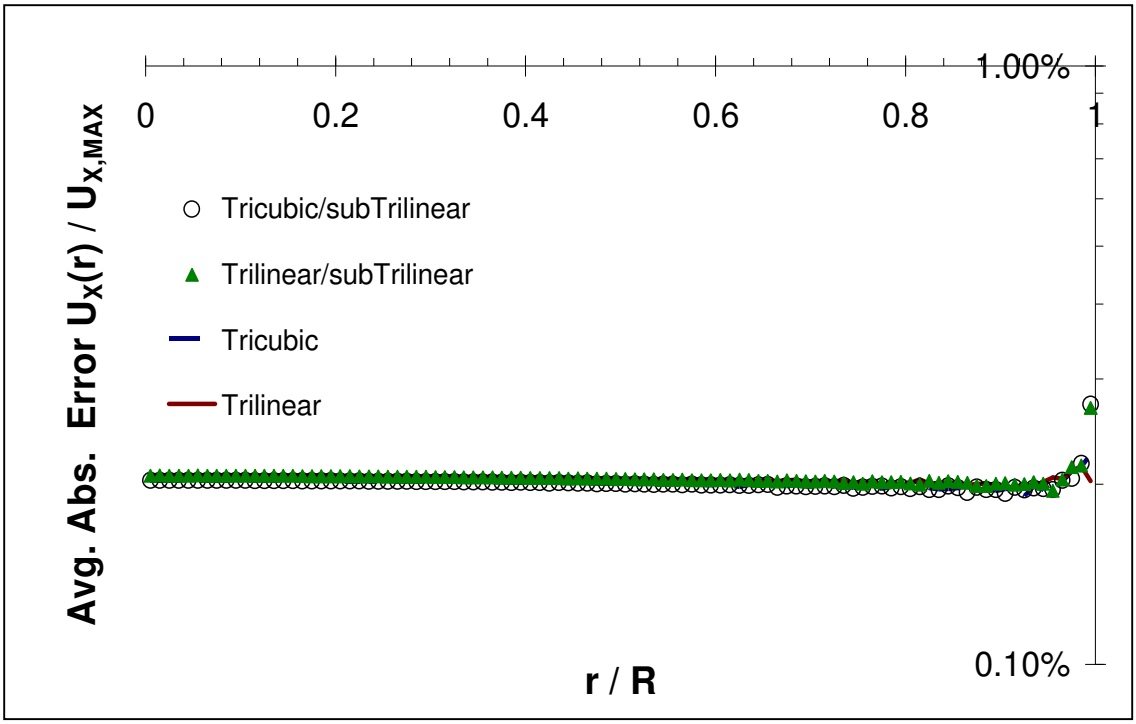

Figure 24 Average absolute error (expressed as a percentage of $U_{X,MAX}$) versus reduced distance from center in the radial direction for uniform release of 200,000 LST markers in Poiseuille flow in a 19cm diameter pipe as a function various interpolation schemes (solid lines are error relative to analytical solution; dotted lines are error relative to LBM velocity profile). Simulation domain size is 5 x 201 x 201; $\Delta P/L = 1x10^{-6}$ g/cm^{2}s^2. The theoretical maximum streamwise velocity at the center of the pipe is 0.0023 cm/s.

Even though from Figure 24 it seems as though at high lattice resolution of the flow geometry the accuracy of the different velocity interpolation schemes does not vary significantly, at the small resolution, such as in the case of a small channel (which is more representative of small pores in scaffolds), the Tricubic-subTrilinear is more accurate. Therefore, it is concluded that combination of the tricubic in the bulk and subtrilinear at the wall interpolation schemes is the optimal choice that offers the most accurate interpolation of velocity everywhere. Unfortunately, it comes at the cost of a large memory footprint which is not acceptable for large simulation domains.

IV.2-d Reaction Algorithm

LST has been used in conjunction with chemical reactions in the past. The effects of a first-order chemical reaction on turbulent mass transfer from a wall (Mitrovic and Papavassiliou, 2004) and to the wall (Nguyen and Papavassiliou, 2008) have been investigated using LST. Flow effects on the kinetics of an isothermal, equimolar, second-order reaction taking place in a channel have been also investigated using LST. The reactants were released instantaneously from the two opposite walls of the channel into fully developed turbulent or laminar flow.(Nguyen and Papavassiliou, 2008) Here we describe a novel approach to heterogeneous reaction modeling using LST, which allows the simulation of a range of first order reaction rates using just one set of markers. The simulation methodology is described below.

The idea is that a single LST marker can be used in order to represent a whole range of *solute particles* with different reaction probabilities. Since different *solute particles* may have a different likelihood of being consumed upon contact with a wall, we define a variable, q, which corresponds to the probability of a *solute particle* to react upon collision with the wall. Essentially, every LST marker represents a whole spectrum of *solute particles* whose reaction probabilities initially range between $q = 0$ (non-reactive) and $q = 1$ (100% reactive). Upon a marker's collision with the wall a random number p is generated from a uniform distribution between 0 and 1 (i.e., $0 < p \leq 1.0$), representing the chance of reaction to occur. If a *solute particle* represented by the LST marker has a 100% chance to react upon a collision with a wall ($q = 1.0$ corresponding to an instantaneous reaction), then the *solute particle* will be consumed at all times regardless of the outcome of p (i.e., $0 < p \leq 1.0$); however, if a *solute particle* has a only

40% chance to react ($q = 0.4$), then p must be $0 < p \leq 0.4$ in order for the *solute particle* to be consumed, and so on.

Note, however, that if a *solute particle* with a particular q is consumed (e.g., $q = 0.4$), a *solute particle* with a higher q (e.g., $q = 0.5$) would have also been consumed, had it been in place of the $q = 0.4$ *solute particle*. In fact, all *solute particles* with a higher value of q than $q = 0.4$ in our example, (i.e., $1.0 \geq q \geq 0.4$), would have been consumed, because they have a higher probability to react with the wall and be consumed. Thus, if a $q = 0.4$ *solute particle* reacts upon a wall collision, in our example, it is advantageous to also record that $1.0 \geq q > 0.4$ type of *solute particles* were consumed. Finally, if a *solute particle* has a 0% chance to react ($q = 0$), then p must be $p = 0$, which is rendered impossible in the code. In this case, the marker is returned to its position prior to the collision with the wall and will have a chance to change its position in the next time step. In this way, the whole spectrum of *solute particle* reaction probability values ($0 \leq q \leq 1$) can be modeled, using just a single LST marker.

In order to draw a connection with an experimentally measured quantity, the reaction probability q can be related to the *nominal* reaction rate constant k_0 (that is the reaction rate constant that the *solute particles* would have if they were in constant contact with the wall) in the following way. Assuming that all *solute particles* are in constant contact with the wall, after one time step only ($1 - q$) of the *solute particles* would not react. For example, if $q = 3/4$ then only 25% of the *solute particles* are expected not to react with the wall after one time step. The reaction with the wall is a heterogeneous reaction that can be described with *effective* first order kinetics. The fraction of the *solute*

particles that have not reacted can be related to k_0 using 1st order of reaction kinetics, as is shown below:

$$\frac{[C]}{[C_0]} = 1 - q = \exp(-k_o \Delta t) \tag{23}$$

where $[C]$ is the concentration of the reactant, $[C_0]$ is the reactant concentration at time zero, and Δt is the LST time step size. Equation (23) can be solved for the nominal reaction rate constant k_o to yield

$$k_o = \frac{1}{\Delta t} \ln\left(\frac{1}{1-q}\right) \tag{24}$$

Since the *solute particles* take time to reach the wall as they travel through the flow field, an interesting aspect to examine is the *effective* 1st order reaction rate kinetics obtained from the simulation that takes into account the effects of flow field on the movement of the *solute particles*. For example, the effective reaction rate constant would take into account the total time that it takes for the *solute particles* to react starting from their initial release time. Likewise, the effective half-life would represent the total period of time after the initial release for unreacted *solute particles* to decrease by half. The following formulas can be used to calculate the *effective* reaction rate coefficient, k_{eff}, and the effective half life, $t_{1/2}$, of the *solute particles*:

$$-\frac{d[C]}{dt} = k_{eff}[C] \tag{25}$$

$$t_{1/2} = \frac{\ln(2)}{k_{eff}} \tag{26}$$

Other quantities that can be extracted from a reactive LST simulation include the average survival distance (how far *solute particles* will travel on average before they react), which can provide information about the required length of the porous medium

when a conversion rate is desired.(Tomadakis and Rupani, 2007) Figure 25 is a typical result that can be obtained using the reactive LST algorithm: a grey scale 3D reconstruction of the scaffold inlet (Left) and outlet (right) as obtained from μCT, overlaid with local *solute particle* reaction probabilities, *q,* that on average collided with the scaffold's surface. In this figure the LST markers are released in a plane oriented perpendicular to flow (left panel of Figure 25). As the markers transverse into the scaffold, the solutes with a high reactivity (blue) become consumed and only the markers with the low reactivity (red) make it all the way through the scaffold and exit it from the other side.

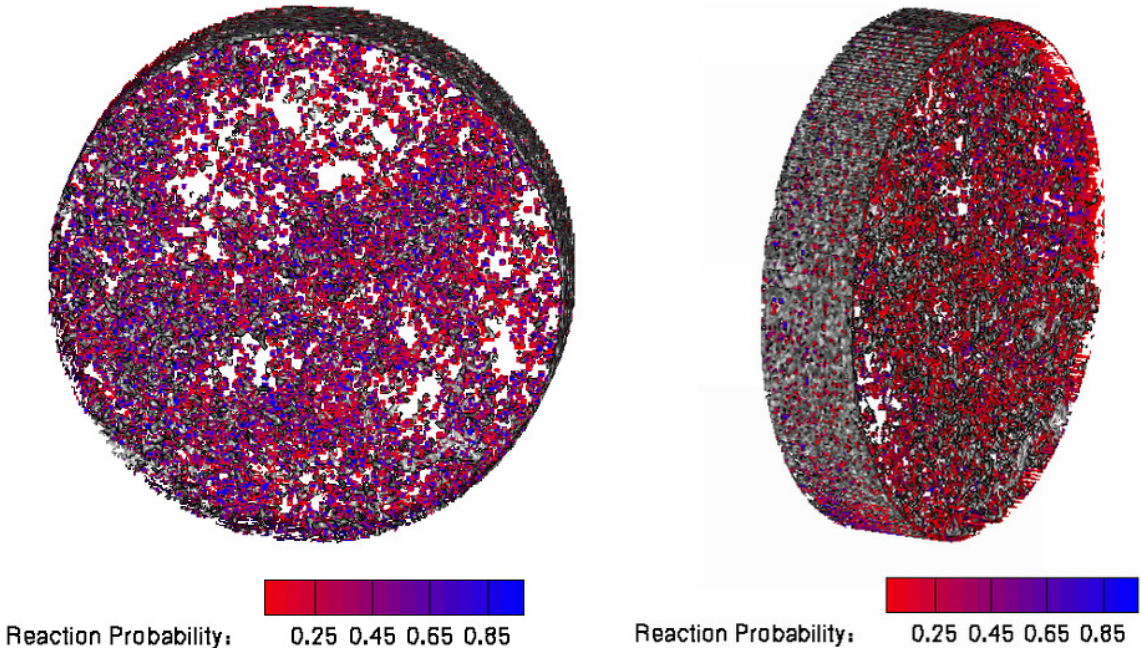

Figure 25 Grey scale 3D reconstruction of the scaffold *inlet* (Left) and *outlet* (right) as obtained from μCT, overlaid with local *solute particle* reaction probabilities *q* that on average collided with the scaffold's surface, where *q* can be related to the *nominal* reaction rate via Equation (24). Conditions are for scaffold in a flow perfusion bioreactor at the typical culturing flow rate of 1 mL/min and Sc = 1. Image from (Voronov et al., 2010).

IV.2-e Parallelization

The message passing interface (MPI) is used in order to parallelize the LST code. Pieces of the simulation geometry are distributed in approximately equal portions among MPI processes, not unlike the LBM parallelization scheme illustrated in Figure 10. While each MPI process contains a list of all LST marker positions, it only updates the positions of the markers that belong to its portion of the geometry as a new time step advances. After the time step is completed, all of the processes update the marker positions in their respective lists, such that every process contains an identical list of all of the most up-to-date marker positions.

IV.2-f Validation

In order to validate the LST code, a velocity field was obtained from a LBM simulation of pressure driven flow in an infinitely long channel (simulation domain size of 21 x 21 x 21 nodes with periodic boundary conditions applied in the streamwise *x* direction) at Reynolds number, $\mathrm{Re} = \frac{(2b)U}{\nu} = 5.72$ (where '2b' is the height of the channel and U is the bulk fluid velocity). Several simulations were performed in order to explore the effect of marker number on the accuracy of the LST method. The marker number ranged from 1,000-100,000, and the LST markers had a Schmidt number of 1. The markers were released instantly and uniformly throughout the channel domain and the simulation was allowed to evolve for 30,000 time steps. Reaction effects were not incorporated in these simulations, in order to validate the algorithm for the movement of markers only.

Because of the bounce back boundary condition used in LBM, the solid-fluid interface is effectively located halfway between the neighboring solid and fluid nodes.

This means that even though the channel ranges from 1 to 21 nodes in the *y* direction, the actual bottom of the channel is effectively located at 1.5 cm and the top is at 20.5 cm (assuming that one lattice unit represents 1 cm). Therefore the channel width '2b' is equal to 19 cm, and the center is at 11 cm. Figure 26 is a plot of the average *y* position with time, as a function of the number of markers.

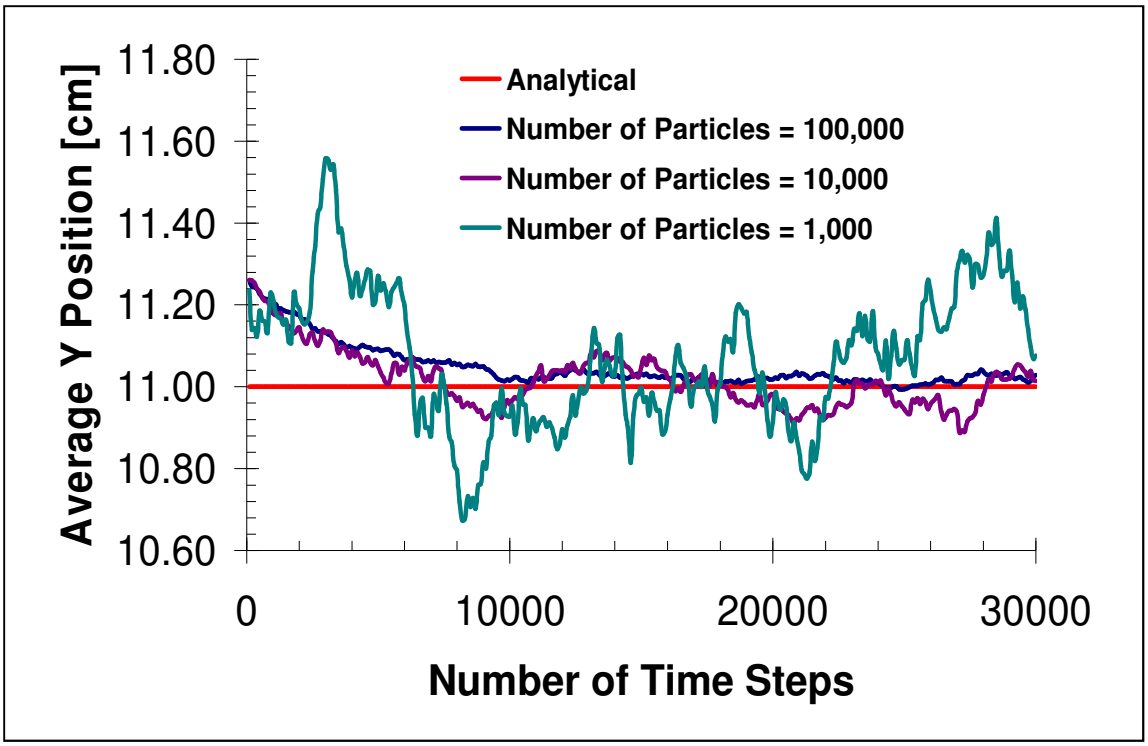

Figure 26 Comparison of the average *Y* position to the theoretically expected value of 11cm for pressure driven flow in a channel (domain size of 21 x 21 x 21 nodes) at Re=5.72, as a function of particle number. The particle number ranges from 1,000-100,000, and the LST particles have a Schmidt number of 1. The markers are spread uniformly throughout the channel domain and the simulation is allowed to evolve for 30,000 time steps.

It is apparent that the average *y* position fluctuates about the center of the channel and the fluctuations are dampened out as the number of markers increases. Since the average *y* position is a fluctuating quantity, we quantify the accuracy of the LST method in Figure 27 as a root mean square (RMS) of the error from the expected value of 11cm.

From Figure 27 it is apparent that as the number of markers increases, the RMS of the error goes down until about 50,000 markers (after which there seems to be no effect).

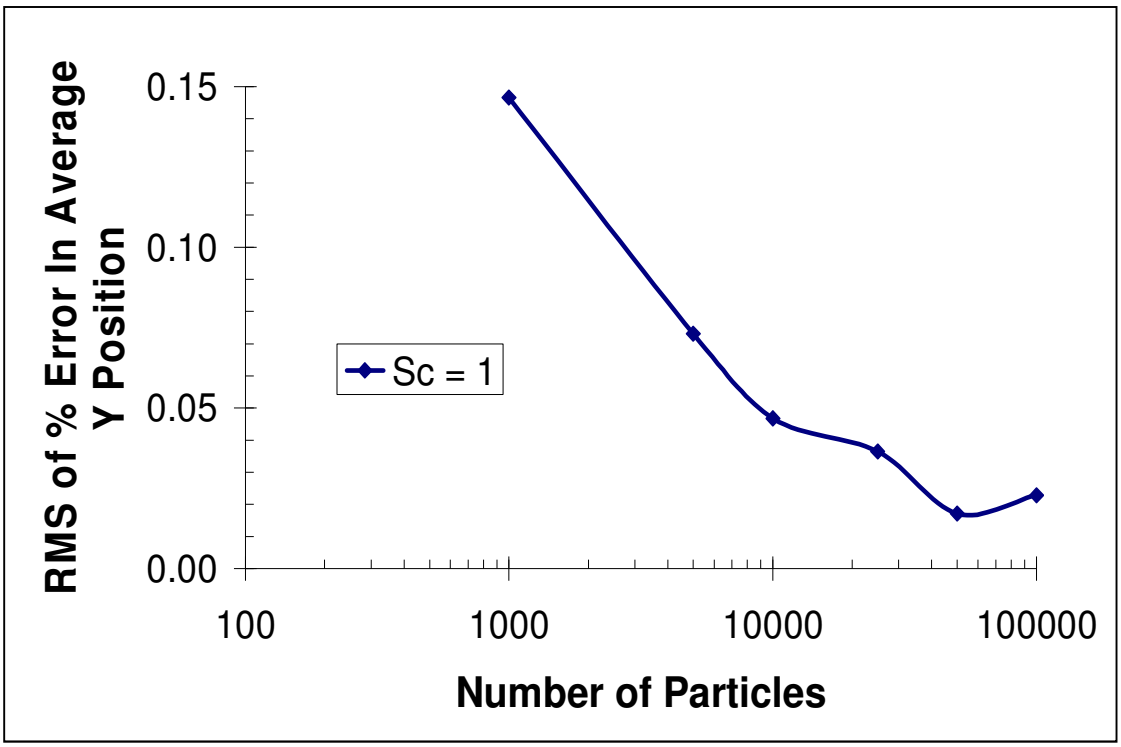

Figure 27 Accuracy of the average Y position relative to the expected value of 11cm quantified via RMS of %error for pressure driven flow in a channel (domain size of 21 x 21 x 21 nodes) at Re=5.72, as a function of particle number. The particle number ranges from 1,000-100,000, and the LST markers have a Schmidt number of 1. The markers are spread uniformly throughout the channel domain and the simulation is allowed to evolve for 30,000 time steps.

The second validation is a comparison of the variance in the *y* direction of the LST marker location relative to the theoretically predicted value. Since in laminar Poiseuille flow in a channel there is no velocity component in the *y* direction, the movement of the LST markers in the *y* direction should be purely Brownian. It is also limited, however, by the walls of the channel. Therefore, the *y* position of the markers should follow a uniform distribution, the bounds of which correspond to the top and bottom walls of the channel. The theoretically expected variance for a uniform

distribution with a range of ΔY is ΔY^2 / 12, and for our case the value of the variance is 30.0833 cm^2. Figure 28 is a plot of the variance of *y* positions with time, as a function of the number of markers.

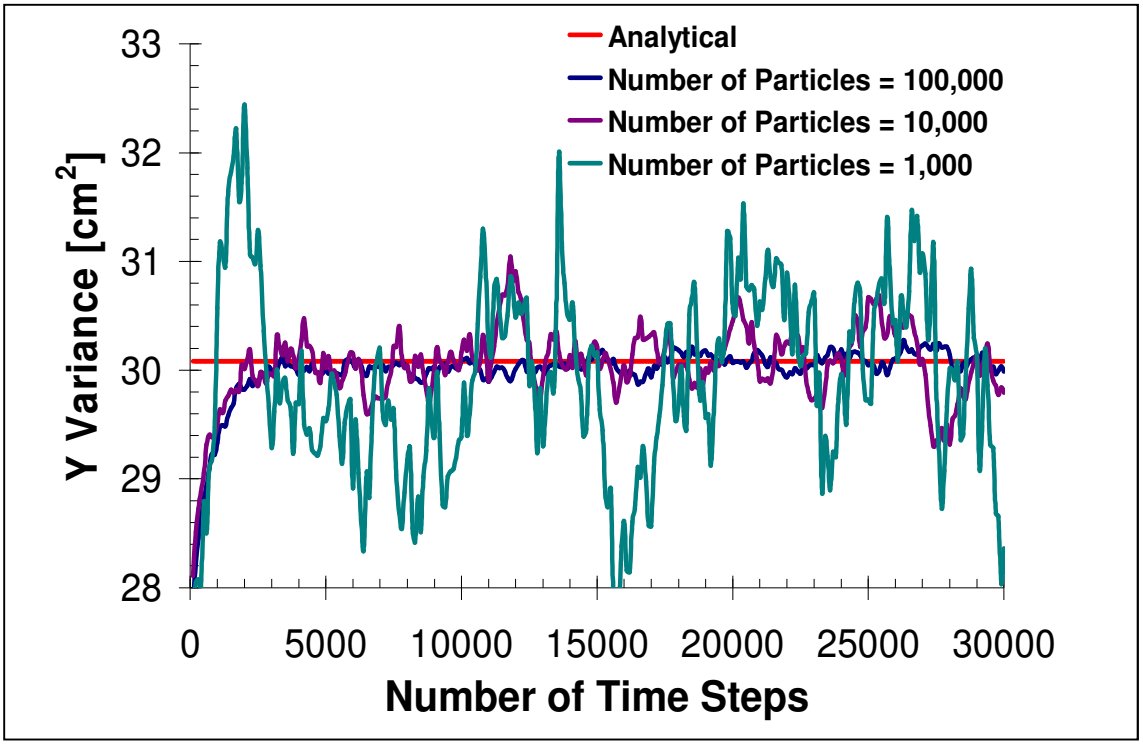

Figure 28 Comparison of the variance of Y positions to the theoretically expected value of 30.0833cm^2 for pressure driven flow in a channel (domain size of 21 x 21 x 21 nodes) at Re=5.72, as a function of particle number. The particle number ranges from 1,000-100,000, and the LST markers have a Schmidt number of 1. The markers are spread uniformly throughout the channel domain and the simulation is allowed to evolve for 30,000 time steps.

It is apparent that the variance of *y* positions fluctuates about the value expected from theory and the fluctuations are dampened out as the number of markers goes up. The root mean square (RMS) of the difference from the theoretically expected value of the variance is presented in Figure 29. It is apparent that as the number of markers increases, the RMS of the error decreases. Both of these validations seem to suggest that the LST is a half-order accurate method: that is when the number of markers is increased by an order of magnitude the error is halved.

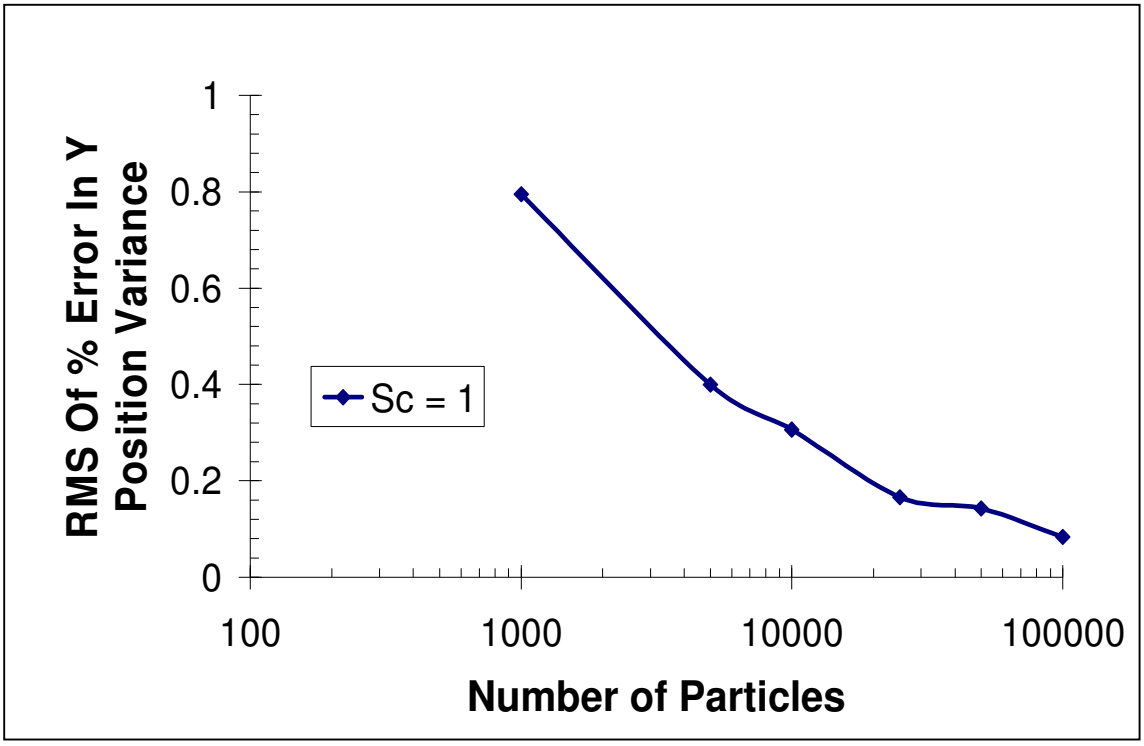

Figure 29 Accuracy of the variance of Y positions relative to the expected value of 30.0833cm2 quantified via RMS of %error for pressure driven flow in a channel (domain size of 21 x 21 x 21 nodes) at Re=5.72, as a function of particle number. The particle number ranges from 1,000-100,000, and the LST markers have a Schmidt number of 1. The markers are spread uniformly throughout the channel domain and the simulation is allowed to evolve for 30,000 time steps.

For the last validation of non-reactive LST the *effective* diffusivity in the streamwise direction is compared to the theoretically predicted value (i.e., the diffusivity that takes into account the convective contribution of the flow field and is calculated relative to the mean position of the markers). Molecular diffusivity (commonly referred to as the diffusion coefficient) is the rate at which transfer of solute in a given fluid occurs under the driving force of a concentration gradient. It is defined as the slope of the mean square displacement (MSD) of the solute molecules traveling in a solvent in the long time limit [see Equation (21)]. In the short time limit the MSD increased quadratically with time, because the distance traveled is proportional to the time interval

(distance equals velocity times time). However, the quadratic behavior holds only for a short period of time (of the order of the mean collision time). Beyond this time the motion is better described as a random walk, for which the MSD increases linearly with time. Therefore, in order to avoid the equilibration period that displays the quadratic behavior of the MSD, the results are only collected for the last half of the simulation. The MSD is fitted using a linear least squares approach and the diffusivity is obtained from the slope of the obtained linear equation.

For Poiseuille flow in a channel, the Taylor-Aris dispersion coefficient is given by Equation (27) [or in the dimensionless form by Equation (28)] (Sukop, Thorne et al., 2006):

$$D_{eff} = D_o + \frac{(2b)^2 \overline{U}^2}{210 D_o} \tag{27}$$

or

$$D_{eff} \Big/ D_o = 1 + \frac{Pe^2}{210} \qquad \text{for } \sqrt{210} << Pe << L/a \tag{28}$$

where $Pe = \mathrm{Re}\, Sc$ is the Peclet number, and L is the length of the channel. A total of 100,000 LST markers were released uniformly and instantaneously throughout the simulation domain and their trajectories were allowed to evolve for a total of 1,000,000 time steps. The Peclet number was varied between 28 and 171 in order to produce a comparison of the Taylor-Aris dispersion coefficient to the analytical solution over a range of Schmidt numbers. The LST simulation results are compared to the analytical solution for Taylor-Aris dispersion coefficient for Poiseuille flow in a channel in Figure 30. As can be seen from Figure 30, the LST model accurately reproduces the analytical solution.

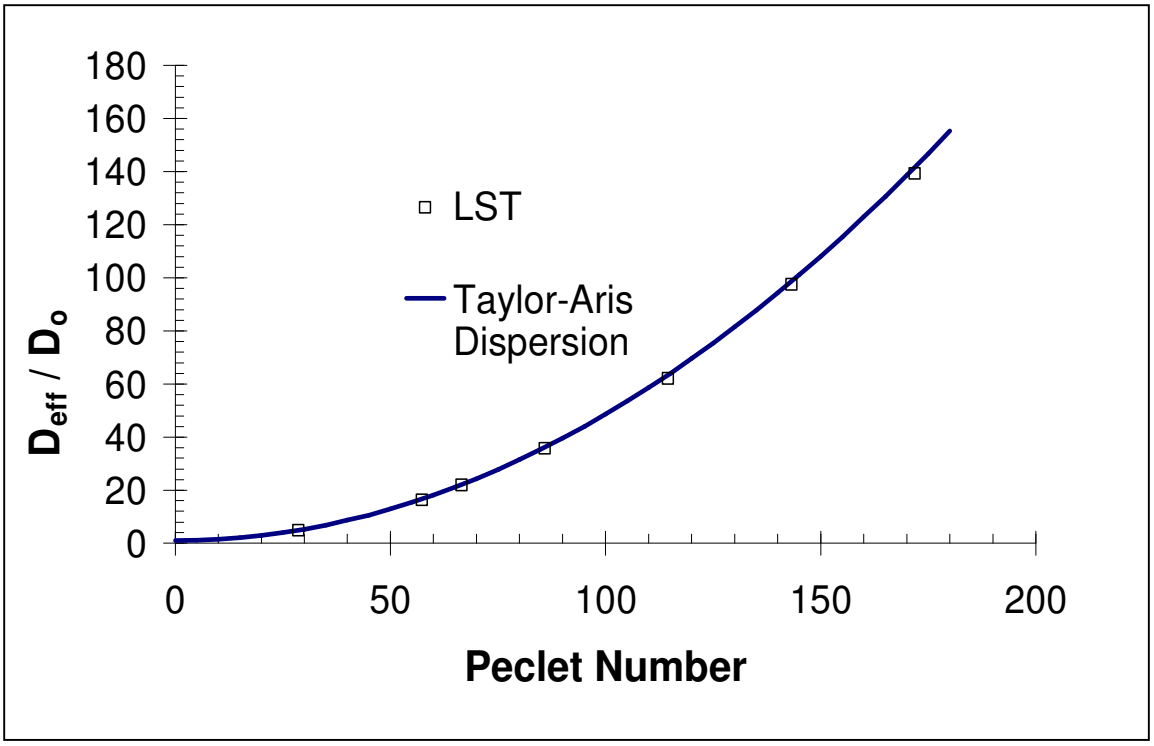

Figure 30 Comparison of the dimensionless effective diffusivity in the streamwise direction obtained from LST to the theoretically predicted value for Poiseuille flow in a channel obtained from the Taylor-Aris dispersion formula [see Equation (28)]. A total of 100,000 LST markers were released uniformly throughout the simulation domain and their trajectories were allowed to evolve for a total of 1,000,000 time steps. The Peclet number was varied between 28 and 171 in order to produce a comparison of the Taylor-Aris dispersion coefficient to the analytical solution over a wide range of Schmidt numbers. Simulation domain size was 21 x 21 x 21; channel height was 19cm and $\Delta P / L = 1 \times 10^{-6}$ g / cm^{2}s^2, corresponding to Re = 5.73.

For Poiseuille flow in a pipe, the Taylor-Aris dispersion coefficient is given by Equation (29) [or in a dimensionless form by Equation (30)] (Sukop, Thorne et al., 2006):

$$D_{eff} = D_o + \frac{(2R)^2 \overline{U}^2}{192 D_o} \tag{29}$$

or

$$D_{eff} / D_o = 1 + \frac{Pe^2}{192} \qquad \text{for } \sqrt{192} << Pe << L/a \tag{30}$$

where $Pe = \mathrm{Re}\, Sc$ is the Peclet number, and L is the length of the pipe.

A total of 100,000 LST markers were released uniformly and instantaneously throughout the simulation domain and their trajectories were allowed to evolve for a total

of 1,000,000 time steps. The Peclet number was varied between 10 and 64 in order to produce a comparison of the Taylor-Aris dispersion coefficient to the analytical solution over a range of Schmidt numbers. The LST simulation results are compared to the analytical solution for Taylor-Aris dispersion coefficient for Poiseuille flow in a channel in Figure 31. As can be seen from Figure 31, the LST model accurately reproduces the analytical solution. In order to test how the simulation results depend on particle number, the pipe simulation is repeated for 10,000 particles and the results are also reported in Figure 31. Although the accuracy decreased a little bit, the percent error from the analytical solution was still within 1 - 2%. However, decreasing the number of time steps down to 100,000 produced considerably poorer results.

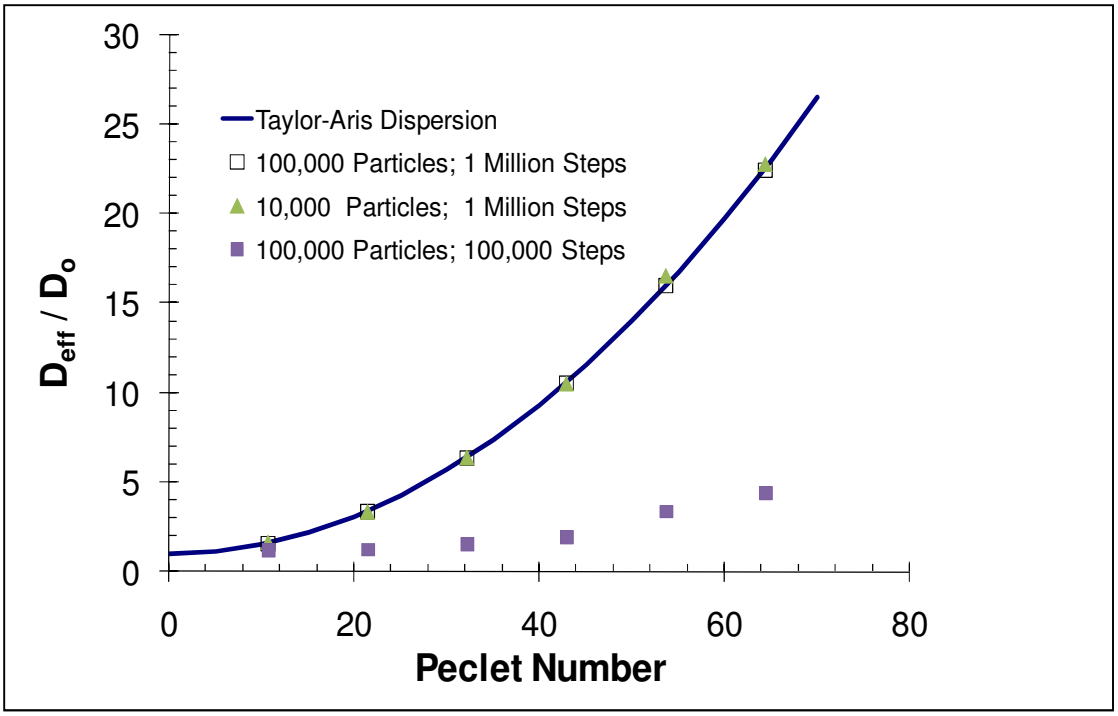

Figure 31 Comparison of the dimensionless effective diffusivity in the streamwise direction obtained from LST to the theoretically predicted values for Poiseuille flow in a pipe obtained from Taylor-Aris dispersion formula. A total of 100,000 LST markers were released uniformly throughout the simulation domain and their trajectories were allowed to evolve for a total of 1,000,000 time steps. Additionally, the number of particles and the number of time steps were each separately reduced by an order of magnitude in order to see the sensitive of the results to these parameters. The Peclet number was varied between 10 and 859 in order to produce a comparison of the Taylor-Aris dispersion coefficient to the analytical solution over a wide range of Schmidt numbers (data for high Pe number shows similar trends in accuracy, but is omitted

for clarity). Simulation domain size was 5 x 101 x 101; pipe diameter was 19cm and $\Delta P / L = 1 \times 10^{-6}$ g / $cm^2 s^2$, corresponding to Re = 2.15.

Since Equation (28) is only valid for non-reactive particles, it cannot be used directly to validate the reactive LST results. However, it can be used qualitatively, since it predicts that the dimensionless effective diffusivity varies linearly with Peclet number squared. In order to validate the reactive part of the LST algorithm, Figure 32 is a plot of the dimensionless effective diffusivity versus Peclet number squared for a range of nominal reaction rate constants for Poiseuille flow in a channel. At all levels of reactivity the LST model displays the expected linear trend. Thus it is concluded that the reactive LST algorithm is valid.

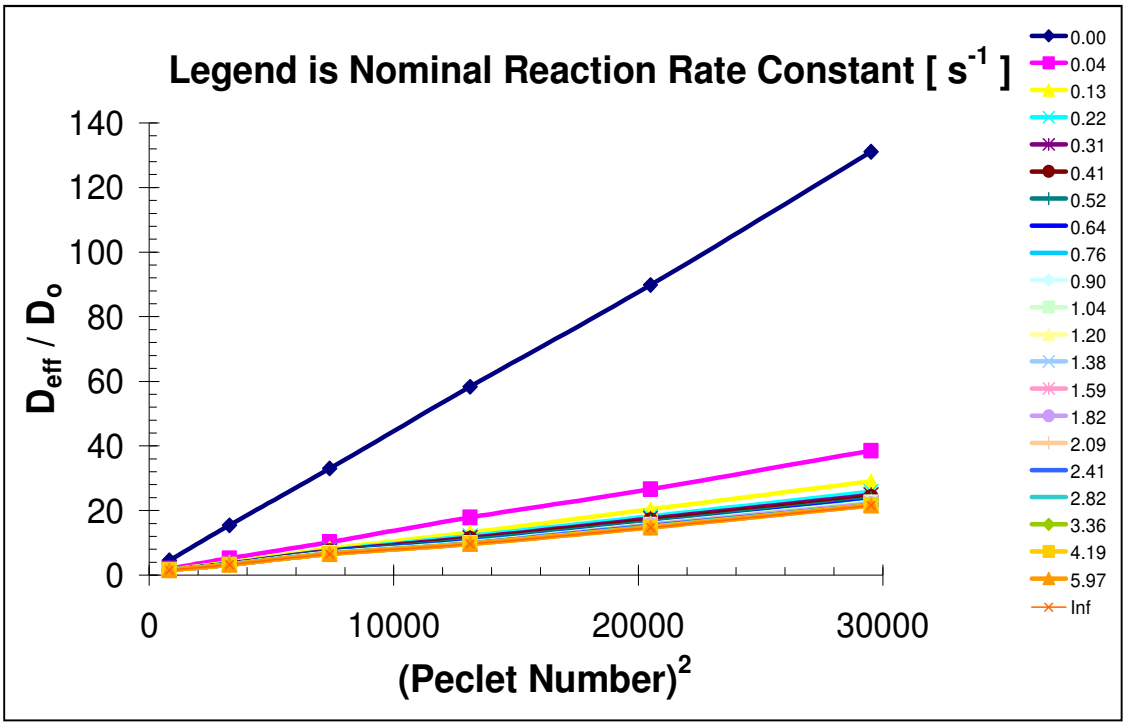

Figure 32 Dimensionless effective diffusivity in the streamwise direction versus Peclet number squared as a function of different nominal reaction rates. A linear trend is expected from Taylor-Aris dispersion formula [Equation (28)]. A total of 100,000 LST markers were released uniformly throughout the simulation domain and their trajectories were allowed to evolve for a total of 1,000,000 time steps. The LST markers were modeled with 20 reactivity levels in order to explore a wide range of reaction rates. Simulation domain size was 21 x 21 x 21; channel height was 19cm and $\Delta P / L = 1 \times 10^{-6}$ g / $cm^2 s^2$, corresponding to Re = 5.73.

IV.2-g Simulation Details

The LST simulations were performed using 100,000 LST markers (this number was found to be sufficient to reproduce analytical results during the validation runs). The velocity field obtained from LBM was used in order to calculate the convective velocity component of the LST markers. Unless stated otherwise, their initial positions were uniformly distributed within the scaffold pore space available to the fluid and the velocity was interpolated using the trilinear-subtrilinear interpolation scheme (in order to minimize the memory footprint of the simulation). Upon contact with the scaffold wall, each LST marker represented a whole spectrum of *solute particles* whose reaction probabilities initially ranged between q = 0 (non-reactive) and q = 1 (100% reactive), in order to simulate the probability of a range of nutrients and/or oxygen to be consumed by the cells on the surface of the scaffold. It was also assumed that the scaffold surface was uniformly covered with cells, and that each cell could always consume nutrients at equal rates. Since second order reactions (reactions between *solute particles*) were not taken into account for this model, any interactions between LST markers were neglected (i.e. they did not affect each other's path). This approximation is good for a dilute solution. The simulation was allowed to evolve for a total of 1,000,000 time steps. The 'Mersenne Twister' random number generator with a cycle of length (2^{19937} - 1) was used to obtain random numbers from a uniform distribution in the LST code.(Matsumoto and Nishimura, 1998) Random numbers from the standard normal distribution were obtained using the Central Limit Theorem based on the random numbers from the uniform distribution (see Appendix - IV).

All LST markers that were released in the flow field were initially assigned the value of $q_{init} = 1$ (i.e. each LST marker represented *solute particles* from the whole reaction probability spectrum of $0 \leq q \leq 1$). Every time a LST marker would collide with the scaffold wall, a random number $0 < p \leq 1$ was generated from a uniform distribution in order to represent the chance of a reaction to occur. If p were larger than q_{init}, then there was no change made to the reaction probability, q, of the LST marker because the reaction did not occur for any of the *solute particles* that it represents. If p were smaller than q_{init} than the reaction probability q of the LST marker would be updated to $q_{new} = p$ (see Section IV.2-d). Essentially, it would be recorded that all the *solute particles,* represented by the LST marker, with a reaction probability q in the range $q_{new} \leq q \leq q_{init}$ (more reactive than the generated random number *p)* have reacted. Only the *solute particles* with reaction probability q in the range $0 < q \leq q_{new}$ (less reactive than the generated random number *p)* would be represented by the LST marker from then on, until the next reaction occurs. At every step, the minimum reaction probability (i.e. q_{new}) and maximum reaction probability (i.e. q_{init}, or q_{old} if the LST marker has reacted before) were recorded for the LST markers that participated in a wall collision-reaction at that particular time step. The average minimum and the average maximum q *(*obtained by averaging the q values of those LST markers that collided with the walls and reacted at each time step) provides a reaction probability range of *solute particles* that are on average reacting at a particular time (or at some distance into the scaffold).

V. RESULTS AND DISCUSSION

V.1 FLUID SHEAR STRESS RESULTS

Assuming that a target amount of stimulatory shear stress can be known (the physiologic fluid shear stress through the lacunar-canalicular system has been suggested to be 8 to 30 dynes/cm, although in *in-vitro* 3D flow perfusion experiments lower shear stress values have been identified as stimulatory) (Weinbaum, Cowin et al., 1994; Bancroft, Sikavitsas et al., 2002), the questions that arise are: (a) what flow conditions should be used in order to achieve the desired stress value within the scaffold, and (b) how should the scaffold be manufactured in order to maximize the distribution of the desired amount of stress to the majority of the cells (while minimizing the exposure of the seeded cells to undesired or extreme stress values). What follows is an attempt to answer these two questions, while also providing additional physical insights in order to better characterize typical PLLA scaffolds.

V.1-a Foam Scaffolds

In order to answer the first question, LBM simulations of flow through 36 different foam scaffolds that were manufactured with different porosity target values and with different NaCl grain size combinations (see Section II.2-a) were conducted. Table 6 is a summary of scaffold permeabilities obtained from the LBM simulations as a function of porosity and the average pore size.

Table 6 Scaffold permeability as a function of porosity and NaCl grain size [cm^2].

NaCl grain size (μm)	Porosity = 80%	Porosity = 85%	Porosity = 90%	Porosity = 95%
180 – 250	2.37×10^{-5}	3.95×10^{-5}	6.50×10^{-5}	1.24×10^{-4}
250 – 355	2.93×10^{-5}	3.57×10^{-5}	6.10×10^{-5}	1.42×10^{-4}
355 – 450	5.53×10^{-5}	8.60×10^{-5}	9.18×10^{-5}	1.92×10^{-4}

For each one of these scaffolds, the stresses were calculated everywhere in the flow domain (see Figure 33 for 3D LBM local fluid stress results in a typical scaffold).

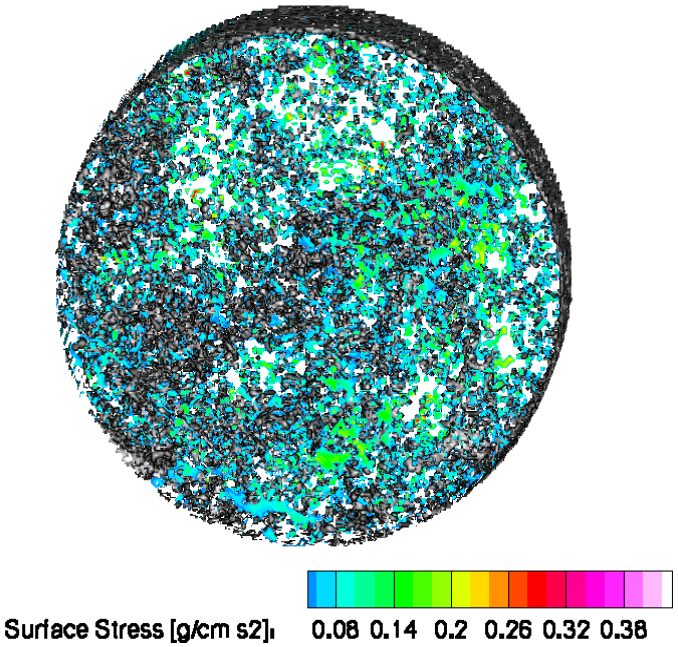

Figure 33 Grey scale 3D reconstruction of the scaffold geometry as obtained from µCT, overlaid with local fluid shear stress values (color) that would be experienced within the scaffold in a flow perfusion bioreactor at the typical culturing flow rate of 1 mL/min. Image from (Voronov, VanGordon et al., 2010).

Stress distribution histograms were generated for the bulk stresses and for the surface stresses. The stress distributions for all scaffolds exhibited a positive skewness, (i.e., the stress distributions had long tails to the right of the distribution). When the average stress and the average surface shear stresses for each stress distribution are plotted versus the superficial velocity for flows at four different pressure drops, a strong relationship is observed (see Figure 34). The equation that best describes the average bulk shear stress is

$$\bar{\tau}_{BULK} = (0.0851 \pm 0.0064)\left(\frac{\Delta P}{L}\right)^{0.503\pm0.015} U_s^{\,0.497\pm0.015} \qquad \text{with an } R^2=0.997 \tag{31}$$

and the correlation that best describes the average surface shear stress is

$$\bar{\tau}_{SURFACE} = (0.096 \pm 0.003)\left(\frac{\Delta P}{L}\right)^{0.5} U_s^{0.5} \qquad \text{with an } R^2=0.969 \tag{32}$$

All three parameters (the constant and the exponents on the right hand side) were fitted in Equation (31) and are reported with 99% confidence intervals, while only the constant was fit in Equation (32). Note that the square root dependency on the pressure drop and the superficial velocity is expected from theory, if Darcy's law or the BK equation is solved for the average stress (see Appendix - I and Appendix - II). These empirical correlations allow the estimation of the bulk stress and of the average shear stress on the internal surface of the scaffold that are experienced by the cells seeded in a scaffold as a function of two parameters that are easily measured – the pressure drop and the superficial velocity.

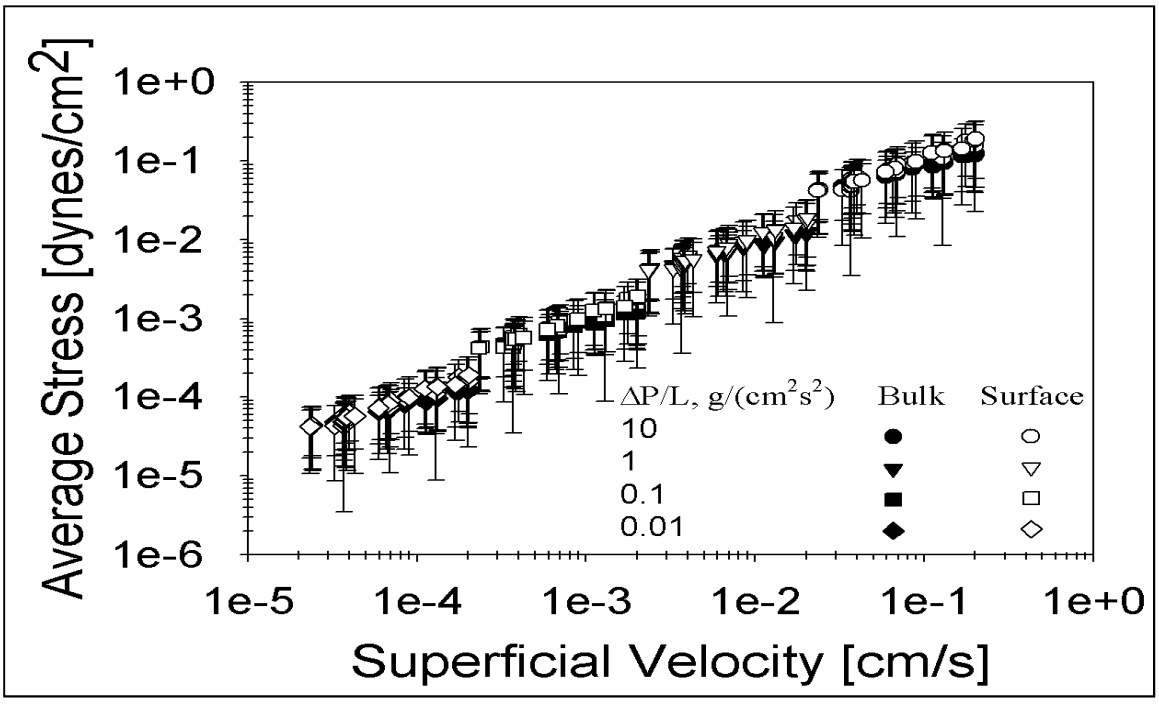

Figure 34 Average bulk (solid symbols) and surface (empty symbols) stresses as a function of superficial velocity and pressure drop for PLLA scaffolds with various manufacturing characteristics. The width of the error bars is equal to two standard deviations from the average. Image from (Voronov, VanGordon et al., 2010).

In order to answer the second question, the effects of scaffold manufacturing parameters on the stress distribution within the scaffold must be examined. Figure 35 is a table of μCT intensity images that represent the pore space in a scaffold as a function of the scaffold manufacturing parameters. Manufacturing the scaffold at high porosity results to more empty space (and less solid obstacles) available within the scaffold, while manufacturing the scaffold with increasing NaCl grain size seems to create larger pores (as well as larger obstacles). At the highest porosity (95%), however, the geometrical differences are imperceptible due to a lack of considerable solid material.

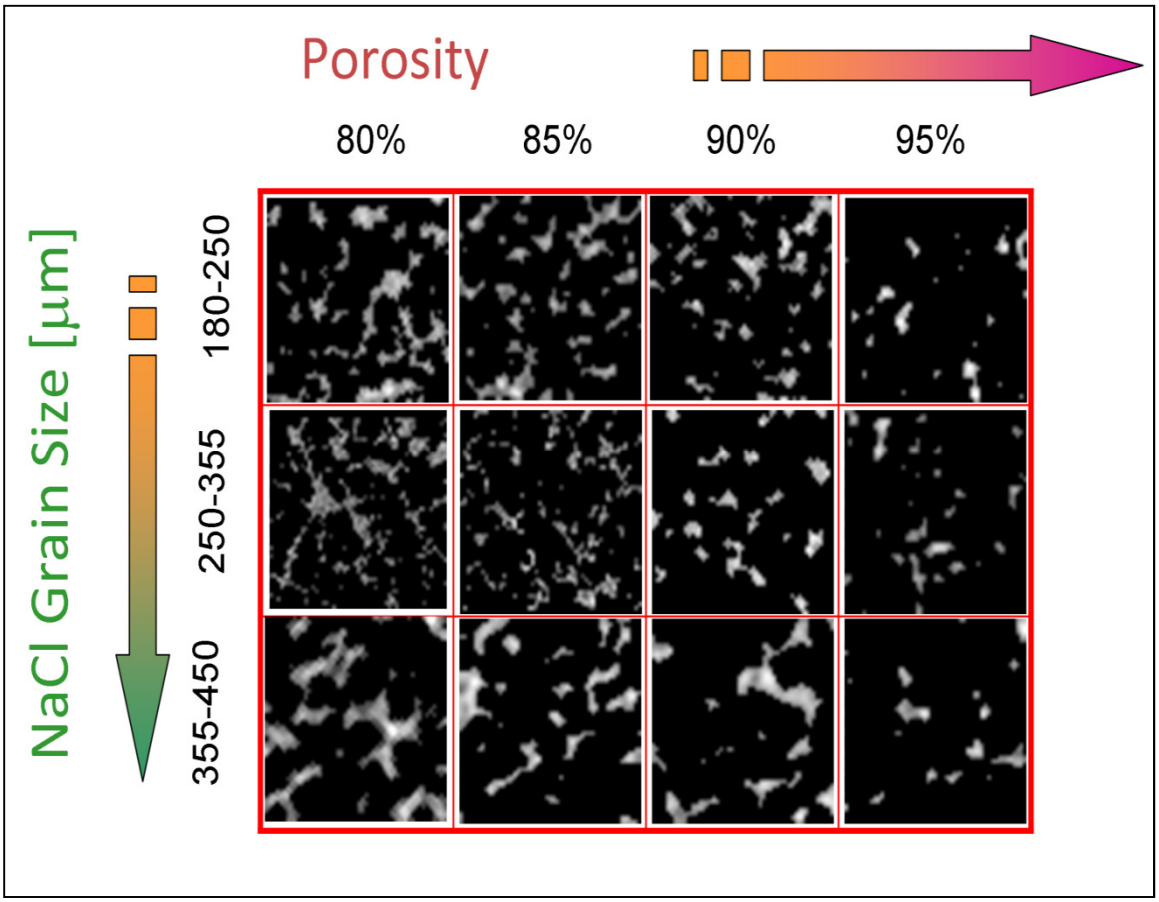

Figure 35 Comparison of intensity μCT images of PLLA scaffolds prepared by salt leeching using various manufacturing parameters. *Grayscale* intensity pixels represent radio-density of the scaffold material; *black* is empty space open to flow. Each image is a square with an edge equal to 2.142 mm cut out from the middle of a scaffold. Image from (Voronov, VanGordon et al., 2010).

Figure 36 is a table of histograms for the stress distributions that would be experienced by cells seeded on scaffolds. From Figure 36, it is apparent that the stress distributions do not vary significantly as the porosity and the NaCl grain size are changed. The distributions are characterized by long tails to the right, i.e., a positive skewness. What this seems to imply is that the standardized wall fluid shear stress distribution for flows through highly porous media follows a single probability density function (pdf) that appears to be universal.

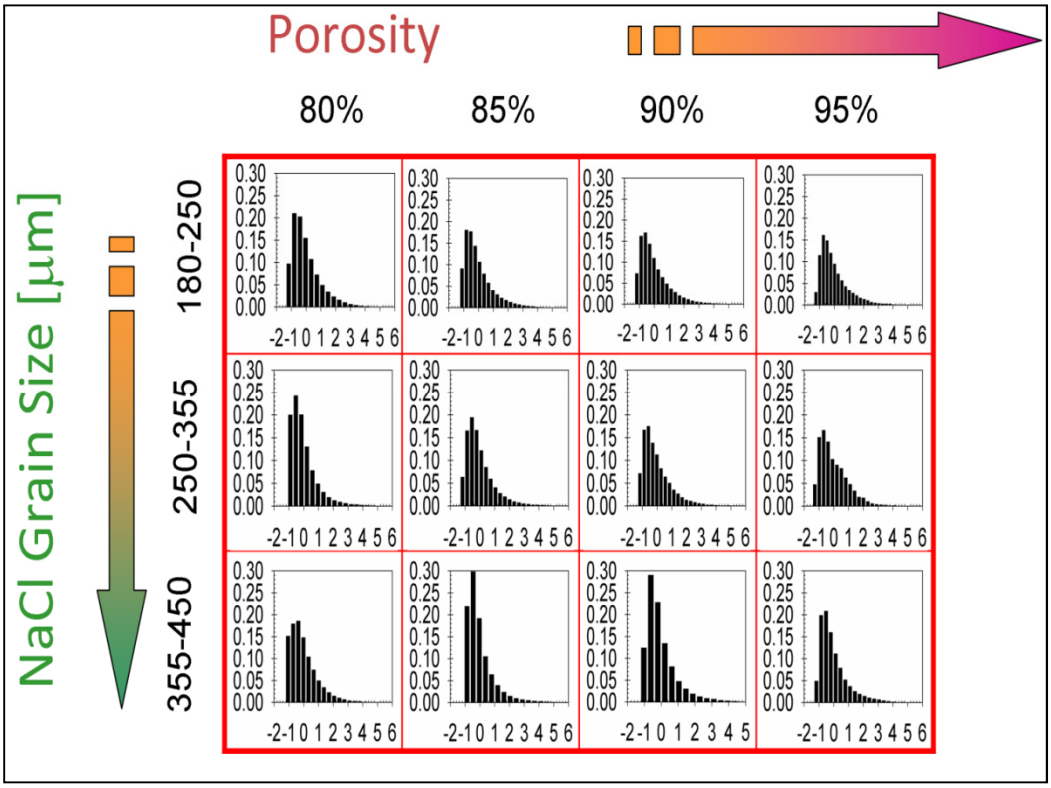

Figure 36 Comparison of surface stress histograms obtained from simulations for PLLA scaffolds that were prepared by salt leeching using various manufacturing parameters. Abscissa is frequency of occurrence ranging from 0 to 0.3, and ordinate is reduced surface stress, ranging from roughly -1 to 5. Stresses are normalized in the following manner: (surface stress – mean surface stress) / (standard deviation of the surface stress distribution). Image from (Voronov, VanGordon et al., 2010).

V.1-b Effect of Defects

Another implication of the linear relationship between the skewness and the kurtosis is that the standard deviation of the surface stress distributions does not change much when compared to the mean stress (see Table 7).

Table 7 Standard deviation of the surface stress distribution expressed as a percentage of the average stress.

NaCl Grain Size (μm)	porosity = 80%	porosity = 85%	porosity = 90%	porosity = 95%
180 - 250	73.19	78.66	79.74	69.70
250 - 355	85.88	73.38	74.83	74.79
355 - 450	71.73	78.36	80.73	68.97

Thus, the manufacturing parameters do not affect the percent of deviation from the average surface stress experienced by the cells seeded on the scaffold. What does affect the stress distributions, however, is manufacturing defects. In Figure 37, the stress is distributed uniformly in a scaffold prepared with no defect, whereas in the non-isotropic defective scaffold the fluid chooses the path of least resistance. At a constant pressure drop this results in a higher flow rate through the area with less solid material present, which in turn results in higher values of localized surface stresses near the defect site.

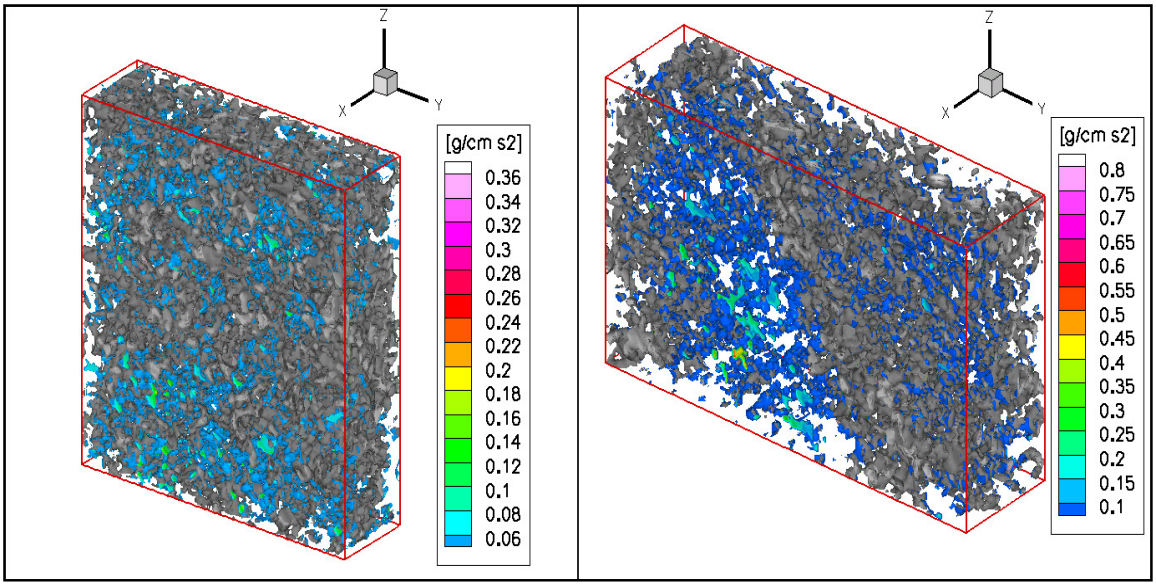

Figure 37 3D reconstructions of a PLLA scaffolds obtained from μCT and reconstructed using Matlab®. *Grayscale* intensity pixels represent radio-density of the scaffold material; *white* is empty space open to flow; *color* is the surface stress (with values below average omitted for clarity). LEFT PANEL: An isotropic scaffold displaying a uniform surface stress distribution throughout. RIGHT PANEL: A scaffold with a defect, showing higher surface stresses near the more porous region of the local defect. The simulation geometry shown here was cut out from the center of the scaffolds in order to avoid end effects, and the flow is in the positive *x* direction. Image from (Voronov, VanGordon et al., 2010).

In order to further characterize the physical properties of the scaffolds, their permeability and surface area-to-volume ratio have been calculated. Permeability is a measure of the ability of a material to transmit fluids and is a property of the porous medium only, not the fluid. It is defined through Darcy's law, which relates the superficial fluid velocity to the pressure gradient applied to a porous medium. Darcy's law is given as (Bear, 1988)

$$U_s = -\frac{k}{\mu}\left(\frac{\Delta P}{L}\right) \tag{33}$$

where k is the medium permeability. The permeability data for the PLLA scaffolds are presented in Table 9. As is expected, permeability increases with higher porosity and higher NaCl grain size. The permeability values for the PLLA scaffolds appearing in Table 9 are comparable to those of highly fractured rock and of well sorted sand or

gravel.(Bear, 1988) In comparison to bone tissue, the range of experimentally obtained permeability of human, bovine and porcine cancellous bone is from about 2×10^{-8} cm^2 to 2×10^{-4} cm^2 (with the higher permeability values corresponding to higher porosities, and vice versa).(Cowin, 2001; Kohles et al., 2001) In a LBM computational study, the permeability of 92.3% porous vertebral trabecular bone scanned with μCT was calculated to be 2.98×10^{-4} to 5.05×10^{-4} cm^2.(Zeiser et al., 2008)

V.1-c Non-woven Fiber Mesh Scaffolds

In order to compare the two scaffold types (nonwoven fiber mesh and porous foam) on geometrically equivalent basis, two scaffolds were prepared with roughly equivalent specific surface area and volume fraction parameters (see Table 4). The surface stress was calculated for both scaffolds using LBM and the results are summarized in .

Table 8 Surface stress calculation results obtained from LBM for 0.5mL/min flow rate.

	Nonwoven Fiber Mesh	Porous Foam
Mean Surface Stress [g / cm s^2]	0.12	0.13
Standard Deviation [g / cm s^2]	0.09	0.11
Standard Deviation as % of Mean	74.84	78.18

Figure 38 contains images of Matlab® 3D reconstructions of average surface shear stresses on the porous foam and nonwoven fiber mesh scaffolds.

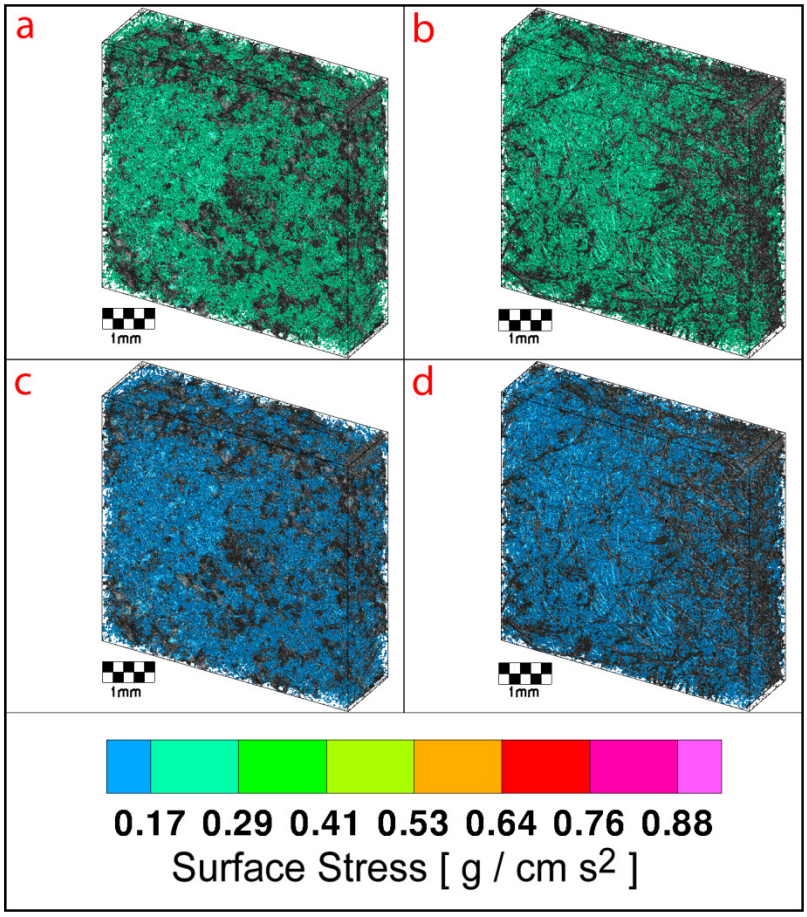

Figure 38 Matlab® 3D reconstructions from μCT imaging showing average surface shear stresses for a 1mL/min flow rate in a a)porous foam scaffold created by solvent casting/particulate leaching and a b)nonwoven fiber mesh scaffold created by spunbonding and 0.5mL/min flow rate in a c)porous foam scaffold created by solvent casting/particulate leaching and d)nonwoven fiber mesh scaffold created by spunbonding. Image from (VanGordon, Voronov et al., 2010).

Since it is apparent from that there is no appreciable difference between the mean surface stress values for the two scaffold geometries, the distribution of the surface stress was examined next. This is the distribution of shear stresses that cells would experience if they were attached to the scaffold surface in a single cell layer which is an ideal case during initial stages of culturing. Figure 39 shows the surface stress distributions for the porous foam and nonwoven fiber mesh scaffolds. From these figures it can be concluded

that the shape of the surface stress distributions for the two different scaffold geometries does not display a significant difference. Both of them are skewed to the right.

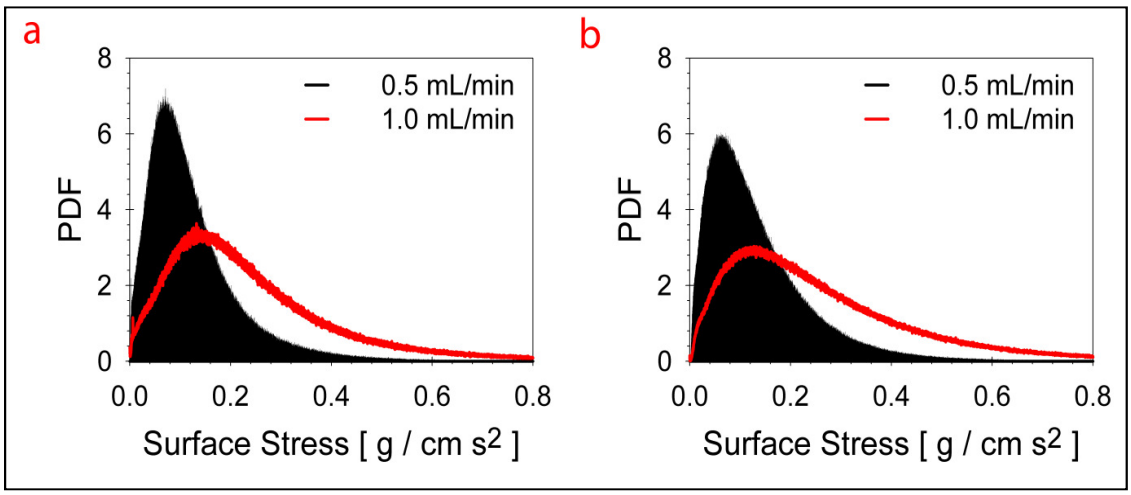

Figure 39 Surface stress distributions in a)porous foam scaffold produced using solvent casting/particulate leaching method and b)nonwoven fiber mesh scaffold made by spunbonding method obtained from calculations using LBM method for a flow rate of (shaded)0.5mL/min with (red line)1mL/min overlay. Image from (VanGordon, Voronov et al., 2010).

A multitude of analytical solutions for creeping flow through geometrically simple cylinder arrangements, as well as semi-empirical correlations for creeping flow through more geometrically complicated cylinder arrangements exist (Skartsis et al., 1992; Stylianopoulos et al., 2008; Nabovati et al., 2009). Table 9 contains a comparison of the permeability values obtained from LBM to the Blake-Kozeny-Carman (BKC) equation

$$k = \frac{\varepsilon^3}{(1-\varepsilon)^2}\frac{1}{S^2\kappa} \tag{34}$$

where ε is the medium void fraction, S is $4/D$ for cylinders if D is the diameter of cylinders, and κ is the Kozeny constant ($\kappa \approx 5$ from experiment). Since the BKC equation is well established, simple to use and versatile, it appears that it can be used for the estimation of the permeability of high-porosity scaffolds such as the ones used in this study. Detailed fluid dynamics simulations can provide the local shear stress field and the

shear stress distribution. The *S* used in BKC calculations is the same obtained from our algorithm used in 3D reconstructions of μCT data (see Section III.3) The permeability of the foam scaffold is about 45% higher than the permeability of the fiber mesh scaffold, which is a reflection of the higher specific area of the fiber mesh (see Table 4.)

Table 9 Comparison of scaffold permeability obtained from LBM to prediction from the BKC equation for porous foam scaffolds and nonwoven fiber mesh scaffolds.

	Nonwoven Fiber Mesh Permeability [cm^2]	% Difference from LBM	Porous Foam Permeability [cm^2]	% Difference from LBM
LBM [cm^2]	5.29×10^{-6}	-	7.70×10^{-6}	-
BKC Equation (Assuming k=5)	4.96×10^{-6}	6.32	7.86×10^{-6}	2.08

V.1-d General Fluid Stress Probability Density Function

In order to deduce what the non-idealized empirical shear stress distribution is for highly porous isotropic media that is common to bone tissue engineering the average shear stress, $\bar{\tau}_w$, and the standard deviation of the shear stress, σ_τ, were calculated and the standardized pdf was generated for each simulation of the 36 foam scaffolds, by transforming the shear stress into a reduced variable using Equation (35):

$$\tau^* = \frac{\left(\tau_w - \bar{\tau}_w\right)}{\sigma_\tau} \tag{35}$$

Note that unless otherwise mentioned from here on all pdfs will be presented in the standardized form, since a non-standardized pdf can be obtained from the standard pdf when the average and the standard deviation are known.

The Kolmogorov-Smirnov (KS) goodness of fit test was used to decide if a sample followed a hypothesized continuous distribution. Some 65 different pdf forms were tested for goodness of fit for each of the 36 scaffolds using the EasyFit version 5.2

software (http://www.mathwave.com/). The three-parameter gamma (Gamma-3P) pdf was chosen as the best pdf for describing the distribution of the normalized τ_w data for the 36 scaffolds, because it ranked at the top of the average and mode KS test rankings over the 36 samples and because it is well-characterized in statistics. The three-parameter gamma probability density function, usually designated as $\Gamma(\alpha,\gamma,\beta)$, is

$$f(\tau_W^*) = \frac{(\tau_W^* - \gamma)^{\alpha-1}}{\beta^{\alpha}\Gamma(\alpha)} \exp\left[-(\tau_W^* - \gamma)/\beta\right] \tag{36}$$

where $\Gamma(\alpha)$ is a complete gamma function, α is the shape parameter ($\alpha > 0$), β is the scale parameter ($\beta > 0$), and γ is the location parameter ($\gamma = 0$ yields the standard gamma distribution $\Gamma(\alpha,0,\beta)$, i.e., the two-parameter gamma pdf).

The KS statistic for a $\Gamma(\alpha,\gamma,\beta)$ pdf was on average 3.194, versus, for example, 7.361 for the lognormal pdf and 8.417 for a beta pdf. The $\Gamma(\alpha,\gamma,\beta)$ pdf also displayed an acceptable "diffusion" of fitting parameters from the mean values of 14.67% (the diffusion is the standard deviation as a percent of mean for each fitting parameter). The calculated parameters that statistically fit the distribution followed by τ_w^* within high porosity foam scaffolds were $\alpha = 2.91 \pm 0.63$, $\beta = 0.45 \pm 0.05$ and $\gamma = -1.43 \pm 0.17$.

It is quite interesting that a single pdf with the specific parameters given above can describe the standardized shear stress distribution inside all of the 36 porous foamy scaffolds. However, is this distribution characteristic only to the PLLA salt-leached scaffolds manufactured and simulated in our laboratory, or could it be describing the distributions obtained for scaffolds manufactured by different techniques and/or distributions obtained by other laboratories? Figure 40 is a comparison of the $\Gamma(2.91,-1.43,0.45)$ pdf suggested herein to the distributions obtained through

computations of experiments for various porous scaffolds in other laboratories, as well as non-woven fiber mesh PLLA scaffolds manufactured in our laboratory.

The suggested $\Gamma(\alpha,\gamma,\beta)$ pdf appears to be a good fit to the experimentally and computationally obtained distributions from various laboratories. The results of the KS hypothesis test formed with the null hypothesis as "The given normalized wall shear stress is a $\Gamma(2.91,-1.43,0.45)$ random variable" showed that the null hypothesis can be accepted at the 20% significance level for all distributions, indicating that there is no statistically significant difference between these distributions and the one suggested herein at the 0.02 level. Therefore, the $\Gamma(\alpha,\gamma,\beta)$ pdf suggested in this Letter can be a practical way to estimate the distribution of the wall shear stresses in various porous constructs without the need to do experiments or simulations. However, in order to convert τ_W^* into dimensional values of τ_w one must know the average stress and the standard deviation of the pdf of τ_w, as is evident from the transformation equation

$$\tau_w = \bar{\tau}_w + \tau_W^* \sigma_\tau \tag{37}$$

The following is an illustration of a simple method for obtaining the dimensional values of τ_w using the $\Gamma(\alpha,\gamma,\beta)$ pdf and the aid of rather well established theory. This should be viewed as a suggested methodology, but not as the only approach to this problem.

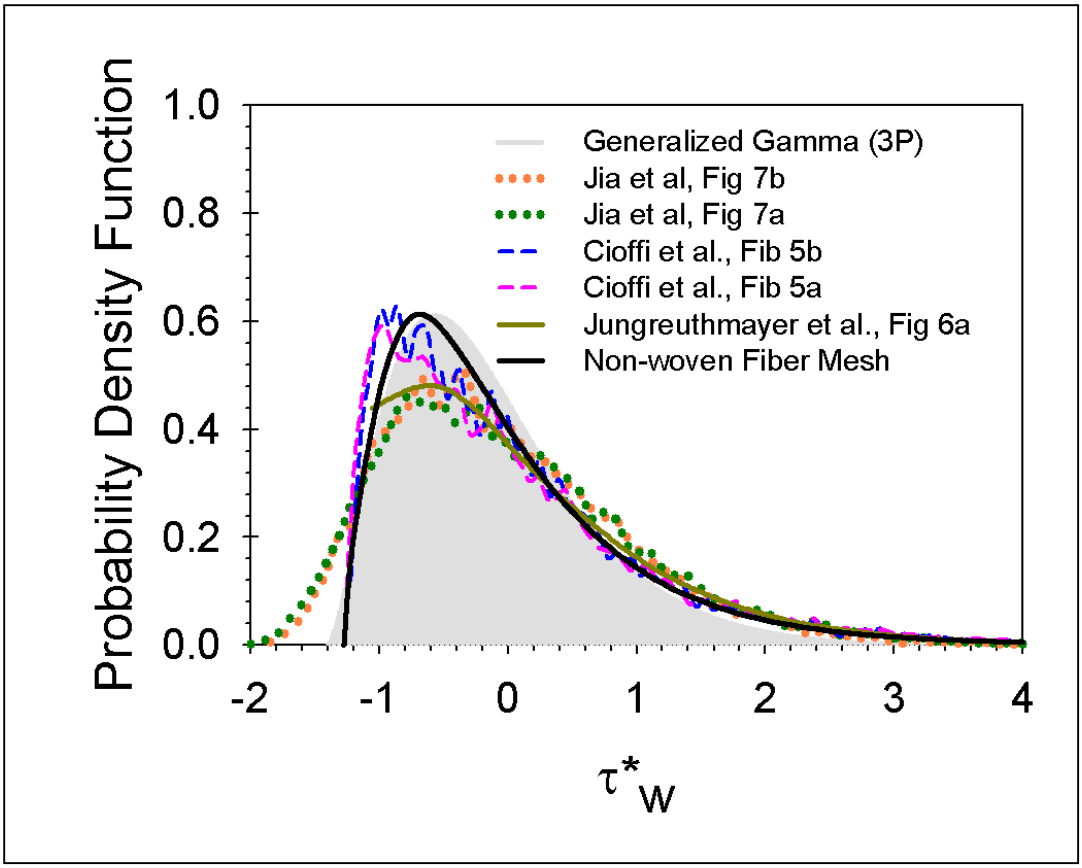

Figure 40 Comparison of the Γ(α,γ,β) pdf (α = 2.91, β = 0.45 and γ = -1.43; in Light Gray Filled) with experimentally and computationally obtained pdfs for τ_w^*: Figure 7 in (Jia, Bagnaninchi et al., 2009) using Doppler Optical Coherence Tomography for chitosan scaffolds prepared via freeze-drying, at 0.5mL/min (Orange Dotted – 90% porous, 100-200μm pore size; Dark Green Dotted – 85% porous, 30-100μm pore size); Figure 5 in (Cioffi, Kuffer et al., 2008) using Fluent finite volume code for PolyActive®/PEGT/PBT 80 % porous and 180μm average pore size scaffolds prepared via compression molding (Dark Blue Dashed – 0.03 mL/min; Light Pink Dashed – 0.3 mL/min, smoothed using Loess method); Figure 6a in (Jungreuthmayer, Donahue et al., 2009) using OpenFOAM: icoFoam finite volume code for collagen-glycosaminoglycan (96 μm average pore size, 90.5-99% porosity) scaffolds (Dark Yellow Monochrome); Unpublished data from our laboratory using LBM simulations for Poly-L-Lactic acid non-woven fiber mesh scaffold with 85% porosity and an average fiber diameter of 35μm (Black Monochrome). Data from other laboratories was extracted using DataTheif v1.5. Image from (Voronov et al., 2010).

First, the average τ_w needs to be calculated. Assuming that it is equal to the pressure drop multiplied by the hydraulic diameter of the porous medium, D_h, then: $\bar{\tau}_w = D_h\left(\frac{-\Delta P}{L}\right)$. Then, using Darcy's Law, $\frac{\Delta P}{L} = \frac{\mu}{k}U_S$, where k is the permeability of the medium, ΔP/L is the pressure drop across the medium, and U_S is the superficial fluid velocity, it is

$$\bar{\tau}_w = D_h\left(\frac{\mu}{k}U_S\right) \tag{38}$$

From here one can express the hydraulic diameter of the porous medium by making the assumption that the permeability is proportional to the wetted surface area of the porous medium with a proportionality constant *K*, as follows(Probstein, 1989)]:

$$k = K * D_h^2 \qquad \text{or} \qquad D_h = \sqrt{\frac{k}{K}} \tag{39}$$

Substituting this expression for the hydraulic diameter into Equation (38) yields

$$\bar{\tau}_w = \sqrt{\frac{k}{K}}\left(\frac{\mu}{k}U_S\right) = \mathrm{B}\left(\frac{\mu}{\sqrt{k}}U_S\right) \tag{40}$$

where $\mathrm{B} = \sqrt{\frac{1}{K}}$. This equation has been previously published for the average stress imposed by the interstitial flow through a periodic square array of cylinders by Wang & Tarbell(Wang and Tarbell, 1995) and around spheres by Brinkman (Brinkman, 1947), where $B = 4 / \pi$ for cylinders, and $B = 3 / \pi$ for spheres. Because $B \approx 1$, several researchers have been using the Wang & Tarbell (WT) equation assuming $B = 1$. (Wang and Tarbell, 2000; Boschetti, Raimondi et al., 2006; Cioffi, Boschetti et al., 2006; Chung et al., 2007; Jia, Bagnaninchi et al., 2009)

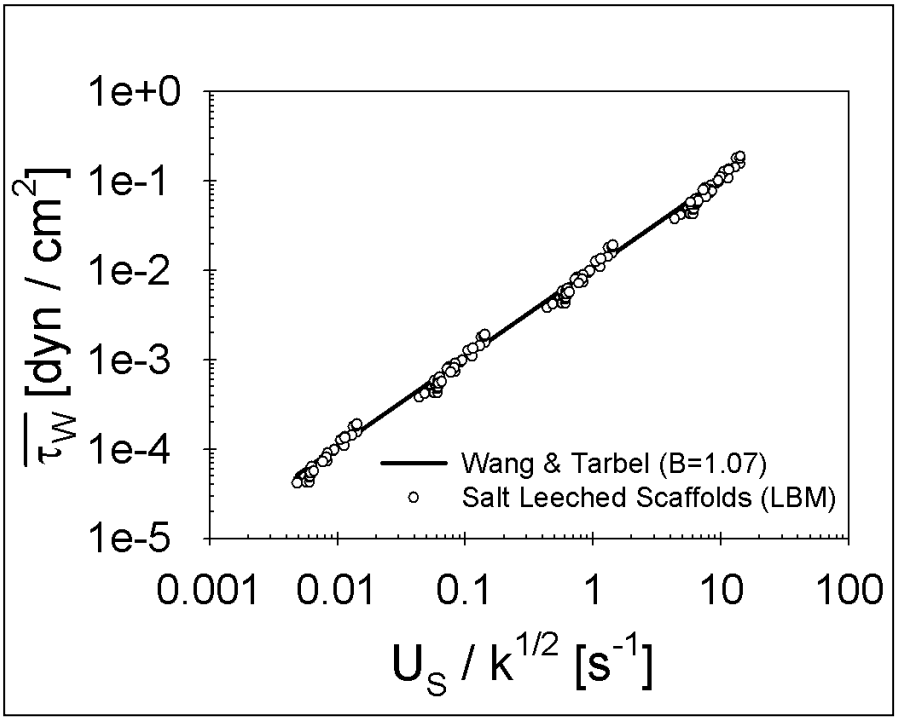

Figure 41 Average τ_w calculated with LBM simulations at ΔP/L = 0.001 to 1 dyn/cm for salt-leached scaffolds that range in porosity between 80% and 95%, and average pore size between 180 and 450 microns. Image from (Voronov, VanGordon et al., 2010).

In the case of porous media with a complex internal structure, like the ones used in our work, we cannot make an assumption about the value of *B*. Instead, we fit $\bar{\tau}_W$ as a function of $\frac{U_S}{\sqrt{k}}$ for data obtained from LBM simulations of pressure driven creeping flows through salt leached scaffolds of various architectures. The parameter, *B,* was found to be *B*=1.07±0.03 within 99% confidence intervals (R^2 = 0.97) (see Figure 41). This implies that the WT equation is more general than previously thought, since it works well for complex porous media, and that the $B \approx 1$ assumption is acceptable for geometries other than spheres and cylinders.

However, the problem remains as to how to estimate the Darcy permeability of the porous medium, which is needed for applying the WT equation. Although for simple

or idealized geometries there exist models that can predict the permeability fairly well, the semi-empirical Blake-Kozeny-Carman (BKC) equation shown below provides a fairly accurate estimate for highly porous geometries at low Reynolds number flows

$$k = \frac{\varepsilon^3}{(1-\varepsilon)^2}\frac{1}{S^2\kappa}, \tag{41}$$

where ε is the medium void fraction, S is the specific surface area of the scaffolds, and κ is the Kozeny constant ($\kappa \approx 5$ from experiments).(Bird, 1960) The specific surface area of the scaffolds can be obtained from μCT or it can be estimated with other techniques. Therefore, since the BKC equation is well established, simple to use and versatile, it can be the equation of choice for making predictions, when detailed fluid dynamics simulation results or measurements are not available.

Thus far the WT equation in conjunction with permeability obtained from the BKC equation has been used to obtain an estimate of $\bar{\tau}_W$ within porous scaffolds. The next step is to obtain the standard deviation of the pdf that τ_w follows. This can be done by taking advantage of the knowledge of the three parameters that describe the $\Gamma(\alpha,\gamma,\beta)$ pdf that the normalized shear stress follows, and of their relationship with the parameters that characterize the pdf that the dimensional stress follows. It can be shown via a substitution of variables that a variable with a $\hat{\Gamma}(\hat{\alpha},0,\hat{\beta})$ pdf can be transformed, using the normalization suggested in Equation (35), into a variable with $\Gamma(\alpha,\gamma,\beta)$ pdf. The parameters of these two pdfs are related as follows:

$$\alpha = \hat{\alpha},\ \beta = \hat{\beta}/\sigma_\tau, \text{ and } \gamma = (-\bar{\tau}_W)/\sigma_\tau \tag{42}$$

The coefficient of variation (and therefore the standard deviation σ_τ) for the pdf of the dimensional stress is then

$$\sigma_\tau / \bar{\tau}_W = -1/\gamma \approx 0.7 \tag{43}$$

Finally, the rest of the parameters of the $\hat{\Gamma}(\hat{\alpha},0,\hat{\beta})$ pdf for τ_w can be obtained as follows:

$$\hat{\alpha} = \alpha = 2.91 \text{ and } \hat{\beta} = \beta\sigma_\tau \approx 0.315\hat{\tau}_W \tag{44}$$

The pdf that the dimensional wall shear stress follows can now be fully described when the average stress, $\bar{\tau}_W$, is known. A further implication is that the mode value of τ_w (arguably more important than the average, since this is the most frequent τ_w value and likely the one that most cells would experience in the scaffold) can be readily calculated as

$$(\hat{\alpha}-1)\hat{\beta} \approx 0.6\bar{\tau}_W \tag{45}$$

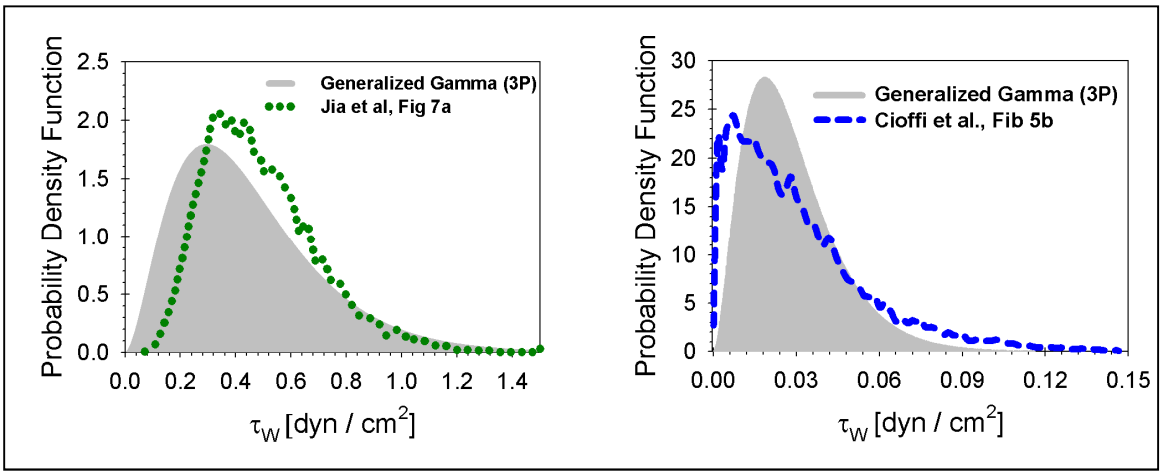

Figure 42 Left - Comparison of an experimentally obtained dimensional pdf (Dark Green Dotted) from Figure 7 in (Jia, Bagnaninchi et al., 2009) and Right - Comparison of a computationally obtained dimensional pdf (Dark Blue Dashed) from Figure 5 in (Cioffi, Kuffer et al., 2008) with the predicted dimensional WSS pdf obtained from knowledge of the average τ_w and the methodology suggested in this letter for calculating the gamma distribution (Light Gray Filled). Image from (Voronov, VanGordon et al., 2010).

In order to test the ability of the $\hat{\Gamma}(\hat{\alpha},0,\hat{\beta})$ pdf developed in this work to predict dimensional WSS values, the distributions shown in their reduced form in Figure 40 were predicted in their dimensional form from prior knowledge of the average stress, $\bar{\tau}_W$, only,

and the parameters in Equation (44). Figure 42 is a comparison of the predicted WSS distributions to the actual ones for an experimental and for a computational study from other laboratories. From Figure 42 it is apparent that there is close correspondence between the predicted and the actual pdfs. In order to statistically quantify the agreement between them, the null hypothesis that actual pdf is described by the predicted pdf was examined using the KS test. The results of the KS test show that the predicted pdfs describe the actual WSS distributions to within acceptable significance limits, and are summarized in Table 10. Considering the amount of error that is incorporated in using DataTheif to extract data from other publications, the error from statistically fitting the reduced $\Gamma(\alpha,\gamma,\beta)$ pdfs, and the error arising from the assumptions required in order to arrive at Equation (44), the results of Table 10 are rather impressive. The fact that the WSS distribution can be predicted simply from the knowledge of the average stress, $\bar{\tau}_W$, provides a powerful tool for quick estimation of the WSS distributions within highly porous constructs without the need for expensive and time consuming simulations or experiments. This has much significance in bone tissue engineering, where tissue growth is affected by the WSS experienced within scaffolds, as well as in many other disciplines.

Table 10 Levels of significance for data from different laboratories at which the null hypothesis that the actual dimensional data is described by the $\hat{\Gamma}\left(\hat{\alpha},0,\hat{\beta}\right)$ distribution [with parameters obtained from Equation (44)] cannot be rejected. *Note: data is smoothed using Loess method.

Source	Significance level
Figure 5a in (Cioffi, Kuffer et al., 2008)*	0.05
Figure 5b in (Cioffi, Kuffer et al., 2008)	0.05
Figure 7a in (Jia, Bagnaninchi et al., 2009)	0.10
Figure 7b in (Jia, Bagnaninchi et al., 2009)	0.15
Figure 6a in (Jungreuthmayer, Donahue et al., 2009)	0.20
Non-woven PLLA Fiber Mesh (unpublished data)	0.20

V.2 MASS TRANSFER & REACTIONS IN BTE SCAFFOLDS

As previously discussed in Section I.2-b, prompt delivery of O_2 is vital to cell survival in 3D cell culture constructs. In order to model mass transfer using the LST method two input parameters are needed: the Schmidt number and the reaction probability that corresponds to the nominal reaction rate at the wall for the molecule in question. For a fixed fluid viscosity and flow rate, only the diffusion coefficient of the solute in the solvent is needed in order to specify the Schmidt number. The molecular diffusivity for O_2 that is available in literature (it is assumed the cell culture medium is an aqueous solution at T = 37°C) and the corresponding Schmidt number are presented in Table 11.

Table 11 Molecular diffusivity of O_2 from literature and the corresponding Schmidt number, assuming that the fluid dynamic viscosity of water is 0.01 g / (cm s).

Source	Solute	Diffusivity in H_2O [cm^2 / s]	Schmidt Number
(Han and Bartels, 1996)	Molecular Oxygen @ T = 37 ºC	2.62×10^{-5}	328.14

Since the LST algorithm described in this work can perform calculations for a range of reaction probabilities using a single set of solute particles, the nutrient consumption can be modeled via a parametric study in which the 1st order reaction coefficient is varied over a wide range of values. Two PLLA scaffolds of each type (foam and nonwoven fiber mesh) were scanned at 10μm resolution and used to model four flow rates common to the laboratory setting: 0.15, 0.5, 0.77 and 1.0 mL / min. The surface of the scaffolds is assumed to be uniformly covered with a monolayer of cells, which have a probability to consume oxygen upon its collision with the scaffold's surface.

V.2-a Survival Distance within BTE Scaffolds

As a proof of concept study, the limiting case of 100% consumption upon every collision is examined. This corresponds to an infinite nominal reaction rate (i.e., instantaneous reaction) and should be treated as a limiting case scenario that allows for a comparison of the scaffold types on an equivalent basis. Figure 43 is a plot of the survival distance in the streamwise direction as a function of surface area per total volume ratio and perfusion flow rate as the nominal reaction rate tends to infinity. The survival distance is defined as the distance that the LST markers travel on average until they are consumed via a collision with the wall. It is apparent that the survival distance in the streamwise direction increases as the flow rate goes up. This is consistent with Taylor-Aris dispersion theory, which states that the effective diffusivity in the streamwise direction should increase with the square of the Peclet number.

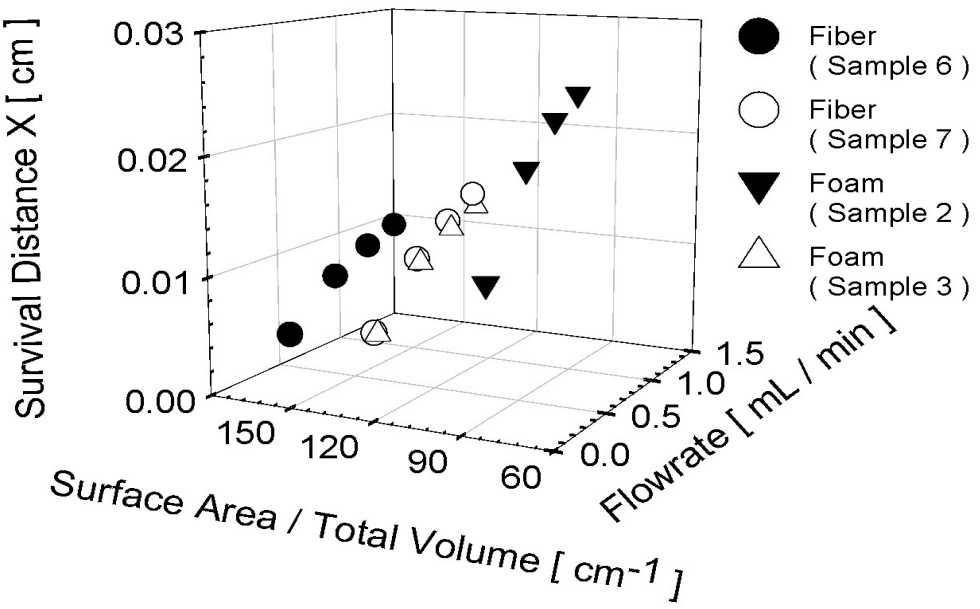

Figure 43 Survival distance in the streamwise X direction as a function of surface area per total volume ratio and perfusion flow rate as the nominal reaction rate tends to infinity. All scaffolds are approximately 85% porous.

Another trend that can be observed from Figure 43 is that the survival distance in the streamwise direction decreases with more surface area in the volume of the scaffold. This is because the collision of the LST markers with the scaffold wall is more probable when the scaffold has more surface area. Interestingly, the survival distances in the directions perpendicular to the streamwise direction actually decrease with flow rate. This is shown in Figure 44.

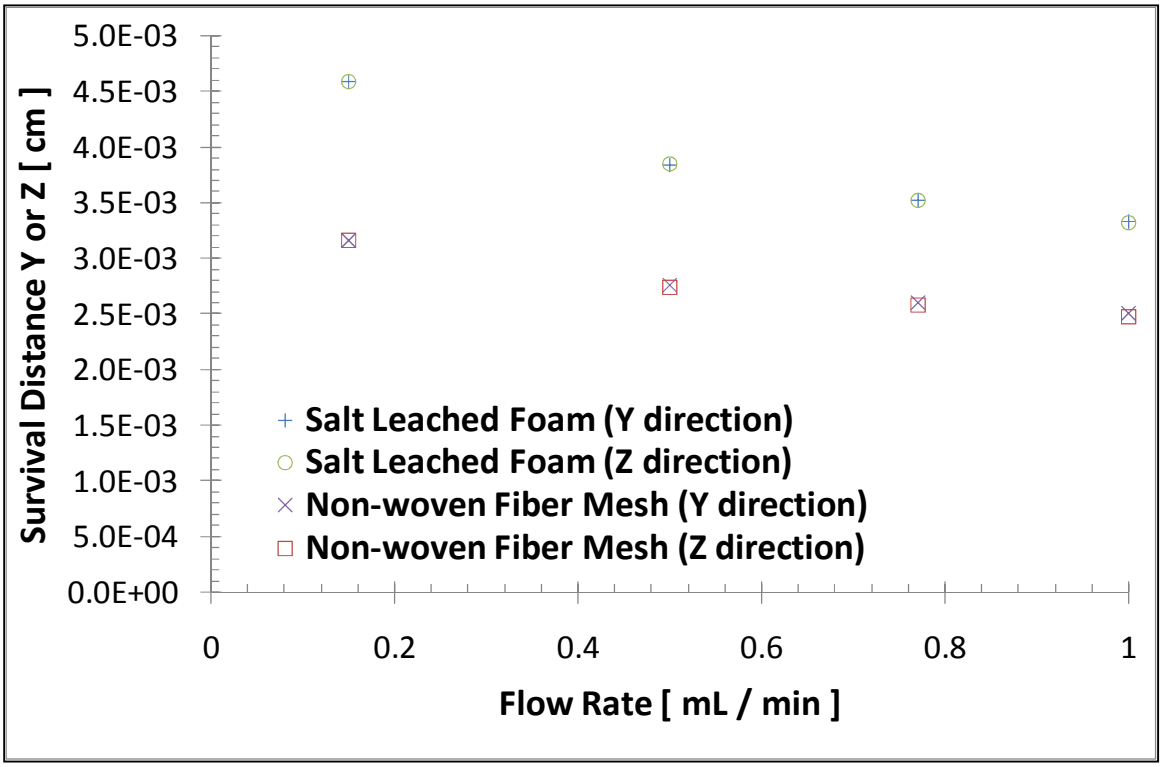

Figure 44 Survival distance in the Y & Z directions for two scaffolds (one foam and one fiber) as a function of perfusion flow rate as the nominal reaction rate tends to infinity. Both scaffolds are 85% porous with the fiber scaffold having more surface area per total volume.

The reason why the survival distance in the Y and Z directions decreases with flow rate is likely because the particles move less in those directions per time step relative to their movement in the direction of flow. Therefore, they transverse less distance prior to being consumed in the Y and Z directions. However, since both the Y

and Z survival distances are an order of magnitude smaller than the survival distance in the direction of flow, the total survival distance is dominated by the trend displayed by survival distance in the X direction.

V.2-b Survival Time

Figure 45 is a plot of the survival time as a function of surface area per total volume ratio and perfusion flow rate as the nominal reaction rate tends to infinity. The survival time is defined as the average time from the beginning of the simulation that the LST markers survive as they are consumed via a collision with the wall.

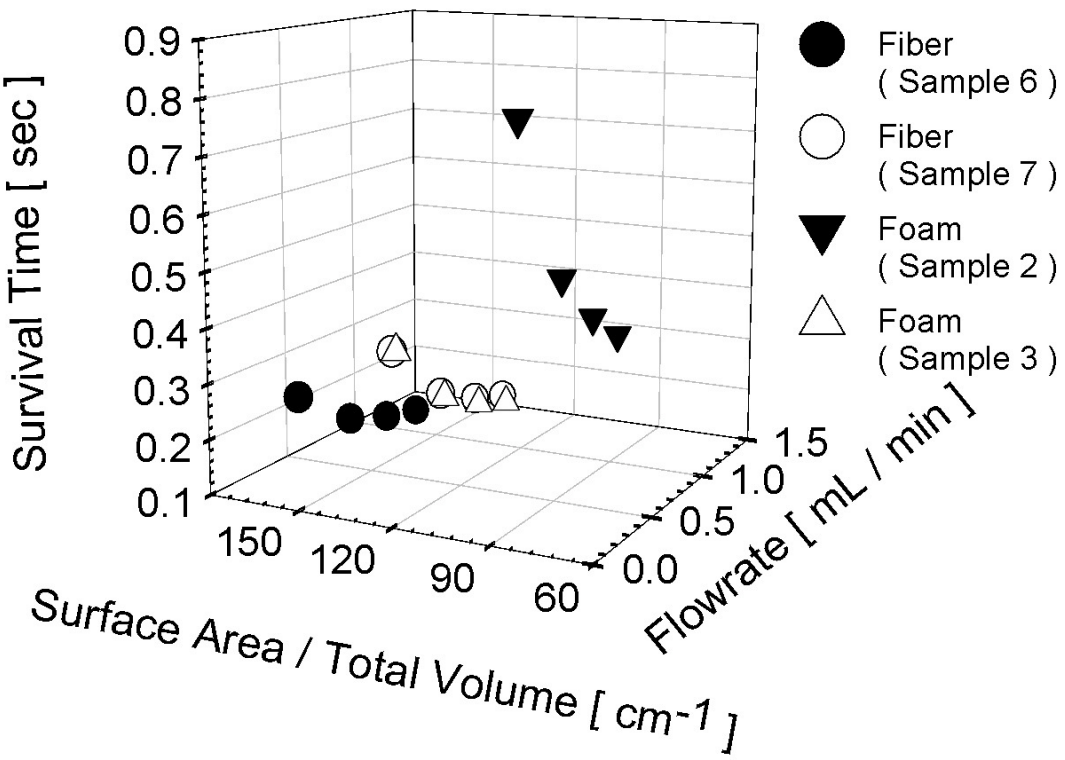

Figure 45 Survival time as a function of surface area per total volume ratio and perfusion flow rate as the nominal reaction rate tends to infinity. All scaffolds are approximately 85% porous.

Figure 45 is a plot of the survival time for the limiting case of an infinitely reactive solute, similar to Figure 43 and Figure 44. Combining the trends from these

three figures indicates that the reactive solutes get carried to a farther distance by a higher flow rate, but they take a shorter time to react. A peculiar thing about reactive solutes is that their average velocity is actually different from the average velocity experienced by a non-reactive solute. This occurs because for the reactive solute, those particles that got consumed no longer contribute to the average velocity, whereas in the case of the non-reactive solute the particles near the wall do not get consumed and have near zero velocities. In essence, the reactive solute will always be traveling faster because it lacks the low velocity particles near the walls. So the effect of an increasing flow rate on a reactive solute is that it will get consumed even faster, which in turn means a faster depletion of low velocity particles near the wall (and a faster effective average velocity). Apparently, this increase in the effective average velocity due to the higher flow rate is more significant than the increase in the effective reaction rate, due to the higher flow rate and the reactive solute travels farther into the scaffold. Similar to the survival distance trend, a higher surface area per total volume ratio decreases the survival time, because there is more opportunity for collisions to occur.

V.2-c Effective 1st Order Reaction Rate Constant

Figure 46 is a plot of the effective 1st order reaction rate constant as a function of surface area per total volume ratio and perfusion flow rate as the nominal reaction rate tends to infinity. The effective 1st order reaction rate constant is defined as the rate constant for an effective 1st order reaction rate that takes into account the effects of the presence of the porous media.

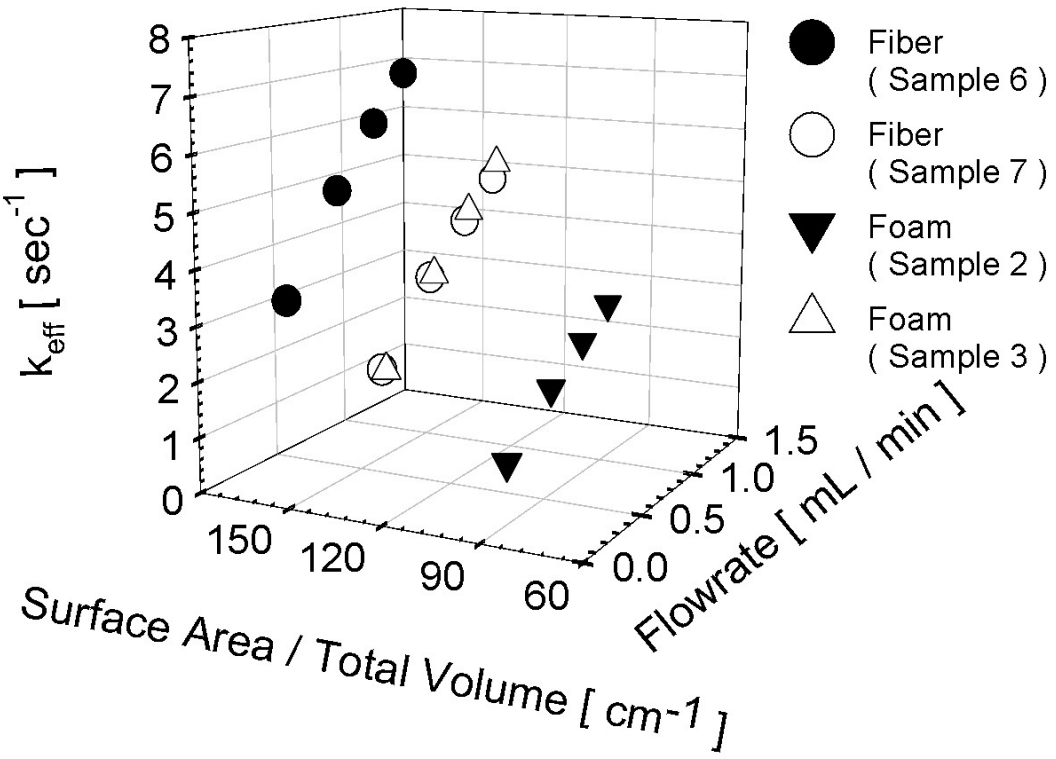

Figure 46 Effective 1st order reaction constant as a function of surface area per total volume ratio and perfusion flow rate as the nominal reaction rate tends to infinity. All scaffolds are approximately 85% porous.

Figure 46 reaffirms the previously observed trends: solute reacts faster at higher surface area per total volume ratio and flow rate increases the effective reactivity of the solute (i.e., the solute reach the scaffold wall in less time at a higher flow rate).

VI. CONCLUSIONS

In 2004, musculoskeletal disorders cost the US nearly $850 billion – 7.7% of the GDP, with 1 in 4 Americans requiring medical attention.(AAOS, 2008) A very promising alternative approach in regenerating bone is BTE using biodegradable scaffolds (Caplan and Goldberg, 2004) seeded with bone forming pre-osteoblastic MSCs. Bone tissue formation within scaffolds can be stimulated in two major ways: *mechanically* (fluid shear stress) and *chemically* (delivery of oxygen, nutrients/growth factors/cell signaling molecules and removal of waste). Information about the microenvironment within scaffolds is not readily available from experiment. Therefore, LBM and LST simulations are used in order to characterize the mechanical and chemical microenvironments within the scaffold, respectively.

Assuming that a target amount of stimulatory shear stress is known, flow within scaffolds can be adjusted in accordance with the correlations presented in this study in order to achieve, on average, the desired stress value. Equations (31) and (32) can be used to estimate the average stress if no prior information about the internal scaffold architecture is known, but they require measuring the pressure drop. The WT Equation [see Equation (40)] does not require a pressure drop measurement, but it requires knowledge of Darcy's permeability, which is presented in Table 6. There does not appear to be a scaffold manufacturing parameter that could be used to maximize the distribution of a desired amount of stress to the majority of the cells (while minimizing the exposure to undesired extreme stress values). All porosity – NaCl grain size combinations seem to produce about the same percentage of standard deviation when normalized by the mean stress value.

In fact the pdf of the WSS within highly porous scaffolds seems to follow a general distribution regardless of the internal scaffold architecture. The gamma distribution [see Equation (36)], along with the knowledge of average τ_w and parameters given in Equation (44), can be used to provide an estimate of this pdf within statistically acceptable limits. A simple procedure for obtaining a quick estimate of average τ_w based on the well established BKC equation (where the WT equation with $B \approx 1$ can be used to provide the permeability of the porous medium) was illustrated as a part of this work. Published results for the normalized τ_w distribution in various tissue engineering constructs fit without statistically significant error the Gamma-3P distribution with the suggested parameter values. This provides for a quick and rather simple method for obtaining the τ_w distribution for flow through highly porous media, thereby eliminating the need of detailed simulations or experiments. Furthermore, based on properties of the $\hat{\Gamma}\left(\hat{\alpha},0,\hat{\beta}\right)$ pdf the mode value of τ_w (the most frequent value of τ_w) is also available from Equation (45).

However, one must keep in mind that the Gamma-3P distribution was chosen based on statistical arguments only and there is no obvious physical interpretation for why a gamma distribution should describe the universal τ_w distribution. Having said that, the very fact that a single distribution such as the one reported herein exists, serves as evidence that an analytical form of such a distribution could exist. Finally, it must be emphasized that this methodology provides an estimate of the τ_w distribution only, and does not provide for a way to determine the exact values of τ_w or their locality. If such information is needed, one must still perform simulations, experiments or both. For

example, in defective scaffolds higher stress values are observed near the porous defects. Such information could not have been captured without performing the simulation.

The presence of manufacturing defects could explain why tissue buildups have been observed in certain parts of the scaffolds and not in others in experimental studies. It also emphasizes the importance of quality control in the scaffold manufacturing process. Since the fluid dynamics simulations performed in this study are not sensitive to the scaffold material, the results of this study can be applicable to other polymer systems provided that they are manufactured by a similar process, while the imaging/modeling approach is applicable to all scaffolds relevant to tissue engineering.

Mass transfer with chemical reaction for flows through porous media is of interest to many disciplines with bone tissue engineering being an interesting case study. The lattice Boltzmann method is particularly attractive for calculating the velocity field within such constructs due to the ease with which it handles complicated boundary conditions. It is also computationally attractive due to its inherent parallelizability. However, useful Lagrangian information (such as solute survival distance, effective diffusivity coefficient, collision frequency, etc.) is challenging to obtain, despite the recent attempts to modify the LBM algorithm.

A novel algorithm has been presented for modeling solute transport with first order heterogeneous reaction using the Lagrangian scalar tracking in conjunction with LBM (though the algorithm could have been used with any fluid dynamics solver). The reactions modeled in this work were heterogeneous, first order, irreversible chemical reactions between the solute and the solid boundary. The LST approach naturally provides useful Lagrangian information and has some advantages over modified LBM

solute transport techniques, such as the ability to simulate various Schmidt number solutes and different solute release modes with a single solvent flow field obtained from a LBM simulation. Additionally, LST allowed the simulation of the whole spectrum of solute reaction rates using just a single flow field obtained from LBM. Although some preliminary validation and results have been presented as a part of this work, the bulk of the mass transfer investigation is left for future work. The preliminary LST results seem to indicate that the nutrients travel longer distances but survive less time at higher flow rates. At high surface area per total volume ratio of the scaffolds the nutrients are more likely to experience a collision with the scaffold wall, and therefore travel shorter distances and survive for less time.

VII. FUTURE WORK

VII.1 EFFECTIVE DIFFUSIVITY & TORTUOSITY

In order to investigate further the effect of the scaffold architecture on mass transfer and reaction within scaffolds, the paths of the LST markers must be examined. Tortuosity is a useful quantity for this purpose, as it examines how twisted a curve is. One of the most common definitions of tortuosity in 2D is the arc-chord ratio: ratio of length of the curve to the shortest distance between its ends (chord). The arc-chord ratio is illustrated in Figure 47.

$$Tortuosity = \frac{Length}{Chord} \tag{46}$$

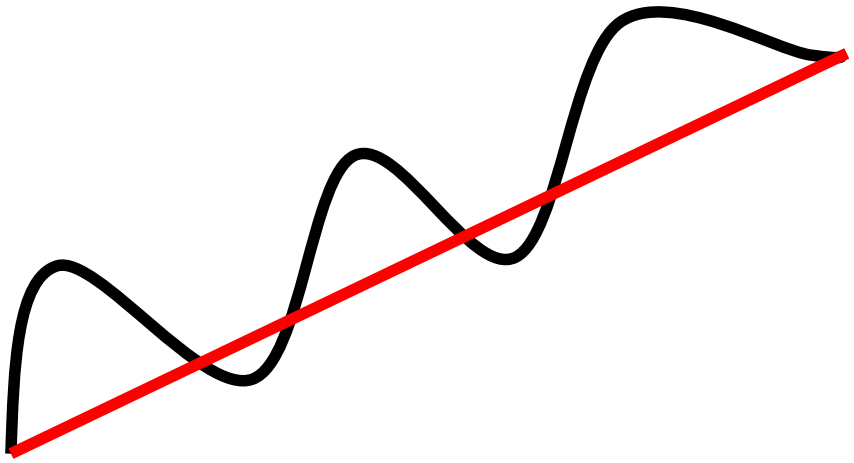

Figure 47 The "arc-chord" ratio definition of tortuosity for two dimensions. Tortuosity is defined as the ratio of length of the curve (Black line) to the shortest distance between its ends or the "chord" (Red line). Tortuosity is 1 for a straight line, and 0 for a circle.

For 3D porous media, such as the BTE scaffolds examined in this study, the tortuosity can be related to the diffusion coefficient of the solute travelling through the scaffold.(Nakashima and Watanabe, 2002; Nakashima and Kamiya, 2007)

As discussed previously, for unrestricted diffusion, such as diffusion in bulk fluid, the MSD is linear with respect to time and thus the nominal diffusion coefficient, D_o, is constant because of the homogeneity of space traversed by the particles. In porous media, however, there is local heterogeneity due to the pore structure, and thus the effective diffusion coefficient, D_{eff}, displays a time-dependent behavior for short time periods. The solid matrix of the porous medium serves as an obstacle to the movement of particles and, therefore, restricts their trajectories. This in turn reduces the diffusion coefficient relative to the nominal value in the bulk, such that $D_{eff} / D_o < 1$. In the short time limit, this ratio is proportional to the surface-to-volume ratio of porous media (Nakashima and Watanabe, 2002)

$$\frac{D_{eff}}{D_o} = 1 - \frac{4}{9\sqrt{\pi}} S_{pore} \sqrt{D_o t} + c_1 t \quad \text{as } t \to 0, \text{where } c_1 \text{is a constant} \tag{47}$$

In the long time limit, the particles travel much farther than the average pore size and experience the full tortuosity of the porous medium (the effective diffusion coefficient reaches a constant value). If the geometrical tortuosity of the porous medium is defined as the ratio of D_o/D_{eff} as $t \rightarrow \infty$, then it is possible to calculate the tortuosity by performing a long-time LST simulation.

VII.2 MASS TRANSFER & REACTIONS IN BTE SCAFFOLDS

As previously discussed, prompt delivery of Glucose as well as efficient removal of Lactate are vital to cell survival in 3D cell culture constructs. Table 12 is a summary of the molecular diffusivity data for Glucose and Lactate (ionic version of Lactic Acid) that is available in literature.

Table 12 Molecular diffusivity literature data for Glucose and Lactate in water at dilute concentrations.

Source	Solute	Diffusivity in H_2O[cm^2 / s]
	α-D-Glucose @ 25ºC	0.67×10^{-5}
(Ribeiro et al., 2005)	Lactic Acid @ 20ºC	0.99×10^{-5}
	Lactic Acid @ 30ºC	1.13×10^{-5}

As part of future work, it would be interesting to explore the Schmidt numbers that correspond to Glucose and Lactate for different scaffold geometries and perfusion flow rates. Effects of varying porosity and the average pore size could also be explored. For the Lactate simulations, a surface release could be utilized in order to measure how long it takes for this solute type to be eliminated from the scaffold. Since Lactate is not consumed by the cells, it would be modeled as a non-reactive species. Parametric LST studies as a function of the Damkohler number could be performed in order to gain understanding of the nutrient delivery and waste removal processes within scaffolds. With knowledge obtained from these simulations, the scaffolds' architecture could be optimized simultaneously for mass transfer and reactions of several species that are relevant to a successful cell culture.

VII.3 ACCOUNT FOR CELLS & TISSUE PRESENCE IN SCAFFOLDS

Thus far, it has been assumed that the cells cover the scaffolds in a uniform monolayer and that neither their presence, nor the presence of the tissue that they lay down affects the results. This is, however, a good assumption only for the first two weeks of the culturing process. After two weeks, the tissue growth begins to clog the pores of the scaffold and modify the flow field significantly. Therefore, the most immediate future goal is to be able to image the cells and the ECM that they produce

within the scaffold. This can be achieved by using more advanced imaging equipment (for example see Figure 48 for a 1.5μm resolution scan of a nonwoven fiber mesh scaffold) and/or x-ray contrasting techniques, such as using osmium tetroxide, iodine containing contrasts (lipiodol) or iodine tagged antibodies.(Ingenbleek et al., 1997; Ho and Hutmacher, 2006; van Lenthe et al., 2007; Guldberg et al., 2008; Dorsey et al., 2009)

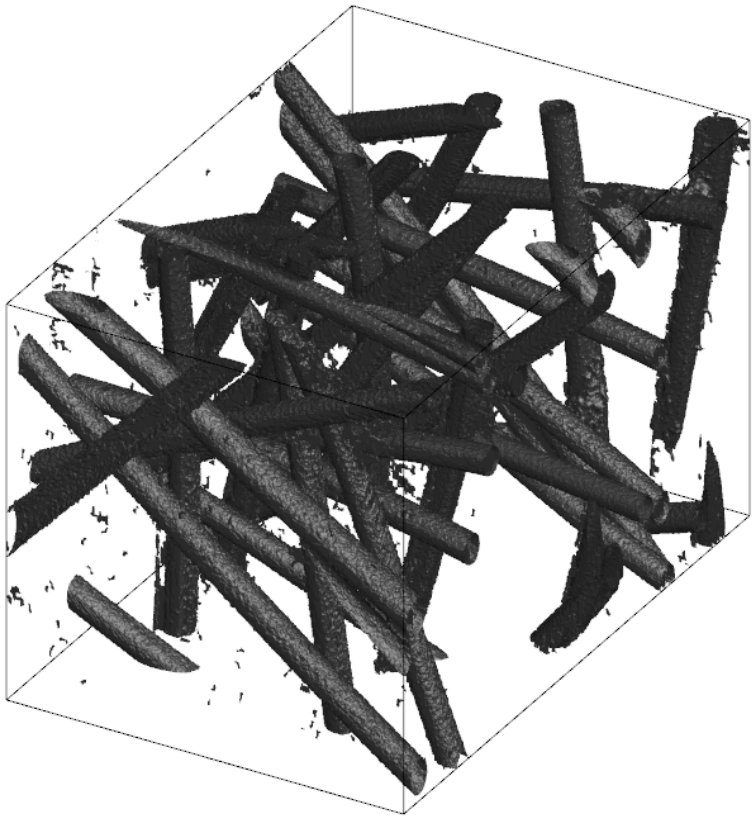

Figure 48 A high resolution (1.5 micron) μCT scan of a nonwoven fiber mesh PLLA scaffold produced in Dr. Shambaugh laboratory. The average fiber diameter is approximately 34μm.

VII.4 TISSUE GROWTH WITH TIME

Aside from the previously mentioned obstacles, the challenge of tissue engineering is further complicated by the transient nature of the tissue growth process within the scaffold as the cells are being cultured. Cell adhesion strengths change with

time as cell coverage grows from an initial monolayer coverage of the scaffold to cells adhering to layers of other cells and excreted extracellular matrix. Expansion of cells and tissue during the culturing period within the porous network of the scaffold creates continuously changing pore geometry and the biological environment inside the scaffold can be visualized as a continuously changing 3D matrix of tissue that dynamically responds to mechanical stresses. Therefore, it is important to explore local shear force distributions as well as the nutrient transport throughout the culturing process on scaffolds at different time points, in order to assess the tissue development with time.

Hard tissue has been previously imaged for long term cultures, but imaging of soft tissue has remained to be a challenge. Once both soft and hard tissue can be imaged, the effect of tissue presence can be explored at different time points throughout the culturing process. Ideally, the scanning of the scaffolds would be done on-line (in real time) without interrupting the experiment. However, if this is not possible then some samples would have to be taken out of the bioreactor and sacrificed for analysis, at different points. Based on these transient results, the 3D porous scaffold structure should be analyzed for optimum fluid shear and nutrient. The obtained results would allow to optimize the scaffold structure not only for the beginning of the tissue culture process, but also for long culturing times.

VII.5 PREDICT TISSUE GROWTH FROM SCAFFOLD GEOMETRY

The ultimate goal of this work would be to predict where tissue will grow based solely on the geometry of an arbitrary scaffold. An empty scaffold's geometry could be obtained using μCT imaging and LBM/LST simulations could be performed in order to

obtain the conditions experienced inside the scaffold during the tissue culturing process. Using this knowledge, areas of high tissue growth could be identified and later verified experimentally using histology or nondestructive imaging techniques. If the insight provided by the simulations is validated via experiment, the simulations could be used in order to design the scaffold geometry that is optimal for the specific tissue and culturing conditions at hand.

VIII. REFERENCES

AAOS (2008). United States Bone and Joint Decade: The Burden of Musculoskeletal Diseases in the United States. Rosemont, IL, American Academy of Orthopaedic Surgeons.

Agrawal, C. M., J. S. McKinney, et al. (2000). "Effects of fluid flow on the in vitro degradation kinetics of biodegradable scaffolds for tissue engineering." Biomaterials **21**(23): 2443-2452.

Allori, A. C., A. M. Sailon, et al. (2008). "Biological basis of bone formation, remodeling, and repair - Part III: Biomechanical forces." Tissue Engineering Part B-Reviews **14**(3): 285-293.

Allori, A. C., A. M. Sailon, et al. (2008). "Biological basis of bone formation, remodeling, and repair - Part I: Biochemical signaling molecules." Tissue Engineering Part B-Reviews **14**(3): 259-273.

Alvarez-Barreto, J. F., S. M. Linehan, et al. (2007). "Flow perfusion improves seeding of tissue engineering scaffolds with different architectures." Annals of Biomedical Engineering **35**(3): 429-442.

Alvarez-Barreto, J. F. and V. I. Sikavitsas (2006). Tissue Engineering Bioreactors. Tissue Engineering and Artificial Organs. J. D. Bronzino. Boca Raton

Boulder, C R C Press LLC

NetLibrary.

Alvarez-Barreto, J. F. and V. I. Sikavitsas (2007). "Improved mesenchymal stem cell seeding on RGD-modified poly(L-lactic acid) scaffolds using flow perfusion." Macromolecular Bioscience **7**(5): 579-588.

Bancroft, G. N., V. I. Sikavitsas, et al. (2002). "Fluid flow increases mineralized matrix deposition in 3D perfusion culture of marrow stromal osteloblasts in a dose-dependent manner." Proceedings of the National Academy of Sciences of the United States of America **99**(20): 12600-12605.

Bear, J. (1988). Dynamics of fluids in porous media. New York, Dover.

Bhatnagar, P. L., E. P. Gross, et al. (1954). "A Model for Collision Processes in Gases .1. Small Amplitude Processes in Charged and Neutral One-Component Systems." Physical Review **94**(3): 511-525.

Bhattacharya, A., O. B. Usta, et al. (2009). "Self-Sustained Motion of a Train of Haptotactic Microcapsules." Langmuir **25**(17): 9644-9647.

Bird, R. B. (1960). Transport phenomena. New York,, Wiley.

Bird, R. B., W. E. Stewart, et al. (2002). Transport phenomena. New York, J. Wiley.

Boschetti, F., M. T. Raimondi, et al. (2006). "Prediction of the micro-fluid dynamic environment imposed to three-dimensional engineered cell systems in bioreactors." Journal of Biomechanics **39**(3): 418-425.

Bose, S., J. Darsell, et al. (2003). "Pore size and pore volume effects on alumina and TCP ceramic scaffolds." Materials Science & Engineering C-Biomimetic and Supramolecular Systems **23**(4): 479-486.

Boyd, J., J. Buick, et al. (2006). "A second-order accurate lattice Boltzmann non-Newtonian flow model." Journal of Physics a-Mathematical and General **39**(46): 14241-14247.

Brinkman, H. C. (1947). "A Calculation of the Viscous Force Exerted by a Flowing Fluid on a Dense Swarm of Particles." Applied Scientific Research Section a-Mechanics Heat Chemical Engineering Mathematical Methods **1**(1): 27-34.

Burger, E. H. and J. Klein-Nulend (1999). "Mechanotransduction in bone - role of the lacuno-canalicular network." Faseb Journal **13**: S101-S112.

Caplan, A. I. and V. M. Goldberg (2004). Orthopedic tissue engineering : basic science and practices. New York, Marcel Dekker.

Cartmell, S., K. Huynh, et al. (2004). "Quantitative microcomputed tomography analysis of mineralization within three-dimensional scaffolds in vitro." Journal of Biomedical Materials Research Part A **69A**(1): 97-104.

Cartmell, S. H., B. D. Porter, et al. (2003). "Effects of medium perfusion rate on cell-seeded three-dimensional bone constructs in vitro." Tissue Engineering **9**(6): 1197-1203.

Chen, S. and G. D. Doolen (1998). "Lattice Boltzmann method for fluid flows." Annual Review of Fluid Mechanics **30**: 329-364.

Chung, C. A., C. W. Chen, et al. (2007). "Enhancement of cell growth in tissue-engineering constructs under direct perfusion: Modeling and simulation." Biotechnology and Bioengineering **97**(6): 1603-1616.

Cioffi, M., F. Boschetti, et al. (2006). "Modeling evaluation of the fluid-dynamic microenvironment in tissue-engineered constructs: A micro-CT based model." Biotechnology and Bioengineering **93**(3): 500-510.

Cioffi, M., J. Kuffer, et al. (2008). "Computational evaluation of oxygen and shear stress distributions in 3D perfusion culture systems: Macro-scale and micro-structured models." Journal of Biomechanics **41**(14): 2918-2925.

Cosgrove, J. A., J. M. Buick, et al. (2003). "Application of the lattice Boltzmann method to transition in oscillatory channel flow." Journal of Physics a-Mathematical and General **36**(10): 2609-2620.

Cowin, S. C. (1999). "Bone poroelasticity." Journal of Biomechanics **32**(3): 217-238.

Cowin, S. C. (2001). Bone mechanics handbook. Boca Raton, FL, CRC Press.

de Rovere, A. and R. L. Shambaugh (2001). "Melt-spun hollow fibers for use in nonwoven structures." Industrial & Engineering Chemistry Research **40**(1): 176-187.

Ding, M., A. Odgaard, et al. (2002). "Age-related variations in the microstructure of human tibial cancellous bone." Journal of Orthopaedic Research **20**(3): 615-621.

Dorsey, S. M., S. Lin-Gibson, et al. (2009). "X-ray microcomputed tomography for the measurement of cell adhesion

and proliferation in polymer scaffolds." Biomaterials **30**: 2967–2974.

Einstein, A. (1905). "The motion of elements suspended in static liquids as claimed in the molecular kinetic theory of heat." Annalen Der Physik **17**(8): 549-560.

Fletcher, C. A. J. and K. Srinivas (1991). Computational techniques for fluid dynamics. Berlin ; New York, Springer-Verlag.

Fritton, S. P. and S. Weinbaum (2009). "Fluid and Solute Transport in Bone: Flow-Induced Mechanotransduction." Annual Review of Fluid Mechanics **41**: 347-374.

Gabbanelli, S., G. Drazer, et al. (2005). "Lattice Boltzmann method for non-Newtonian (power-law) fluids." Physical Review E **72**(4): -.

Goldstein, A. S., T. M. Juarez, et al. (2001). "Effect of convection on osteoblastic cell growth and function in biodegradable polymer foam scaffolds." Biomaterials **22**(11): 1279-1288.

Guarino, R. D., L. E. Dike, et al. (2004). "Method for determining oxygen consumption rates of static cultures from microplate measurements of pericellular dissolved oxygen concentration." Biotechnology and Bioengineering **86**(7): 775-787.

Guldberg, R. E., C. L. Duvall, et al. (2008). "3D imaging of tissue integration with porous biomaterials." Biomaterials **29**(28): 3757-3761.

Gunatillake, P. A. and R. Adhikari (2003). "Biodegradable Synthetic Polymers for Tissue Engineering." European Cells and Materials **5**: 1-16.

Han, P. and D. M. Bartels (1996). "Temperature dependence of oxygen diffusion in H2O and D2O." Journal of Physical Chemistry **100**(13): 5597-5602.

Ho, S. T. and D. W. Hutmacher (2006). "A comparison of micro CT with other techniques used in the characterization of scaffolds." Biomaterials **27**(8): 1362-1376.

Holland, T. A. and A. G. Mikos (2006). "Review: Biodegradable polymeric scaffolds. Improvements in bone tissue engineering through controlled drug delivery." Tissue Engineering I: Scaffold Systems for Tissue Engineering **102**: 161-185.

Hollister, S. J. (2009). "Scaffold Design and Manufacturing: From Concept to Clinic." Advanced Materials **21**(32-33): 3330-3342.

Holtorf, H. L., J. A. Jansen, et al. (2005). "Flow perfusion culture induces the osteoblastic differentiation of marrow stromal cell-scaffold constructs in the absence of dexamethasone." Journal of Biomedical Materials Research Part A **72A**(3): 326-334.

Holy, C. E., M. S. Shoichet, et al. (2000). "Engineering three-dimensional bone tissue in vitro using biodegradable scaffolds: Investigating initial cell-seeding density and culture period." Journal of Biomedical Materials Research **51**(3): 376-382.

Hutmacher, D. W. (2000). "Scaffolds in tissue engineering bone and cartilage." Biomaterials **21**(24): 2529-2543.

Ingenbleek, Y., L. Jung, et al. (1997). "Iodised rapeseed oil for eradication of severe endemic goitre." Lancet **350**(9090): 1542-1545.

Jaiswal, N., S. E. Haynesworth, et al. (1997). "Osteogenic differentiation of purified, culture-expanded human mesenchymal stem cells in vitro." Journal of Cellular Biochemistry **64**(2): 295-312.

Jia, Y. L., L. An, et al. (2009). "Doppler optical microangiography improves the quantification of local fluid flow and shear stress within 3-D porous constructs." Journal of Biomedical Optics **14**(5): -.

Jia, Y. L., P. O. Bagnaninchi, et al. (2009). "Doppler optical coherence tomography imaging of local fluid flow and shear stress within microporous scaffolds." Journal of Biomedical Optics **14**(3): -.

Jungreuthmayer, C., S. W. Donahue, et al. (2009). "A Comparative Study of Shear Stresses in Collagen-Glycosaminoglycan and Calcium Phosphate Scaffolds in Bone Tissue-Engineering Bioreactors." Tissue Engineering Part A **15**(5): 1141-1149.

Kandhai, D., A. Koponen, et al. (1998). "Lattice-Boltzmann hydrodynamics on parallel systems." Computer Physics Communications **111**(1-3): 14-26.

Kang, Q. J., P. C. Lichtner, et al. (2007). "An improved lattice Boltzmann model for multicomponent reactive transport in porous media at the pore scale." Water Resources Research **43**(12): -.

Karageorgiou, V. and D. Kaplan (2005). "Porosity of 3D biornaterial scaffolds and osteogenesis." Biomaterials **26**(27): 5474-5491.

Kohles, S. S., J. B. Roberts, et al. (2001). "Direct perfusion measurements of cancellous bone anisotropic permeability." Journal of Biomechanics **34**(9): 1197-1202.

Komarova, S. V., F. I. Ataullakhanov, et al. (2000). "Bioenergetics and mitochondrial transmembrane potential during differentiation of cultured osteoblasts." American Journal of Physiology-Cell Physiology **279**(4): C1220-C1229.

Kretlow, J. D. and A. G. Mikos (2008). "From Material to Tissue: Biomaterial Development, Scaffold Fabrication, and Tissue Engineering." Aiche Journal **54**(12): 3048-3067.

Krinner, A., M. Zscharnack, et al. (2009). "The Impact of the Oxygen Environment on Mesenchymal Stem Cell Expansion and Chondrogenic Differentiation." Tissue Engineering Part A **15**(5): O13-O14.

Laib, A., O. Barou, et al. (2000). "3D micro-computed tomography of trabecular and cortical bone architecture with application to a rat model of immobilisation osteoporosis." Medical & Biological Engineering & Computing **38**(3): 326-332.

Lakhotia, S. and E. T. Papoutsakis (1992). "Agitation Induced Cell Injury in Microcarrier Cultures - Protective Effect of Viscosity Is Agitation Intensity Dependent - Experiments and Modeling." Biotechnology and Bioengineering **39**(1): 95-107.

Laurencin, C., Y. Khan, et al. (2006). "Bone graft substitutes." Expert Review of Medical Devices **3**(1): 49-57.

Lekien, F. and J. Marsden (2005). "Tricubic interpolation in three dimensions." International Journal for Numerical Methods in Engineering **63**(3): 455-471.

Liu, X. and P. X. Ma (2004). "Polymeric scaffolds for bone tissue engineering." Ann Biomed Eng **32**(3): 477-486.

Liu, X. H. and P. X. Ma (2004). "Polymeric scaffolds for bone tissue engineering." Annals of Biomedical Engineering **32**(3): 477-486.

Lu, L. C., S. J. Peter, et al. (2000). "In vitro degradation of porous poly(L-lactic acid) foams." Biomaterials **21**(15): 1595-1605.

Maes, F., P. Ransbeeck, et al. (2009). "Modeling Fluid Flow Through Irregular Scaffolds for Perfusion Bioreactors." Biotechnology and Bioengineering **103**(3): 621-630.

Majumdar, B. and R. L. Shambaugh (1990). "Air Drag on Filaments in the Melt Blowing Process." Journal of Rheology **34**(4): 591-601.

Malda, J., P. Van den Brink, et al. (2004). "Effect of oxygen tension on adult articular chondrocytes in microcarrier bioreactor culture." Tissue Engineering **10**(7-8): 987-994.

Malkan, S. R. (1995). "An Overview of Spunbonding and Meltblowing Technologies." Tappi Journal **78**(6): 185-190.

Matsumoto, M. and T. Nishimura (1998). "Mersenne twister: a 623-dimensionally equidistributed uniform pseudo-random number generator." ACM Transactions on Modeling and Computer Simulation (TOMACS) **8**(1): 3-30.

McNamara, G. R. and G. Zanetti (1988). "Use of the Boltzmann-Equation to Simulate Lattice-Gas Automata." Physical Review Letters **61**(20): 2332-2335.

Mikos, A. G., M. D. Lyman, et al. (1994). "Wetting of poly(L-lactic acid) and poly(DL-lactic-co-glycolic acid) foams for tissue culture." Biomaterials **15**(1): 55-58.

Mitrovic, B. M. and D. V. Papavassiliou (2004). "Effects of a first-order chemical reaction on turbulent mass transfer." International Journal of Heat and Mass Transfer **47**(1): 43-61.

Moretti, M., D. Wendt, et al. (2005). "Effects of in vitro preculture on in vivo development of human engineered cartilage in an ectopic model." Tissue Engineering **11**(9-10): 1421-1428.

Nabovati, A., E. W. Llewellin, et al. (2009). "A general model for the permeability of fibrous porous media based on fluid flow simulations using the lattice Boltzmann method." Composites Part a-Applied Science and Manufacturing **40**(6-7): 860-869.

Nakashima, Y. and S. Kamiya (2007). "Mathematica programs for the analysis of three-dimensional pore connectivity and anisotropic tortuosity of porous rocks using X-ray computed tomography image data." Journal of Nuclear Science and Technology **44**(9): 1233-1247.

Nakashima, Y. and Y. Watanabe (2002). "Estimate of transport properties of porous media by microfocus X-ray computed tomography and random walk simulation." Water Resources Research **38**(12): -.

Nguyen, K. T. and D. V. Papavassiliou (2008). "Effects of a reacting channel wall on turbulent mass transfer." International Journal of Heat and Mass Transfer **51**(11-12): 2940-2949.

Nguyen, K. T. and D. V. Papavassiliou (2008). "Flow effects on the kinetics of a second-order reaction." Chemical Engineering Journal **140**(1-3): 370-380.

Papavassiliou, D. V. (2002). "Turbulent transport from continuous sources at the wall of a channel." International Journal of Heat and Mass Transfer **45**(17): 3571-3583.

Papavassiliou, D. V. (2006). Understanding macroscopic heat/mass transfer using meso- and macro-scale simulations. Model Reduction and Coarse-Graining Approaches for Multiscale Phenomena. A. N. Gorban, N. Kazantzis, Y. G. Kevrekidis, H. C. Ottinger and C. Theodoropoulos. Berlin; New York, Springer-Verlag**:** 489-515.

Papavassiliou, D. V. and T. J. Hanratty (1995). "The Use of Lagrangian-Methods to Describe Turbulent Transport of Heat from a Wall." Industrial & Engineering Chemistry Research **34**(10): 3359-3367.

Porter, B., R. Zauel, et al. (2005). "3-D computational modeling of media flow through scaffolds in a perfusion bioreactor." Journal of Biomechanics **38**(3): 543-549.

Probstein, R. F. (1989). Physicochemical hydrodynamics : an introduction. Boston, Butterworths.

Qian, Y. H., D. Dhumieres, et al. (1992). "Lattice Bgk Models for Navier-Stokes Equation." Europhysics Letters **17**(6bis): 479-484.

Raimondi, M. T., M. Moretti, et al. (2006). "The effect of hydrodynamic shear on 3D engineered chondrocyte systems subject to direct perfusion." Biorheology **43**(3-4): 215-222.

Ribeiro, A. C. F., V. M. M. Lobo, et al. (2005). "Binary diffusion coefficients for aqueous solutions of lactic acid." Journal of Solution Chemistry **34**(9): 1009-1016.

Sandino, C., J. A. Planell, et al. (2008). "A finite element study of mechanical stimuli in scaffolds for bone tissue engineering." Journal of Biomechanics **41**(5): 1005-1014.

Sikavitsas, V. I., G. N. Bancroft, et al. (2003). "Mineralized matrix deposition by marrow stromal osteoblasts in 3D perfusion culture increases with increasing fluid shear forces." Proceedings of the National Academy of Sciences of the United States of America **100**(25): 14683-14688.

Sikavitsas, V. I., G. N. Bancroft, et al. (2005). "Flow perfusion enhances the calcified matrix deposition of marrow stromal cells in biodegradable nonwoven fiber mesh scaffolds." Annals of Biomedical Engineering **33**(1): 63-70.

Sikavitsas, V. I., J. S. Temenoff, et al. (2001). "Biomaterials and bone mechanotransduction." Biomaterials **22**(19): 2581-2593.

Skartsis, L., J. L. Kardos, et al. (1992). "Resin Flow through Fiber Beds during Composite Manufacturing Processes .1. Review of Newtonian Flow through Fiber Beds." Polymer Engineering and Science **32**(4): 221-230.

Stathopoulos, N. A. and J. D. Hellums (1985). "Shear-Stress Effects on Human-Embryonic Kidney-Cells Invitro." Biotechnology and Bioengineering **27**(7): 1021-1026.

Stevens, B., Y. Z. Yang, et al. (2008). "A review of materials, fabrication methods, and strategies used to enhance bone regeneration in engineered bone tissues." Journal of Biomedical Materials Research Part B-Applied Biomaterials **85**(2): 573-582.

Stolberg, S. and K. E. McCloskey (2009). "Can Shear Stress Direct Stem Cell Fate?" Biotechnology Progress **25**(1): 10-19.

Stylianopoulos, T., A. Yeckel, et al. (2008). "Permeability calculations in three-dimensional isotropic and oriented fiber networks." Physics of Fluids **20**(12): -.

Succi, S. (2001). The lattice Boltzmann equation for fluid dynamics and beyond. Oxford New York, Clarendon Press ;
Oxford University Press.

Sukop, M. C., D. T. Thorne, et al. (2006). Lattice Boltzmann modeling an introduction for geoscientists and engineers. Berlin ; New York, Springer**:** ix, 172 p.

Swift, M. R., E. Orlandini, et al. (1996). "Lattice Boltzmann simulations of liquid-gas and binary fluid systems." Physical Review E **54**(5): 5041-5052.

Tandler, B., G. Schmack, et al. (2001). "Melt processing of a new biodegradable synthetic polymer in high-speed spinning and underpressure spunbonding process." Journal of Polymers and the Environment **9**(4): 149-156.

Tate, M. L. K., U. Knothe, et al. (1998). "Experimental elucidation of mechanical load-induced fluid flow and its potential role in bone metabolism and functional adaptation." American Journal of the Medical Sciences **316**(3): 189-195.

Thummala, N. (2004). Convective heat transfer in microfluidics using Lagrangian methods and lattice Boltzmann simulations. School of Chemical, Biological and Materials Engineerin. Norman, University of Oklahoma. **MS**.

Tomadakis, M. M. and D. Rupani (2007). "Diffusion controlled reaction rate, survival probability, and molecular trajectory characteristics in the bulk, transition and Knudsen regime." Chemical Engineering Journal **128**(1): 1-10.

Toolan, B. C. (2006). "Current concepts review: Orthobiologics." Foot & Ankle International **27**(7): 561-566.

Tuan, R. S., G. Boland, et al. (2003). "Adult mesenchymal stem cells and cell-based tissue engineering." Arthritis Research & Therapy **5**(1): 32-45.

Van Leemput, P., C. Vandekerckhove, et al. (2007). "Accuracy of hybrid lattice boltzmann/finite difference schemes for reaction-diffusion systems." Multiscale Modeling & Simulation **6**(3): 838-857.

van Lenthe, G. H., H. Hagenmuller, et al. (2007). "Nondestructive micro-computed tomography for biological imaging and quantification of scaffold-bone interaction in vivo." Biomaterials **28**(15): 2479-2490.

VanGordon, S., R. S. Voronov, et al. (2010). "Effects of Scaffold Architecture on Preosteoblastic Cultures under Continuous

Fluid Shear." Industrial & Engineering Chemistry Research (In Print).

Voronov, R. S., S. VanGordon, et al. (2010). "Computational Modeling of Flow Induced Shear Stresses Within 3D Salt-Leached Porous Scaffolds Imaged via Micro-CT." Journal of Biomechanics **43**(7): 1279-1286.

Voronov, R. S., S. VanGordon, et al. (2010). "Efficient Lagrangian scalar tracking method for reactive local mass transport simulation through porous media " International Journal for Numerical Methods in Fluids (In Print).

Voronov, R. S., S. VanGordon, et al. (2010). "A General Flow-Induced Wall Shear Stress Distribution Within High Porosity Scaffolds." (Under Review).

Vunjak-Novakovic, G., B. Obradovic, et al. (1998). "Dynamic cell seeding of polymer scaffolds for cartilage tissue engineering." Biotechnology Progress **14**(2): 193-202.

Wang, D. M. and J. M. Tarbell (1995). "Modeling Interstitial Flow in an Artery Wall Allows Estimation of Wall Shear-Stress on Smooth-Muscle Cells." Journal of Biomechanical Engineering-Transactions of the Asme **117**(3): 358-363.

Wang, J. Y., X. X. Zhang, et al. (2005). "Domain-decomposition method for parallel lattice Boltzmann simulation of incompressible flow in porous media." Physical Review E **72**(1): -.

Wang, S. and J. M. Tarbell (2000). "Effect of fluid flow on smooth muscle cells in a 3-dimensional collagen gel model." Arteriosclerosis Thrombosis and Vascular Biology **20**(10): 2220-2225.

Weinbaum, S., S. C. Cowin, et al. (1994). "A Model for the Excitation of Osteocytes by Mechanical Loading-Induced Bone Fluid Shear Stresses." Journal of Biomechanics **27**(3): 339-360.

Wendt, D., M. Jakob, et al. (2005). "Bioreactor-based engineering of osteochondral grafts: from model systems to tissue manufacturing." Journal of Bioscience and Bioengineering **100**(5): 489-494.

Yoon, D. M. and J. P. Fisher (2006). Polymeric Scaffolds for Tissue Engineering Applications. The biomedical engineering handbook. v. 3, tissue engineering and artificial organs J. D. Bronzino. Boca Raton, CRC/Taylor & Francis**:** 1 v. (various pagings).

Yoshino, A., Y. Hotta, et al. (2007). "A numerical method for incompressible non-Newtonian fluid flows based on the lattice Boltzmann method." Journal of Non-Newtonian Fluid Mechanics **147**(1-2): 69-78.

Zeiser, T., M. Bashoor-Zadeh, et al. (2008). "Pore-scale analysis of Newtonian flow in the explicit geometry of vertebral trabecular bones using lattice Boltzmann

simulation." Proceedings of the Institution of Mechanical Engineers Part H-Journal of Engineering in Medicine **222**(H2): 185-194.
Zhang, D., G. Bhat, et al. (1997). "Structure and properties of polypropylene filaments in a spunbonding process." Journal of Thermal Analysis **49**(1): 161-167.
Zhao, F., P. Pathi, et al. (2005). "Effects of oxygen transport on 3-D human mesenchymal stem cell metabolic activity in perfusion and static cultures: Experiments and mathematical model." Biotechnology Progress **21**(4): 1269-1280.

IX. NOMENCLATURE

b – half height of a channel
B – proportionality constant in WT equation
c – the lattice speed ($\Delta x/\Delta t$) or an integration constant
C – concentration of reactant
D – diameter [cm] or mass diffusivity (a.k.a. diffusion coefficient) [cm^2 / s]
$\vec{e}$ – microscopic velocity in LBM
f - particle distribution function in LBM
ff – forcing factor in LBM [g / cm^2 s^2]
k – permeability of porous medium in Darcy's equation [cm^2] or 1st order reaction constant [s^{-1}] in LST
K – proportionality constant
L – length
N –denotes normal distribution
S – surface area per solid volume (a.k.a. specific surface area) [cm^{-1}]
$\vec{x}$ – position
p – number of MPI processes
P – pressure
Pe – dimensionless Peclet number
Sc – dimensionless Schmidt number
O – order of accuracy
q – nominal reaction probability in LST
r – radius [cm] or reaction rate
R – inside radius of a pipe [cm]
Re – dimensionless Reynolds number
t – time
T – temperature [ºC]
U – macroscopic velocity [cm / s]
w – lattice specific weighing factor in LBM

Greek:

α – shape parameter ($\alpha > 0$)
β – scale parameter ($\beta > 0$)
Δ – difference
ε – the porosity
μ - dynamic viscosity [g / (cm s)]
κ – Kozeny constant in the BKC equation
ν – kinematic visocisity
Ω – collision operator in LBM
σ – standard deviation
τ – fluid stress [dyn / cm^2] or relaxation time in LBM
Γ – three-parameter gamma (Gamma-3P) distribution that describes fluid stress

γ – location parameter ($\gamma = 0$ yields the standard gamma distribution $\Gamma(\alpha,0,\beta)$, i.e., the two-parameter gamma pdf)

Subscripts:
½ – half life [s]
o – nominal (at the wall)
0 – at time equals zero
eff - effective
i – lattice direction index in LBM
init – initial
j – solute component in a mixture
h – hydraulic
pore – in reference to pore space of porous media
s – superficial
t – at time equals to 't'
w – wall
x – direction of flow
τ – in relation to fluid stress

Superscripts:

eq – equillibrium
* – dimensionless
^ – in relation to Gamma-3P distribution describing the dimensional fluid stresses

APPENDIX

Appendix - I Derivation of shear stress for the general case of flow in porous media, at low Reynolds number

Average Wall Shear Stress:

$\bar{\tau}_w = R_h\left(\frac{-\Delta P}{L}\right)$ where R_h is hydraulic radius of a packed bed or porous medium

$$R_h = \frac{Cross\ \text{sec}tional\ area\ for\ flow}{wetted\ perimeter}$$

$R_h = \frac{\varepsilon}{(1-\varepsilon)S_0}$ where S_0 is the specific area (units of inverse length) = ratio of surface area to the volume of the solid's fraction of porous medium.

Darcy's Law: $\frac{\Delta P}{L} = -\frac{\mu}{k}U_{SUPERFICIAL}$

Assuming that $k \sim D_h^2$, where D_h is hydraulic diameter (pg 99 in Probstein's Physicochemical Hydrodynamics)(Probstein, 1989)

$$\frac{\Delta P}{L} = -\frac{\mu}{KD_h^2}U_{SUPERFICIAL}$$

Plugging this expression for the pressure drop back into the original average WSS equation gives

$$\bar{\tau}_w = \sqrt{-\frac{\mu}{K\frac{\Delta P}{L}}U_{SUPERFICIAL}}\left(\frac{-\Delta P}{L}\right) = -\sqrt{-\frac{1}{K}}\sqrt{\mu U_{SUPERFICIAL}\left(\frac{\Delta P}{L}\right)} = \ \sim\ \sqrt{\mu U_{SUPERFICIAL}\left(\frac{\Delta P}{L}\right)}$$

Appendix - II Derivation of shear stress for the general case of flow through an infinite array of spheres (Blake-Kozeny equation), at low Reynolds number

The Blake-Kozeny equation for a packed bed of spherical particles is

$$\frac{\Delta P}{L} = 150\left(\frac{\mu U_{SUPERFICIAL}}{D_P^2}\right)\frac{(1-\varepsilon)^2}{\varepsilon^3}$$

Rearranging the BK equation to solve for the particle diameter gives

$$D_P = \pm\sqrt{150\left(\frac{U_{SUPERFICIAL}\mu L}{\Delta P}\right)\frac{(1-\varepsilon)^2}{\varepsilon^3}}$$ where D_p is sphere diameter

Average Wall Shear Stress:

$$\bar{\tau}_w = R_h\left(\frac{-\Delta P}{L}\right)$$ where R_h is hydraulic radius of a packed bed or porous medium

Strictly, for packed bed flows

$$R_h = \frac{\varepsilon D_P}{6(1-\varepsilon)+4\left(\frac{D_P}{D_C}\right)}$$ where D_c is column diameter. Assuming $(D_p/D_c) \ll 1$

$$R_h = \frac{\varepsilon D_P}{6(1-\varepsilon)}$$ express shear stress in terms of superficial velocity

$$\bar{\tau}_w = R_h\left(\frac{\Delta P}{L}\right) = \frac{\varepsilon D_P}{6(1-\varepsilon)}\left(\frac{-\Delta P}{L}\right) = \frac{\varepsilon\left(\sqrt{150\left(\frac{U_{SUPERFICIAL}\mu L}{\Delta P}\right)\frac{(1-\varepsilon)^2}{\varepsilon^3}}\right)}{6(1-\varepsilon)}\left(\frac{\Delta P}{L}\right)$$

$$\bar{\tau}_w = \frac{\varepsilon\left(\sqrt{150\mu}\right)(1-\varepsilon)}{6(1-\varepsilon)\varepsilon^{3/2}}\left(\frac{\Delta P}{L}\right)^{0.5} U_{SUPERFICIAL}^{0.5} = \frac{\varepsilon^{1/3}\left(\sqrt{150}\right)}{6}\sqrt{\mu U_{SUPERFICIAL}\left(\frac{\Delta P}{L}\right)}$$

Appendix - III Matlab Edge Detection

Taken from
http://www.mathworks.com/products/image/demos.html?file=/products/demos/shipping/images/ipexradius.html

Measuring the Radius of a Roll of Tape

Your objective is to measure the radius of a roll of tape, which is partially obscured by the tape dispenser. You will utilize `bwtraceboundary` to accomplish this task.

Contents

Step 1: Read Image

Read in `tape.png`.

```
RGB = imread('tape.png');
imshow(RGB);

text(15,15,'Estimate radius of the roll of tape',...
     'FontWeight','bold','Color','y');
```

Step 2: Threshold the Image

Convert the image to black and white for subsequent extraction of the edge coordinates using the `bwtraceboundary` routine.

```
I = rgb2gray(RGB);
threshold = graythresh(I);
BW = im2bw(I,threshold);
imshow(BW)
```

Step 3: Extract Initial Boundary Point Location

The `bwtraceboundary` routine requires that you specify a single point on a boundary. This point is used as the starting location for the boundary tracing process.

To find the edge of the tape, pick a column in the image and inspect it until a transition from a background pixel to the object pixel occurs.

```
dim = size(BW);

col = round(dim(2)/2)-90;

row = find(BW(:,col), 1);
```

Step 4: Trace the Boundaries

The `bwtraceboundary` routine is used to find (X, Y) locations of the boundary points. In order to maximize the accuracy of the radius calculation, it is important to find as many points belonging to the tape boundary as possible. You should determine the number of points experimentally.

```
connectivity = 8;
num_points   = 180;
contour = bwtraceboundary(BW, [row, col], 'N', connectivity,
num_points);

imshow(RGB);
hold on;

plot(contour(:,2),contour(:,1),'g','LineWidth',2);
```

Step 5: Fit a Circle to the Boundary

Rewrite basic equation for a circle:

```
(x-xc)^2 + (y-yc)^2 = radius^2,  where (xc,yc) is the center
```

in terms of parameters a, b, c as

```
x^2 + y^2 + a*x + b*y + c = 0,  where a = -2*xc, b = -2*yc, and
                                      c = xc^2 + yc^2 - radius^2
```

Solve for parameters a, b, c, and use them to calculate the radius.

```
x = contour(:,2);
y = contour(:,1);

% solve for parameters a, b, and c in the least-squares sense by
% using the backslash operator
abc = [x y ones(length(x),1)] \ -(x.^2+y.^2);
a = abc(1); b = abc(2); c = abc(3);

% calculate the location of the center and the radius
xc = -a/2;
yc = -b/2;
radius  =  sqrt((xc^2+yc^2)-c)

% display the calculated center
plot(xc,yc,'yx','LineWidth',2);
```

```
% plot the entire circle
theta = 0:0.01:2*pi;

% use parametric representation of the circle to obtain coordinates
% of points on the circle
Xfit = radius*cos(theta) + xc;
Yfit = radius*sin(theta) + yc;

plot(Xfit, Yfit);

message = sprintf('The estimated radius is %2.3f pixels', radius);
text(15,15,message,'Color','y','FontWeight','bold');
radius =

   80.7256
```

Appendix - IV Standard Normal Distribution from Central Limit Theorem

The standard normal distribution can be obtained from Central Limit Theorem, which states that "If $\overline{X}$ is the mean of a random sample X_1, X_2, ……, X_n of size n from a distribution with finite mean μ and a finite positive variance σ^2, then the distribution of

$$W = \frac{\overline{X} - \mu}{\sigma/\sqrt{n}} = \frac{\sum_{i=1}^{n} X_i - n\mu}{\sqrt{n}\sigma}$$

is N(0,1) in the limit as $n \rightarrow \infty$" (Hogg and Tanis, 1988).

This random sample X_1, X_2,…… X_n of size n, which has finite mean μ and a finite positive variance σ^2, is obtained from a sample having a uniform distribution, U(a,b) = U(0,1) with same mean $\mu = (a+b)/2 = (0+1)/2 = 0.5$ and variance $\sigma^2 = (b-a)^2/12 = 1/12$. Therefore, for a sample size of n = 48 we can generate a normal distribution with zero mean and variance one as follows

$$Z = W = \frac{\sum_{i=1}^{n} X_i - n\mu}{\sqrt{n}\sigma} = \frac{\sum_{i=1}^{48} X_i - 24}{2}$$

Appendix - V Trilinear Interpolation

Taken from http://local.wasp.uwa.edu.au/~pbourke/miscellaneous/interpolation/

Written by Paul Bourke
July 1997

Trilinear interpolation is the name given to the process of linearly interpolating points within a box (3D) given values at the vertices of the box. Perhaps its most common application is interpolating within cells of a volumetric dataset.

Consider a unit cube with the lower/left/base vertex at the origin as shown here on the right. The values at each vertex will be denoted V_{000}, V_{100}, V_{010}, ...etc....V_{111}

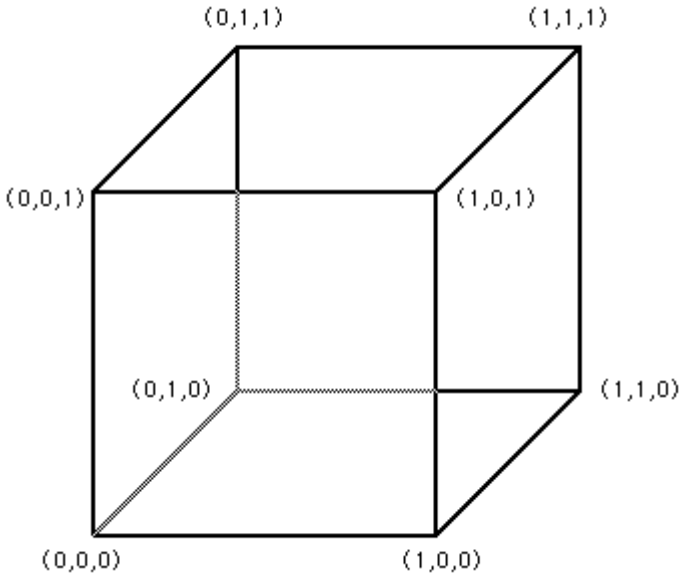

The value at position (x,y,z) within the cube will be denoted V_{xyz} and is given by

$$V_{xyz} = V_{000} (1 - x) (1 - y) (1 - z) +$$
$$V_{100} x (1 - y) (1 - z) +$$
$$V_{010} (1 - x) y (1 - z) +$$
$$V_{001} (1 - x) (1 - y) z +$$
$$V_{101} x (1 - y) z +$$
$$V_{011} (1 - x) y z +$$
$$V_{110} x y (1 - z) +$$
$$V_{111} x y z$$

In general the box will not be of unit size nor will it be aligned at the origin. Simple translation and scaling (possibly of each axis independently) can be used to transform into and then out of this simplified situation.